

4-2024

DISTURBANCE OBSERVER-BASED CONTROL FOR PMSG-BASED WIND TURBINER CONSIDERING UNBALANCED GRID CONDITIONS

Moayad Alanani Maher

Follow this and additional works at: https://scholarworks.uaeu.ac.ae/all_theses



Part of the [Electrical and Computer Engineering Commons](#)



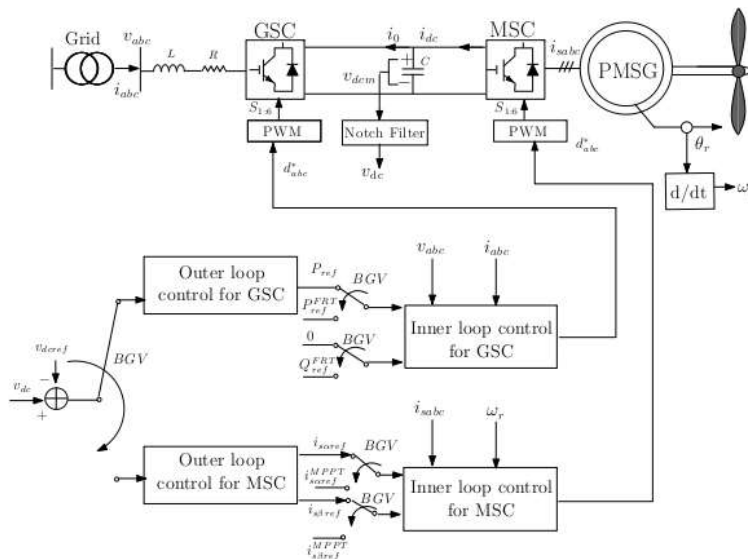
MASTER THESIS NO. 2024: 25

College of Engineering

Department of Electrical and Communication Engineering

**DISTURBANCE OBSERVER-BASED CONTROL FOR
PMSG-BASED WIND TURBINER CONSIDERING
UNBALANCED GRID CONDITIONS**

Moayad Maher Alanani



April 2024

United Arab Emirates University

College of Engineering

Department of Electrical and Communication Engineering

**DISTURBANCE OBSERVER-BASED CONTROL FOR PMSG BASED-
WIND TURBINE CONSIDERING UNBALANCED GRID
CONDITIONS**

Moayad Maher Alanani

This thesis is submitted in partial fulfilment of the requirements for the degree of Master of
Science in Electrical Engineering

April 2024

United Arab Emirates University Master Thesis
2024: 25

Cover: Power control scheme for PMSG wind energy conversion system
(Photo: By Moayad Maher Alanani)

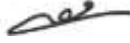
© 2024 Moayad Maher Alanani, Al Ain, UAE

All Rights Reserved

Print: University Print Service, UAEU 2024

Declaration of Original Work

I, Moayad Maher Alanani, the undersigned, a graduate student at the United Arab Emirates University (UAEU), and the author of this thesis entitled “*Disturbance Observer-Based Control for PMSG-Based Wind Turbine Considering Unbalanced Grid Conditions*”, hereby, solemnly declare that this is the original research work done by me under the supervision of Dr. Rachid Errouissi, in the College of Engineering at UAEU. This work has not previously formed the basis for the award of any academic degree, diploma or a similar title at this or any other university. Any materials borrowed from other sources (whether published or unpublished) and relied upon or included in my thesis have been properly cited and acknowledged in accordance with appropriate academic conventions. I further declare that there is no potential conflict of interest with respect to the research, data collection, authorship, presentation and/or publication of this thesis.

Student's Signature: 

Date: 22/04/2024

Approval of the Master Thesis

This Master Thesis is approved by the following Examining Committee Members:

1) Advisor (Committee Chair): Rachid Errouissi

Title: Associate Professor

Department of Electrical and Communication Engineering

College of Engineering

Signature:



Date: 22/04/2024

2) Member: Addy Wahyudie

Title: Associate professor

Department of Electrical and Communication Engineering

College of Engineering

Signature:



Date: 22/04/2024

3) Member (External Examiner): Yasser Mohamed

Title: Professor

Department of Electrical and Computer Engineering

Institution: University of Alberta, Canada

Signature:



Date: 22/04/2024

This Master Thesis is accepted by:

Dean of the College of Engineering: Professor Mohamed H. Al-Marzouqi

Signature Mohamed AlMarzouqi

Date June 04, 2024

Dean of the College of Graduate Studies: Professor Ali Al-Marzouqi

Signature Ali Hassan

Date June 5, 2024

Abstract

A typical Permanent Magnet Synchronous Generator (PMSG)-based wind turbine system consists of an electrical generator, Machine-Side Converter (MSC), Grid-Side Converter (GSC), dc-link capacitor, and a passive filter such as L filter or LCL filter to connect the GSC to the host grid. When the wind turbine operates under unbalanced grid voltages, a negative sequence component is introduced to the system. This negative sequence voltage can pose challenges for classical controllers to ensure an efficient control of the PMSG-based wind turbine system. On one hand, when the control objective is to ensure injecting sinusoidal and balanced three-phase currents to the grid, voltage unbalance can cause active power to oscillate at double fundamental frequency. On the other hand, delivering constant active power to the grid, under unbalanced voltages, requires injecting sinusoidal and unbalanced three-phase currents to the grid. In the current control scheme, constant active power operation during unbalanced voltages can be achieved by setting the grid currents to follow appropriate sinusoidal and unbalanced current references. In power control scheme, these current references can be used to compute the active and reactive power commands required to achieve ripple-free active power under unbalanced voltage conditions. During unbalanced grid voltages, ripple-free active power can produce a sinusoidal oscillation of frequency 2ω in the dc-link voltage, where ω is the grid frequency. This oscillation occurs due to periodic energy exchange between the inductance of the passive filter and the dc-link capacitor, as no active power oscillations are injected into the grid. This energy exchange also occurs between the dc-link voltage and the stator windings of the PMSG, resulting in 2ω ripple in the torque of the generator. Thus, under unbalanced grid voltages, appropriate control strategies are required for the control of the GSC and MSC to enable efficient power exchange between the host grid and the wind turbine.

This thesis presents the design and performance evaluation of a robust control strategy for both GSC and MSC. Under balanced grid voltage conditions, GSC regulates the dc-link voltage through controlling either the current or the power injected into the grid, while the MSC regulates the stator currents of the PMSG aiming to maximize the power extracted from

the wind. During unbalanced grid voltage conditions, the roles of GSC and MSC are interchanged. In particular, the MSC regulates the dc-link voltage through controlling the stator currents of the PMSG, while the GSC regulates the active power delivered to the grid to allow implementing the so-called “Fault Ride Through” algorithm. In this thesis, the proposed controller for both converters is based on combining a state-feedback controller with a disturbance observer. The feedback controller has the role of stabilizing the nominal closed-loop system, while the disturbance observer plays the role of a servo-compensator to cancel the effect of model uncertainties and unknown disturbances, considering the oscillatory behavior of disturbances under unbalanced grid voltages. Another advantage of the disturbance observer is its ability to achieve a seamless transition between the control schemes in response to sudden balance/unbalance event in grid voltages. The proposed controller also makes use of a notch filter to cancel the effect of the inherent dc-link voltage oscillations on the machine torque, particularly when the grid voltage is unbalanced.

Simulation tests are conducted to verify the performances of the proposed control technique using MATLAB Software considering realistic scenarios and adequate control parameters. The results demonstrate that the proposed control scheme can achieve good steady-state and transient performances under both balanced and unbalanced grid voltages. More importantly, the obtained results show that proposed controller is able to maintain good transient performances in response to sudden unbalance/balance events in the grid voltages.

Keywords: PMSG, GSC, MSC, disturbance observer, feedback linearization, sinusoidal disturbance rejection, unbalanced grid voltages.

Title and Abstract (in Arabic)

التحكم القائم على مراقب الاضطراب ل PMSG في ظل ظروف الشبكة غير المتوازنة

الملخص

تتكون توربينات الرياح المتزامنة القائمة على المغناطيس الدائم النموذجي من مولد كهربائي ، ومحول من جانب الماكينة (MSC) ، ومحول من جانب الشبكة (GSC) ، ومكثف وصلة تيار مستمر ، ومرشح سلمي لتوصيل GSC بالشبكة. عند التشغيل تحت الفولتية غير المتوازنة للشبكة ، سيتم إدخال مكون تسلسل سلبي إلى النظام ، والتفاعل بين جهد التسلسل الموجب والسلمي سوف تتأرجح الطاقة المحقونة في الشبكة بتردد أساسي مزدوج. يمكن تحقيق الطاقة النشطة الخالية من التموج أثناء جهد الشبكة غير المتوازن عن طريق ضبط تيارات الشبكة لتتبع مراجع التيار الجيبي وغير المتوازنة المناسبة. يمكن استخدام هذه المراجع الحالية لحساب أوامر الطاقة النشطة والتفاعلية التي سيتم تسليمها بواسطة الشبكة بهدف تحقيق مهمة الطاقة النشطة الخالية من التموج في ظل الفولتية غير المتوازنة للشبكة. ومع ذلك ، فإن الطاقة النشطة الخالية من التموج أثناء جهد الشبكة غير المتوازن يمكن أن تنتج تذبذبا جيبيا للتردد 2ω في جهد وصلة التيار المستمر. يمكن تفسير هذا التذبذب من خلال التبادل الدوري للطاقة المخزنة في مرشح L مع الطاقة المخزنة في مكثف link-dc حيث لا يتم حقن تذبذبات الطاقة النشطة في الشبكة. يمكن أن يحدث هذا التبادل الدوري للطاقة أيضا بين جهد وصلة التيار المستمر ولفات الجزء الثابت ل PMSG ، مما قد يؤدي إلى تموج 2ω في عزم دوران PMSG. نظرا لعدم وجود مسار خارجي لهذا التذبذب. وبالتالي ، في ظل الفولتية الشبكية غير المتوازنة ، هناك حاجة إلى تقنيات تحكم متقدمة للسماح للتيارات والقوى النشطة والتفاعلية بتتبع مراجعها بدقة وقوة. تقدم هذه الأطروحة التصميم والتحقق التجريبي لاستراتيجية تحكم قوية لكل من GSC و MSC. في حالة جهد الشبكة المتوازن ، تكون GSC مسؤولة عن تنظيم جهد وصلة التيار المستمر. بينما تتمثل الوظيفة الرئيسية ل MSC في زيادة استخراج الطاقة من الرياح باستخدام خوارزمية MPPT. في سياق جهد الشبكة غير المتوازن ، يتم تبادل وظائف GSC و MSC. تتحمل MSC مسؤولية تنظيم جهد وصلة التيار المستمر ، من ناحية أخرى ، فإن وحدة تحكم GSC مسؤولة عن تنظيم الطاقة النشطة. تعتمد وحدة التحكم المقترحة على الجمع بين وحدة تحكم التغذية المرتدة للحالة ومراقب الاضطراب. يتم استخدام وحدة التحكم في التغذية المرتدة لتنشيط نظام الحلقة المغلقة ، بينما يتم استخدام مراقب الاضطراب للتعويض عن تأثير عدم اليقين في النموذج مع الأخذ في الاعتبار السلوك التذبذبي للاضطرابات تحت الفولتية الشبكية غير المتوازنة. علاوة على ذلك ، يتم تطبيق مرشح الشق على قياس جهد وصلة التيار المستمر قبل تغذيته في وحدة التحكم في جهد وصلة التيار المستمر من أجل إلغاء تأثير تموج 2ω على وحدة التحكم في الجهد علاوة على ذلك ، يتم تطبيق مرشح الشق لقياس جهد وصلة التيار المستمر لإلغاء تأثير تموج 2ω على جهد وصلة التيار المستمر وعزم دوران الماكينة. تم إجراء اختبارات محاكاة وتجريبية مختلفة للتحقق من أداء تقنية التحكم المقترحة. أظهرت النتائج التي تم الحصول عليها أن كلا من مخطط التحكم في الطاقة ونظام التحكم الحالي قادران على تحقيق تتبع دقيق للمراجع

الجيبية في ظل ظروف الشبكة المتوازنة وغير المتوازنة. كان التتبع الدقيق لمراجع الطاقة / التيار تحت وحدة التحكم المركبة فعالا في القضاء على خطأ الحالة المستقرة وتموجات الطاقة المحقونة تحت كل من الفولتية الشبكية المتوازنة وغير المتوازنة.

مفاهيم البحث الرئيسية: محول من جانب الشبكة، ومحول من جانب الماكينة ، مراقب الاضطراب ، التغذية الراجعة الخطية ، رفض الاضطراب الجيبي ، الفولتية غير المتوازنة للشبكة.

Acknowledgements

I would like to express my sincere gratitude to my supervisor, Dr. Rachid Errouissi, for his invaluable guidance, unwavering support, and expert advice throughout the course of my thesis. His dedication to excellence and passion for the subject matter have been a constant source of inspiration. I am deeply thankful for the time and effort Dr. Errouissi invested in reviewing my work, providing constructive feedback, and helping me navigate the complexities of the research process. His mentorship has been instrumental in shaping the quality and direction of this thesis.

I would also like to extend my appreciation to my beloved parents and family for their encouragement and support.

This thesis would not have been possible without the encouragement, expertise, and support of those mentioned above. I am truly grateful for their contributions to this academic journey.

Dedication

To my beloved parents and family

Table of Contents

Title.....	i
Declaration of Original Work.....	iii
Approval of the Master Thesis	iv
Abstract.....	vi
Title and Abstract (in Arabic).....	viii
Acknowledgements.....	x
Dedication.....	xi
Table of Contents.....	xii
List of Table.....	xv
List of Figures.....	xvi
List of Abbreviations	xviii
Chapter 1: Introduction.....	1
1.1 Overview	1
1.2 Statement of the Problem	7
1.3 Research Objectives	8
1.4 Relevant Literature	9
1.4.1 Voltage-Oriented Control	10
1.4.2 Direct Power Control	17
1.4.3 Maximum Power Point Tracking.....	21
1.4.4 Disturbance Observer Based Control.....	25
Chapter 2: Mathematical Model	28
2.1 Mathematical Model of Grid-tied Inverter.....	29
2.1.1 Mathematical Model in the Natural Frame.....	29
2.1.2 Mathematical Model in the Stationary $\alpha\beta$ Reference Frame	30
2.1.3 Mathematical Model in the Synchronous dq Reference Frame	32
2.1.4 Mathematical Model Using P and Q as State Variables.....	34
2.2 Mathematical Model of Permanent Magnet Synchronous Generator.....	36
2.2.1 Aerodynamic Model of Wind Turbine	36
2.2.2 Mathematical Model of PMSG in the Natural abc Reference Frame	38

2.2.3 Mathematical Model of PMSG in the Stationary Frame	40
2.2.4 Mathematical Model of PMSG in the Synchronous Frame.....	42
2.2.5 Electromagnetic Torque	46
2.3 Dynamics of the DC-link Voltage.....	47
2.3.1 Model for DC-link Voltage under Balanced Grid Voltages	47
2.3.2 Model for DC-link Voltage under Unbalanced Grid Voltages.....	49
2.4 Summary.....	51
Chapter 3: Control of PMSG-Based Wind Energy Generation System in Stationary Reference $\alpha\beta$ Frame.....	52
3.1 Power Control of the Grid-Side Converter.....	55
3.1.1 Perturbed Model of the Grid-Side Converter.....	55
3.1.2 Feedback Controller	56
3.1.3 Disturbance Observer.....	58
3.2 DC-Link Control under Balanced Grid Voltages.....	66
3.2.1 Feedback Controller	66
3.2.2 Disturbance Observer.....	67
3.3 Current Control of the Machine-Side Converter.....	70
3.3.1 Perturbed Model and Feedback Controller	70
3.3.2 Disturbance Observer.....	73
3.3.3 Current Reference for Maximum Power Point Tracking (MPPT)	78
3.4 DC-Link Control under Unbalanced Grid Voltages	81
3.5 Power Reference Calculation During Unbalanced Grid Voltages	83
3.6 Mitigation of 2ω -Oscillation Effect on the Machine Torque under Unbalanced Grid Voltages.....	85
3.7 Simulation Results.....	86
3.7.1 Performance Evaluation under Balanced Grid	89
3.7.2 Performance Evaluation under Unbalanced Grid Voltages without Notch Filter.....	91
3.7.3 Performance Evaluation under Unbalanced Grid Voltages along with Notch Filter	94
3.7.4 Performance Evaluation of the Disturbance Observer Effect and under Unbalanced Grid Voltages	96

3.7.5 Performance Evaluation under a Grid Condition Transition	100
3.7.6 Performance Evaluation under Model Uncertainties and Unbalanced Grid Voltages	102
3.8 Summary.....	104
Chapter 4: Control of PMSG in Synchronous Reference Frame	106
4.1 Current Control of the Grid-Side Converter.....	108
4.1.1 Perturbed Model of the Grid-Side Converter.....	108
4.1.2 Feedback Controller	108
4.1.3 Disturbance Observer.....	109
4.2 DC-Link Control under Balanced Grid Voltages.....	114
4.2.1 Feedback Controller	114
4.2.2 Disturbance Observer.....	115
4.3 Phase-Locked Loop (PLL)	116
4.4 Current Control of the Machine-Side Converter.....	117
4.4.1 Perturbed Model and Feedback Controller	117
4.4.2 Disturbance Observer.....	118
4.5 current Reference Calculation During Unbalanced Grid Voltages	120
4.6 Simulation Results.....	121
4.6.1 Performance Evaluation under Balanced Grid	123
4.6.2 Performance Evaluation under Unbalanced Grid Voltages without Notch Filter.....	125
4.6.3 Performance Evaluation under Unbalanced Grid Voltages along with Notch Filter	127
4.6.4 Performance Evaluation of the Disturbance Observer Effect and under Unbalanced Grid Voltages	129
4.6.5 Performance Evaluation under a Grid Condition Transition	133
4.6.6 Performance Evaluation under Model Uncertainties and Unbalanced Grid Voltages	135
4.7 Summary.....	137
Chapter 5: Conclusion	139
References.....	144
List of Publications	154

List of Table

Table 1: Comparative analysis of vector oriented control methodologies	17
Table 2: Comparative analysis of direct power control methodologies	20
Table 3: Comparison of MPPT control techniques	24
Table 4: Grid parameters	88
Table 5: PMSG parameters.....	88
Table 6: Grid side control parameters	89
Table 7: Machine side control parameters.....	89
Table 8: Grid parameters	122
Table 9: PMSG parameters.....	122
Table 10: Grid controller parameters.....	123
Table 11: PMSG grid controller parameters.....	123

List of Figures

Figure 1: Typical topology of a wind energy conversion system	2
Figure 2: Topology of a PMSG connected to the grid by back-to-back converter	4
Figure 3: Ac and dc side of a three-phase rectifier	29
Figure 4: Model of PMSM along with a three-phase power converter	38
Figure 5: dq frame model for the PMSG	44
Figure 6: dq frame model for the PMSG including stator voltage dynamics	45
Figure 7: General power control scheme	55
Figure 8: Mechanical power generated by the turbine in y-axis as a function of the rotor speed in x-axis for different wind speeds	81
Figure 9: Structure of the DSOGL	85
Figure 10: Control diagram for testing the developed controller	87
Figure 11: Grid simulation results under balanced grid voltages	90
Figure 12: PMSG simulation results under balanced grid voltages	91
Figure 13: Grid simulation results under unbalanced grid voltages without notch filter	93
Figure 14: PMSG simulation results under unbalanced grid voltages without notch filter	94
Figure 15: Grid simulation results during unbalanced grid voltages along with notch filter	95
Figure 16: PMSG simulation results under unbalanced grid voltages along with notch filter	96
Figure 17: Grid simulation results when the disturbance observer was disabled at $t = 0.1$ s from the grid	97
Figure 18: PMSG simulation results when the disturbance observer was disabled at $t = 0.1$ s from the grid	98
Figure 19: Grid simulation results when the disturbance observer was disabled at $t = 0.1$ s from the machine	99
Figure 20: PMSG simulation results when the disturbance observer was disabled at $t = 0.1$ s from the machine	100
Figure 21: Grid simulation results when 50% dip in Phase B was suddenly created at $t = 0.04$ s to 0.14 s.	101
Figure 22: PMSG simulation results when 50% dip in Phase B was suddenly created at $t = 0.04$ s to 0.14 s	102

Figure 23: Grid simulated outcomes of the grid when the resistance R and inductance L utilized in the controller are increased by 150% of their nominal values	103
Figure 24: PMSG simulated outcomes of the grid when the resistance R and inductance L utilized in the controller are increased by 150% of their nominal values	104
Figure 25: General current control scheme	107
Figure 26: Control scheme for testing the proposed controller	121
Figure 27: Grid simulation results under balanced grid voltages.....	124
Figure 28: PMSG simulation results under balanced grid voltages	125
Figure 29: Grid simulation results under unbalanced grid voltages without notch filter	126
Figure 30: PMSG simulation results under unbalanced grid voltages without notch filter	127
Figure 31: Grid simulation results during unbalanced grid voltages with notch filter	128
Figure 32: PMSG simulation results during unbalanced grid voltages with notch filter	129
Figure 33: Grid simulation results when the disturbance observer was disabled at $t = 0.1$ s from the grid.....	130
Figure 34: PMSG simulation results when the disturbance observer was disabled at $t = 0.1$ s from the Grid.....	131
Figure 35: Grid simulation results when the disturbance observer was disabled at $t = 0.1$ s from the machine.....	132
Figure 36: PMSG simulation results when the disturbance observer was disabled at $t = 0.1$ s from the machine.....	133
Figure 37: Grid simulation results when 50% dip in Phase B was suddenly created at $t = 0.04$ s to 0.14 s.....	134
Figure 38: PMSG simulation results when 50% dip in Phase B was suddenly created at $t = 0.04$ s to 0.14 s.....	135
Figure 39: Grid simulated outcomes of the grid when the resistance R and inductance L utilized in the controller are increased by 150% of their nominal values	136
Figure 40: PMSG simulated outcomes of the grid when the resistance R and inductance L utilized in the controller are increased by 150% of their nominal values	137

List of Abbreviations

BPSC	Balanced Positive Sequence Control
BSC	Backstepping Control
DN	Decoupling Network
DOBC	Disturbance Observer Based Control
DPC	Direct Power Control
EHGSO	Extended High-Gain State Observer
EMF	Electromagnetic Field
ESO	Extended State Observer
FLC	Fuzzy Logic Control
FRT	Fault Ride Through
FSWT	Fixed Speed Wind Turbine
GSC	Grid Side Converter
HAWT	Horizontal Axis Wind Turbine
HCC	Hysteresis Current Controller
HCS	Hill Climb Search
HOSMC	High Order Sliding Mode Control
IAPC	Instantaneous Active Power Control
IARC	Instantaneous Active and Reactive Power Control
LDUE	Linear Disturbance and Uncertainty Estimation
LPF	Low Pass Filter
MMF	Magneto Motive Forces
MPC	Model Predictive Control

MPPT	Maximum Power Point Tracking
MSC	Machine Side Converter
NDO	Nonlinear Disturbance Observer
NDUE	Nonlinear Disturbance and Uncertainty Estimation
NN	Neural Network
NPC	Neutral Point Clamped
OT	Optimal Torque
P&O	Perturbation and Observation
PI	Proportional Integral
PLL	Phase Locked Loop
PMSG	Permanent Magnet Synchronous Generators
PMSM	Permanent Magnet Synchronous Motor
PR	Proportional Resonant
PSF	Power Signal Feedback
PWM	Pulse Width Modulation
SCIG	Squirrel Cage Induction Generator
SMC	Sliding Mode Control
SRF	Synchronous Reference Frame
ST-DPC	Switching Table Direct Power Control
SVM	Space Vector Modulation
TSMC	Terminal Sliding Mode Control
TSR	Tip Speed Ratio
UIO	Unknown Input Observer
VAWT	Vertical Axis Wind Turbine

VOC	Voltage Oriented Control
VSC	Voltage Source Converter
VSI	Voltage Source Inverter
VSWT	Variable Speed Wind Turbine
WECS	Wind Energy Conversion System
WRIG	Wound Rotor Induction Generator

Chapter 1: Introduction

1.1 Overview

Due to rising electricity demand and global warming concerns, the adoption of renewable energy sources for the generation of electricity has experienced an unprecedented acceleration. Among these renewable energies, wind energy is one of the most economical and promising sources [1]. Many developing countries have significant untapped wind energy potential. Moreover, in many locations, generating electricity from wind energy offers a cost-effective alternative to thermal power stations in terms of lower impact on the environment and climate, reduces dependence on fossil fuel imports, and increases security of energy supply [2].

Wind Energy Conversion Systems (WECSs) produce electrical energy by capturing the kinetic energy of the wind and utilizing it to drive an electrical generator. The kinetic energy of the incoming air stream is converted into electrical energy in two steps: the extraction device, i.e., the wind turbine rotor, captures the wind power movement with aerodynamically designed blades and converts it into rotating mechanical energy that drives the wind turbine generator where the mechanical power is converted into electrical power. A gear box can be used to match the rotational speed of the wind turbine rotor to that of the generator. In addition, power electronic converters are used for enhanced power extraction and variable speed operation of the wind turbine [1]. The topology of a complete wind energy conversion system is depicted in Figure 1.

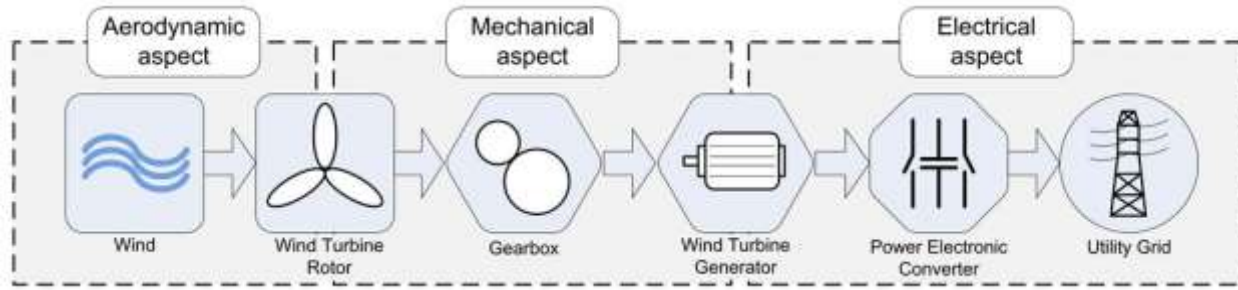


Figure 1: Typical topology of a wind energy conversion system.

There are two types of wind turbines, Horizontal-Axis Wind Turbine (HAWT) and Vertical-Axis Wind Turbine (VAWT). HAWT are among the widely used wind turbine[2]. WECS are classified into two types based on the speed control criteria such as Fixed-Speed Wind Turbine (FSWT) and variable-speed WECS. In FSWT topology, the turbine is directly connected to the grid through gear box and a shaft [3,4]. The FSWT configuration system is commonly known as a constant or fixed speed system, and it is usually based on either the Squirrel-Cage Induction Generator (SCIG) or a Wound Rotor Induction Generator (WRIG). Regardless of wind speed, the rotor speed in FSWT is imposed by the frequency of the supply grid, the gear ratio, and the number of pole-pairs of a generator. The system achieves maximum efficiency at a specific wind speed, but the energy capture does not reach its maximum in wind speeds above and below the rated wind speed. Despite its limited inability to extract maximum power from the wind, FSWT system are simple, robust, reliable, and cost effective in terms of their electrical components [1].

Variable speed operation and direct-drive generators have been the recent developments in wind turbine drive trains. Compared to constant speed operation, variable speed operation of wind turbines provides 10-15% higher energy output, lower mechanical stress, and less power fluctuation. Variable-speed WECS utilizes both synchronous generators and doubly fed induction generators [5,6]. Unlike constant-speed WECS, variable-speed WECS needs power electronic converters in order to convert variable-frequency and variable-voltage at the output of the generator into constant-frequency and constant-voltage. Among the main advantages for using power converters in the WECS are load control, energy

optimal operation, soft drive train, gearless option, and reduced noise while, controllable active and reactive powers, local reactive power source, improved network voltage stability, and improved power quality [7].

The various converter topologies commonly employed for variable-speed WECS with Permanent Magnet Synchronous Generators (PMSG) include DC-DC boost converters, Neutral Point Clamped (NPC) converters, Pulse Width Modulation (PWM) current source converters, diode rectifiers, Voltage Source Converters (VSC), and back-to-back VSC. The DC-DC boost diode rectifier and VSC commonly face challenges in regulating the characteristics on the generator side, which results in lower efficiency as the parameters on the grid side are only controlled. The operation and control of NPC converter is more complex compared to other converters. However, considering the challenges of various converter topologies, the utilization of a two-level back-to-back VSC topology is strongly favored for variable speed WECS with PMSG. It is considered as the most effective converter topology for controlling the active and reactive powers on the generator-side, as well as controlling the DC-link voltage and power on the grid-side [8]. The topology of a PMSG connected to the grid using a back-to-back converter is shown in Figure 2. The system consists of two Voltage Source Inverters (VSI) coupled together using a dc-link capacitor. One VSI is called Grid-Side Converter (GSC), and it is used to interface with the main power grid, the other VSI is known as Machine-Side Converter (MSC), and it is responsible for regulating the power extracted from the wind. Under certain conditions, the MSC is primarily utilized to control the electrical generator in order to optimize power extraction from the wind [9]. Besides, an L filter connects the GSC to the grid with the aim of reducing the current harmonics injected into the grid.

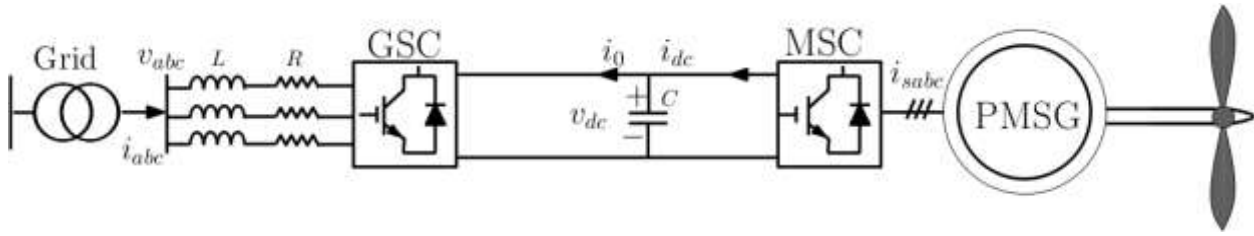


Figure 2: Topology of a PMSG connected to the grid by back-to-back converter.

Literature review reveals that the topology of PMSG-based Wind Turbine (WT) can include additional components such as active crowbars and dc choppers [10], energy storage devices [11], series dynamic breaking resistor[12], dc chopper[13], and others. These components can help increasing the reliability of the energy conversion system in the presence of abnormal conditions, which is achieved at the expense of increasing the system cost and complexity [14]. The literature also reports that several approaches have been proposed to control PMSG-based WT to handle abnormal conditions including grid faults. The control of the PMSG-based WT involves two distinct steps. The first step involves acquiring the signals and measurements essential for the primary controller, including grid voltages, grid currents and dc output voltage. Furthermore, under certain circumstances, it may be essential to perform extra calculations, such as isolating the positive and negative sequence components of grid currents and voltages, in order to achieve certain control objectives, especially during abnormal grid conditions. Controllers for Permanent Magnet Synchronous Generators (PMSG) are often designed utilizing either the synchronous reference frame or stationary reference frame. Therefore, it is necessary to mathematically convert the grid currents and voltages into these reference frames. The second step involves designing a control strategy that can meet the transient and steady-state performance specifications. The main control objective is to deliver a constant active power to the grid, inject a specific amount of reactive power to fulfill Fault Ride-Through (FRT) requirement, and regulate the dc-link voltage. It's noteworthy that, in certain situations, exchanging the control roles between the GSC and MSC might be advantageous for maintaining system stability, especially when managing large-scale wind energy. As an example, the GSC can be manipulated to solely manage the active and reactive powers supplied to the grid, whereas the MSC can be employed to ensure a

constant dc-link voltage. As pointed in [15], this control structure can have the capability to reduce the resistive losses in the PMSG and can have the added benefit of providing ancillary services to improve the dynamic stability of electric power systems, particularly, when there are abrupt changes in the load. In case of voltage imbalance, injecting reactive power into the power grid becomes essential to ensure that the grid voltage remains above a certain voltage threshold. Based on the severity of the voltage unbalance, the grid code determines the amount of reactive power to be supplied to the grid during short-term unbalance event. It is important to emphasize that each power system has its own specific protocol for implementing the FRT technique, which ensures that the grid voltage remains within acceptable limits during short-term disruptions. Literature also reveals that voltage sag can cause the GSC current to exceed its maximum allowable value. Thus, necessitating a reduction in the power transmitted from the dc-link to the grid side converter. Another problem of voltage sag is that the dc-link voltage may experience a significant transient overshoot if the dc-link capacitor continues to receive the same power as before the voltage sag event. This occurs when the MSC is controlled to operate the PMSG to extract the maximum available power from the wind.

During balanced grid voltages, a typical control scheme makes use of the GSC to control the active and reactive powers delivered to the grid through the regulation of the dc-link voltage. In such a case, MSC can be employed to implement Maximum Power Point Tracking (MPPT) algorithm so that the PMSG can extract the maximum available power from the wind. This can be achieved by setting either the torque or the speed of PMSG to follow an appropriate command value that is normally provided by an MPPT algorithm. However, under voltage unbalance, the presence of the negative sequence component of the grid voltage can lead to the creation of second order harmonic oscillations in the grid-side active power and dc-link voltage. However, injecting oscillating active power into the grid is considered a breach of the grid code regulation, which mandates that the provided active power must be free from any fluctuations. This mandated ripple-free active power during unbalanced grid voltage can result in a sinusoidal oscillation of frequency 2ω in the dc-link voltage, which can negatively affect the torque response of the generator. The consequence of this impact

can cause fluctuations in the machine torque, which in turn can result in undesired vibrations, ultimately diminishing the durability and lifespan of the motor that connects the generator to the wind turbine [16]. More precisely, in the case of ripple-free active power, the dc-link oscillation can be explained by a periodic exchange of the energy stored in the L filter with the energy stored in the dc-link capacitor since no active power oscillations are injected into the grid [17]. This periodic exchange of energy can also occur between the dc-link voltage and the stator windings of the PMSG, which can result in 2ω ripple in the torque of PMSG, since there is no external path for this oscillation. The aforementioned considerations highlight the necessity of an appropriate control scheme for the PMSG-based WT in order to comply with grid code regulation and to ensure an efficient use of the electrical generator under both normal and abnormal conditions.

A solution to the aforementioned problems can be achieved by interchanging the control roles between GSC and MSC, particularly when the grid is subject to voltage unbalance. More specifically, during voltage unbalance, the role of GSC can be limited to only assure the control of active and reactive powers delivered to the grid, while the dc-link voltage regulation can be achieved by MSC through the control of the stator currents of PMSG, such a control structure is adopted in this research work to operate PMSG-based WECS under unbalanced grid voltage condition. Here, the main control objective of GSC is to inject ripple-free active power and sinusoidal currents into the grid, this requires the reactive power to oscillate with frequency 2ω . The dc component of the reactive power is determined by the FRT algorithm considering the severity of the voltage unbalance. Achieving this requirement demands a controller that is able to achieve accurate tracking of sinusoidal signals with zero and non-zero dc components. In this research work, the Disturbance Observer-Based Control (DOBC) approach is employed to achieve the task of accurate tracking of constant active power command and sinusoidal reactive power command. Similarly, DOBC technique is adopted to control MSC to ensure asymptotic regulation of the dc-link voltage. The control of MSC is achieved through a cascade control scheme, where an outer loop regulates the dc-link voltage, and an inner loop controls the stator currents, the DOBC approach is employed in both loops for the control of MSC.

This research work mainly focuses on applying DOBC approach to PMSG-based WT with a view to evaluate its effectiveness in implementing FRT algorithm in the case of voltage unbalance. The main part of the control design is the development of the disturbance observer which represents the core of the controller. Thus, this research work is mainly focused on designing a stable disturbance observer that can accurately predict the effect of modeling errors and unknown perturbations on the control performance. Under voltage unbalance, this unknown effect is assumed to exhibit oscillatory behavior with both zero and non-zero dc components. The estimated disturbance is subsequently inputted into the feedback controller to compensate for the effects of uncertainties that were not considered during the modeling phase. Not only does the disturbance observer improve the accuracy of the composite controller, but it can also ensure seamless transition between the control schemes in response to sudden balance/unbalance event in grid voltages. Another advantage of the disturbance observer is its ability to mitigate the effect of control saturation during transients, particularly when the control limitation is considered in the disturbance observer design. During control saturation, a composite controller naturally incorporates an anti-windup method to counteract the accumulation of resonator and/or integrator effects. Another contribution of this thesis is to provide a solution to the torque oscillations under unbalanced grid voltages. This is achieved by applying a notch filter to the measurement of the dc-link voltage before feeding it into the dc-link voltage controller. The notch filter effectively cancels the effect of 2ω ripple on the dc-link voltage controller. As a result, only dc component of dc-link voltage measurement is fed into the outer voltage loop, preventing the propagation of 2ω ripple to the command value for the inner current loop.

1.2 Statement of the Problem

PMSG-based wind turbine has gained considerable attention in renewable energy systems because of the intrinsic benefits of PMSG, including high efficiency, compact size, good reliability, and high-power density. In grid tied-applications, a typical PMSG-based wind turbine uses a back-to-back converter to control the power exchange between the wind turbine and the grid. Back-to-back converter is composed of Grid-Side Converter (GRS),

Machine-Side Converter (MSC), dc-link capacitor, and a passive filter that can be either an L filter or an LCL filter. Reliable and efficient operation of PMSG-based wind turbine requires employing appropriate controllers for the power converters to cope with both balanced and unbalanced voltages. The reason is that voltage unbalance can pose challenges for the existing controllers to ensure stable, fast, accurate, robust, and reliable control of the machine's output power, the dc-link voltage, and the power delivered to the grid. An example of these challenges is the difficulty of having ripple-free dc-link voltage under unbalanced voltages, which can adversely impact the quality of the machine output torque. More precisely, the dc-link voltage oscillations can lead to substantial torque fluctuations, which in turn can result in undesirable vibrations. Ultimately, this can reduce the durability and lifespan of the rotor that connects the generator to the wind turbine. Another concern of abnormal conditions is the need for an appropriate control scheme to facilitate implementing the so-called Fault Ride-Through (FRT) strategy with a view to comply with grid connection requirement under both balanced and unbalance grid voltages.

1.3 Research Objectives

The main objective of this thesis is to develop a control scheme for PMSG-based wind turbine that is capable of injecting a ripple-free active power to the grid under both balanced and unbalanced grid voltages. The proposed control scheme uses a reconfigurable structure that consists of interchanging the roles of power converters depending on the grid voltage conditions. Under balanced grid voltages, the GSC is responsible for regulating the dc-link voltage, while the MSC extracts the maximum power from the wind using the MPPT algorithm. Under unbalanced grid voltages, the MSC takes the responsibility of controlling the dc-link voltage, while the GSC controls the active and reactive power injected into the grid in order to implement FRT control strategy. The control design is based on combining state-feedback control law with disturbance observer approach, resulting in the so-called Disturbance Observer-Based Control (DOBC). The first contribution of this thesis is to adapt the existing disturbance observers to cope with sinusoidal disturbances. The second contribution of this thesis is to use the disturbance observer output to ensure seamless

reconfiguration of the control scheme in response to a sudden balance/unbalance event in grid voltages. The efficacy of the suggested control scheme is assessed using simulation tests. The objectives can be summarized as follows.

- To design and implement two control techniques for GSC, namely, current control scheme and power control scheme. The current control scheme is designed in the dq reference frame, while the power control scheme is designed in the $\alpha\beta$ stationary frame.
- To design and implement a current control scheme for MSC considering both the dq reference frame and the $\alpha\beta$ stationary frame.
- To design and implement a reconfigurable control scheme for the dc-link voltage. The reconfigurable control structure allows interchanging the roles of the power converters in controlling the dc-link voltage considering the grid voltage conditions.
- To ensure fast and seamless reconfiguration of the control scheme in response to sudden balance/unbalance event in grid voltages.
- To mitigate the effect of the inherent dc-link voltage oscillations on the machine torque, particularly when the grid voltage is unbalanced, which is achieved by incorporating a notch filter in the control scheme.
- To evaluate the efficacy of the proposed controller through simulation experiments.

1.4 Relevant Literature

Several research works have aimed to address the concerns regarding the control of PMSG under unbalanced grid voltages. The studies aim to maximize wind energy extraction while making sure that the power delivered to the grid meets the interconnection requirements. The PMSG coupled with a back-to-back voltage source converter provides full controllability of the system. Various control strategies are developed for GSC and MSC to achieve distinct objectives. The objective of the GSC is to control the power delivery to the grid, grid synchronization and to supply high quality power to the grid and to meet grid code

compliance. The goal of the MSC is either to extract maximum power from the wind and or to regulate the dc-link voltage. This section provides a comprehensive analysis and examination of several control techniques. The current methodologies and their respective benefits and drawbacks are examined here. Subsequently, the review has identified the research gap concerning the control of the PMSG.

1.4.1 Voltage-Oriented Control

1.4.1.1 Synchronous Frame VOC with PI Controller

The literature reports that there are different approaches to implement voltage-oriented control to PMSG-based wind turbine. One straightforward approach is to employ a current controller within the dq reference frame. The variables in the dq frame can be obtained by the park transformation, which involves calculating an appropriate angle. For the control of GSC, this angle is called synchronization angle; it is obtained using a synchronization mechanism known as a Phase-Locked Loop (PLL). For the control of PMSG, this angle can be directly measured with a position sensor, or an encoder mounted on the shaft of the rotor. The goal of the controller in the dq reference frame is to precisely align the dq -axis components of the current with their respective references. By decomposing grid currents into d -axis and q -axis components, separate control for active and reactive power can be achieved for GRC [18]. It is important to emphasize that the dq -axis components of the current/voltage are simply a representation of the three-phase current/voltage in a two-phase rotating reference frame. This allows the current/voltage to be represented as a dc quantity which simplifies the analysis and control of the GSC and PMSG. If the three-phase current is unbalanced, the resulting current vector in the natural frame consists of a positive-sequence component revolving in the positive direction and a negative-sequence component rotating in the negative direction. The initial rotating frame is referred to as the positive Synchronous Reference Frame (SRF), whereas the subsequent rotating frame is called the negative SRF. [19]. The positive and negative sequence currents in the positive and negative synchronous reference frame interact, resulting in oscillations at a frequency of 2ω , where ω is the fundamental frequency measured in radians per second. As a result, the negative sequence

current induces oscillations at double the frequency 2ω in the positive sequence current, and vice versa. According to this discovery, the dq -axis components in the dq frame are essentially dc components that can be associated with oscillations occurring at twice the fundamental frequency. To be more specific, the dc component represents the positive sequence component, whereas the double fundamental frequency oscillation indicates the presence of the negative sequence component. When the voltages in the grid are in balance, the currents in the grid are also in balance and exhibit a sinusoidal waveform. This indicates the absence of any negative sequence component. Positive sequence components can accurately characterize both the voltages and currents. In a balanced three-phase system, the sinusoidal currents can be represented as dc components in the dq frame. This reduces the complexity of the control design process. A simple Proportional-Integral (PI) controller can effectively and efficiently manage the dq -axis components of the grid current, guaranteeing stability, precision, robustness, and quick response. Nevertheless, the presence of power grid imbalances caused by faults poses a significant challenge in the design of an inner current controller within the dq frame. The reason for this is that the negative sequence of the dq current manifests as a dual fundamental frequency oscillation around a dc component that represents the positive component. In [20] a voltage oriented controller along with a PI controller is proposed to regulate the dc-link voltage, while the dq -axis current is utilized to control the active and reactive power delivered to the grid. VOC adopts a dual loop control approach, consisting of an outer loop for dc-link voltage regulation and an inner loop for current control. In [20], the active power is utilized to regulate the voltage of the dc-link within the inner control loop. The reactive power is adjusted to zero to ensure unity power factor operation, otherwise it is adjusted based on the grid's specifications. The advantages of VOC strategy include constant switching frequency, low harmonic distortion and simple filter design. It has better control of utilizing the dc voltage.

1.4.1.2 Stationary Frame VOC with PR Controller

Voltage unbalance results in the appearance of second-order harmonics in the dq -axis components of the currents and voltages, this can introduce complexity in the control design within the dq reference frame. More precisely, when implemented in the dq reference frame, controllers are required to ensure accurate tracking of both constant and sinusoidal references oscillating at 2ω to cope with unbalance voltage. To mitigate the challenges associated with developing controllers in the dq reference frame while dealing with unbalanced grid voltages, one can opt to design either current control or power control in the $\alpha\beta$ stationary reference. In this approach, a Proportional Resonant (PR) controller can be employed instead of a PI controller. The reason for this is that the PI controller exhibits infinite gain only for dc quantities. The property of the PI regulator allows it to effectively reject constant disturbances and regulate dc signals with no steady-state error in the synchronous frame. [21,22]. However, PR controller can have infinite gain at specific frequency, which is enough to accurately regulate sinusoidal signals at that frequency [23]. In addition, in order to reduce the dimensionality of the controller, Clarke transformation can be used to convert three-phase signal into orthogonal coordinate $\alpha\beta$. The obtained signals in the $\alpha\beta$ stationary reference are reduced to two and have sinusoidal waveforms with zero dc-components. Therefore, a simple PR controller can be employed to regulate the obtained sinusoidal signals provided that the PR controller has infinite gain at the oscillation frequency.

The advantages of using PR controllers are reduced complexity due to fewer transformations and elimination of decoupling and voltage feed-forward requirements. Additionally, compared to synchronous reference frame control, PR controller offers high dynamic performance and do not require voltage feed-forward to eliminate steady-state error [24]. It should be noted that when grid voltages are unbalanced, the PR controller alone is ineffective for implementing the power control scheme in cases of unbalanced grid voltages. The reason for this is that the instantaneous power fluctuates around a dc component. To ensure the active and reactive power commands are accurately tracked over time, both integral action and resonant action are necessary [25].

1.4.1.3 Hysteresis Current Controllers

Hysteresis Current Controllers (HCC) have been widely utilized due to their ease of implementation without the need for complicated hardware. Another significant benefit of these controllers is their fast-dynamic response and their inherent capacity to limit the peak current injected by the converter. Furthermore, HCC operates independently of any knowledge regarding the system parameters. The fundamental hysteresis current control relies on an on-line Pulse Width Modulation (PWM) control that promptly stabilizes the output voltage of the inverter. The primary function of the PWM current controller in an inverter is to control the output current so that it closely follows its reference. Therefore, it is necessary to decrease the error signal. In classical hysteresis controllers, the error band is typically set to a specific value. As a result, the switching frequency fluctuates within a range because the peak-to-peak current ripple needs to be controlled at every point of the fundamental frequency wave [26]. To address this issue without compromising the effective dynamic performance of the hysteresis current control, a solution is proposed in [27] to implement an adaptive hysteresis band that can maintain a consistent switching frequency. The results demonstrated that the adaptive hysteresis band current control offers better performance than fixed band hysteresis current control. Furthermore, it enables a simpler design of the output filter by ensuring a nearly constant switching frequency. Additionally, the utilization of adaptive hysteresis band current regulation can effectively minimize switching losses.

1.4.1.4 Nonlinear Current Control

The utilization of nonlinear control for PMSG provides numerous benefits in comparison to linear control techniques such as greater tracking performance, improved stability, superior disturbance rejection capabilities, and effective management of energy resources [28].

1.4.1.4.1 Sliding Mode Control

Sliding Mode Control (SMC) is a robust control method commonly used to handle nonlinear systems. SMC is widely recognized for its robustness, precise performance, and simple implementation. It employs a Lyapunov function to design a control law that ensures the system's trajectory converges to a predefined sliding surface. This approach allows SMC to ensure asymptotic regulation even in the presence of internal parameter variations and external disturbances. One of the key advantages of SMC is its ability to effectively reduce a relatively high-order system into a lower-order system, thus simplifying control design [29].

The fundamental concept of SMC is to modify the behavior of the nonlinear system utilizing a discontinuous control signal, which compels the system to align with the predetermined sliding surface [30]. However, the original SMC configuration suffers from chattering phenomena, particularly at stable state as a result of the discontinuous term employed in the SMC structure. This phenomenon leads to unstable system response, and a decline in system performance, impacting the quality of the injected current [31,32]. To address this issue, researchers have introduced advanced variants of SMC, such as High Order Sliding Mode Control (HOSMC) and Terminal Sliding Mode Control (TSMC). HOSMC aims to mitigate the chattering phenomenon while preserving the benefits of the original SMC [33,34]. This is achieved by manipulating higher-order time derivatives of the system's deviation from the constraint. This results in smoother control actions and improved system performance. On the other hand, TSMC focuses on achieving system convergence within a finite time, while maintaining a minimum output control level. This is achieved by incorporating fractional-order components into the control strategy. However, the inclusion of fractional-order variables in the sliding manifold of TSMC introduces singularity issues and may affect system stability. In order to address this, more sophisticated variants of TSMC, such as nonsingular TSMC and fast TSMC, have been proposed aiming to overcome the singularity problem and further enhance control performance [35,36]. An integration of Integral Sliding Mode Control (ISMC) with feedback linearization approach is employed in [37] to enhance its transient performance in the presence of model uncertainty and external

disturbances. The resulting integral sliding surface has a PI-like structure, along with an additional component that serves to maintain the nominal transient performance of the FBL.

1.4.1.4.2 Backstepping Control

Backstepping is a systematic method used to design control systems that can handle non-linear behavior effectively. The fundamental concept of the Backstepping Controller (BSC) involves transforming a complex system into a series of cascaded first-order subsystems. Initially, it is focused on a minor subsystem for which a virtual control law is developed. Subsequently, the design process progresses through multiple stages until the final control law for the entire system is formulated. Therefore, nonlinear systems are transformed into linear systems even in the presence of uncertainty. During the design phase, a Lyapunov function for the controlled system is effectively formulated, providing the stability condition of the closed-loop system. There exist two distinct categories of backstepping techniques. The initial category is referred to as the non-adaptive backstepping control. This technique is employed when the parameters of the analyzed system are already known. The alternative category is referred to as adaptive backstepping control. The adaptation law is employed to approximate the various unknown parameters in a manner that leads them to converge towards their respective values, while ensuring that the general stability of the system remains unaffected. As a result, the system becomes less affected by change in parameters [38]. However, an important limitation of the traditional BSC is the occurrence of a phenomena known as term explosion. This phenomenon happens when virtual inputs undergo many differentiations [39]. Consequently, the complexity of the controller rises, particularly for systems with higher orders, making the practical execution of control more challenging. Several methodologies have been employed to address the aforementioned issue including [40-42].

1.4.1.4.3 Feedback linearization control

Feedback linearization control is an approach that utilizes state feedback and state transformation to algebraically convert a nonlinear system, either partially or wholly, into a linear one. This transformation simplifies the controller design process, enabling systematic control design for the linearized model [43]. The primary concern for the feedback linearization technique is its sensitivity to parameter variations and unknown disturbances. To address this concern, additional control components can be incorporated in the control scheme to enhance robustness against modeling errors. In [44] a feedback linearization controller along with a sliding mode disturbance compensator is employed to enhance disturbance rejection and ensure control robustness in the presence of model uncertainties. In [45] a feedback linearization technique utilizing a double frame controller has been designed to control the positive and negative sequence under unbalanced grid conditions.

Table 1: Comparative analysis of Vector oriented control methodologies

Control Methods	Advantages	Disadvantages
Synchronous VOC with PI Controller	<ul style="list-style-type: none"> • Excellent performance under balanced grid voltages • Fast transient response • High gain 	<ul style="list-style-type: none"> • It is essential to separate active and reactive power • Complicated design to function in situations with imbalanced conditions
Stationary VOC with PR controller	<ul style="list-style-type: none"> • Resonant action property • excellent performance in situations with imbalanced conditions • Straightforward design 	<ul style="list-style-type: none"> • Sensitivity to parameter variations and model uncertainties
Sliding-mode	<ul style="list-style-type: none"> • Robustness against uncertainties • Lower sensitivity to unbalanced voltages 	<ul style="list-style-type: none"> • Chattering effect
Feedback Linearization	<ul style="list-style-type: none"> • Decoupled active and reactive power • Simplified linear model 	<ul style="list-style-type: none"> • Sensitivity to parameter variation and model uncertainties
Backstepping	<ul style="list-style-type: none"> • Resilience to uncertainties • Robust and consistent stability 	<ul style="list-style-type: none"> • Complex stability analysis • Term explosion
Hysteresis	<ul style="list-style-type: none"> • simplicity • Fast dynamics • Increased robustness • Independent of load parameters 	<ul style="list-style-type: none"> • Increased sampling frequency • Variable frequency switching • Higher computing complexity

1.4.2 Direct Power Control

The Direct Power Control (DPC) approach is a simplified version of Voltage-Oriented Control (VOC) strategy. The main focus of the DPC strategy is to accurately and quickly

calculate the active and reactive powers. The DPC schemes differ from VOC approach as they exclude current controllers. They can be categorized into direct control and cascaded control.

The classical Switching-Table-based DPC (ST-DPC) operates on a principle similar to that of direct torque control, employing two hysteresis regulators to choose the desired voltage vector based on a predefined switching table. This method has several key benefits, such as a straightforward design, rapid dynamic response, and immunity to uncertainties in system's parameters. Nevertheless, the utilization of hysteresis comparators in conjunction with the suggested switching tables presents a number of disadvantages, such as fluctuating and high switching frequency [46,47]. To address the issue of variable switching frequency, Space Vector Modulation (SVM) has been introduced along with DPC, replacing the switching table to generate switching pulses [48]. Nonetheless, precise vector selection remains a challenge for these DPC methods.

Model Predictive Control (MPC) has emerged as a solution to enhance the steady-state performance of DPC [49,50]. In MPC, vectors are not derived from a pre-established switching table, but rather acquired by minimizing a cost function. Typically, the cost function is formed by combining the active power and reactive power errors. Using the system model, MPC predicts future reactive and active power values for every switching state and selects the optimal voltage vector that minimizes the cost function. Compared to heuristic switching tables in DPC, the vector selected by MPC showed better accuracy and effectiveness. Finite Control Set Model Predictive Control (FCS-MPC) and Deadbeat Predictive Control are the main branches of MPC [51,52].

In [53-56], DPC with nonlinear techniques are presented. The research work in [53] introduces SMC-based DPC, which combines SVM approach to control the active and reactive powers in the stationary reference frame. In [54], the effectiveness of this control system is enhanced to address unbalanced grid conditions by integrating a power compensation algorithm. This algorithm ensures the production of either sinusoidal and balanced current, the elimination of active power oscillations, or the eradication of reactive

power oscillations. However, when utilizing continuous approximation, relying solely on SMC does not ensure asymptotic tracking in the presence of model uncertainty. Furthermore, it may lead to a chattering effect, which negatively affects the quality of the current by amplifying the magnitude of harmonics. In [55], BSC-DPC is presented by implementing recursive design, where DPC is utilized to construct fuzzy logic as a substitute to switching table for determining the appropriate switching states. This control structure is implemented in [56], focusing on managing the errors in active and reactive powers, while eliminating the use of hysteresis comparators. The benefits of fuzzy logic include straightforward integration and enhanced precision, whilst the drawbacks include the complexity and slow response. However, the author in [57] suggests a power control strategy that involves using the generator-side converter to regulate the dc-link voltage and the grid-side converter to manage the power flow into the grid. During grid faults, the generator-side converter automatically reduces the generator current to maintain the dc voltage, and any resulting acceleration of the generator is counteracted by pitch regulation. To ensure sufficient oscillation damping, an additional active damping loop is incorporated into the generator-side controller. The proposed strategy is simple to implement and does not require any system parameters. However, it does sacrifice the response of the generator-side variables and can cause oscillations in the dc-link voltage.

Table 2:Comparative analysis of direct power control methodologies

Control Methods	Advantages	Disadvantages
Table-based DPC	<ul style="list-style-type: none"> • The need for current and phase-locked loops has been eliminated • Elimination of PWM approaches • Elimination of coordinate transformation 	<ul style="list-style-type: none"> • Variable frequency switching • Increased sampling frequency • Strong sensitivity to changes in inductance • Increased power ripple and THD in current
DPC with SVM	<ul style="list-style-type: none"> • Constant switching frequency • PI controllers can be used 	<ul style="list-style-type: none"> • active and reactive power are decoupled • Difficult design to function in an unbalanced grid • Tuning effort
Sliding-mode	<ul style="list-style-type: none"> • Resilience to distortions • Reduced sensitivity to voltage imbalances • switching frequency is constant 	<ul style="list-style-type: none"> • Chattering effect • Higher complexity
Backstepping	<ul style="list-style-type: none"> • Resilience to uncertainties • Robust and consistent stability • switching frequency is constant 	<ul style="list-style-type: none"> • Complex stability analysis
Fuzzy logic	<ul style="list-style-type: none"> • Simple control design • high accuracy • switching frequency is constant 	<ul style="list-style-type: none"> • Slow response • Increased complexity
Finite-control-set predictive control	<ul style="list-style-type: none"> • Simplicity of the control design • Ensures optimal selection of vectors • Reduced power ripple and decreased sensitivity 	<ul style="list-style-type: none"> • Variable switching frequency • High sampling frequency • High complexity in three-vector approach
Deadbeat predictive control	<ul style="list-style-type: none"> • switching frequency is constant • Wide bandwidth enables accurate tracking of sinusoidal signals • No power error 	<ul style="list-style-type: none"> • Sensitive to change in parameters • Need for precise model details

1.4.3 Maximum Power Point Tracking

Wind turbines operate within a specific range of wind speeds, limited by the cut-in and cut-out speeds. For every wind speed value, there is an optimal rotor speed at which the PMSG can extract the maximum available power from the wind. A Maximum Power Point Tracking (MPPT) algorithm is a tool that can generate the optimal rotor speed for a given wind speed value so that the PMSG-based wind turbine can operate at its maximal power capability. Therefore, it is important to incorporate an MPPT algorithm into the control of PMSG-based wind turbine to accurately identify the optimum operating point. Lookup table-based strategies are the most utilized MPPT methods. These methods rely on either a pre-programmed 2D lookup table that contains stored values of the ideal generator speed and the corresponding maximum power at different wind speeds, or a cubic (quadratic) mapping function that generates a reference signal for the optimal turbine power at the operating generator speed. This section provides a literature review of various MPPT control algorithms.

1.4.3.1 Tip Speed Ratio (TSR) Control

The Tip Speed Ratio (TSR) control aims at keeping the TSR at an optimal value in order to extract maximum available power from the wind. This can be achieved by controlling the rotor speed at an optimal value that is computed in real-time from the optimal value of the TSR considering the measured value of the wind speed. This method involves comparing the optimal rotor speed with its actual value and providing the resulting difference to the controller. The controller then adjusts the speed of the generator to minimize this error. The main drawback of this approach is the requirement for an accurate wind speed measurement, which subsequently increases the overall cost of the device[58,59].

1.4.3.2 Optimal Torque (OT) Control

The fundamental idea of this approach is to control the torque of the PMSG to follow an optimal torque reference given by either a curve or a lookup table. This reference curve is derived from experimental tests. The benefits of this strategy include its simplicity, rapid

response, and high efficiency. However, it is important to note that this method relies on accurate information regarding air density and turbine mechanical parameters, which can vary across different systems. Furthermore, the optimal torque curve, primarily acquired through experimentation in the field, will undergo alterations when the system undergoes aging. This will impact the efficiency of the MPPT system [60-62].

1.4.3.3 Power Signal Feedback (PSF) Control

The Power Signal Feedback (PSF) method introduced in [63] aims at minimizing the error between the optimal power and the actual power by means of a controller. The optimal power is generated by either utilizing a pre-determined power-speed curve or by employing the equation for turbine output power. However, prior to implementing this technique, it is necessary to get the optimum power curve of the wind turbine. The data points for the highest output power and the corresponding wind turbine speed are stored in a lookup table or a function that uses the product of the cube of the measured rotational speed with the optimum proportionality constant. While this technique is commonly employed in wind power generation systems, it necessitates the utilization of the optimal power-speed curve, which in turn necessitates the conduct of aerodynamic testing. Furthermore, these attributes can undergo significant alterations over time due to external causes such as the accumulation of dirt and ice on the turbine blades [64].

1.4.3.4 Perturbation and Observation (P&O) Control

The Perturbation and Observation (P&O) algorithm[65-67], also known as the Hill Climb Search (HCS) MPPT algorithm, is a mathematical optimization strategy utilized to locate the local optimum point of a specified function. This approach relies on perturbing a control variable by a small step size and observing the consequences of the alterations in the target function until the slope reaches zero, i.e., if the operating point is located to the left of the peak point, the controller must shift it towards the right in order to approach the peak point. Conversely, if the operating point is on the right side, it should be moved towards the left. The P&O algorithms can be categorized based on the step-sizes they create and the tracking approach they employ. The step-sizes can be categorized into fixed, variable,

adaptive, and hybrid. However, these classes do not illustrate the operating policy and performance evaluation of the P&O algorithms. The tracking approach can be categorized into conventional and modified algorithm groups. The traditional algorithms are classified into fixed and adjustable step-sizes algorithms. The modified P&O algorithms are classified into subcategories, such as dividing the power curve, adopting a generic objective function, combining optimization approaches, and employing hybrid methods [68]. The P&O algorithm is commonly employed in wind power generation systems due to its simplicity and flexibility. In addition, it does not necessitate previous knowledge with the wind turbine's characteristic curve. Nevertheless, it is unable to achieve the highest power output levels when subjected to fast fluctuations in wind speed, particularly when employed for wind turbines with significant mass and rotational inertia. Moreover, a significant limitation that may lead to the failure tracking process is the absence of differentiation between the power variations caused by the wind shift and those resulting from the preceding perturbation.

1.4.3.4 Other MPPT Control

Advanced MPPT controllers have been developed to surpass the conventional algorithms mentioned earlier. Among these controllers is the Hybrid MPPT algorithm, which combines two or more MPPT algorithms. In [64] PSF and HCS controllers are combined to create a sensorless and flexible method that can be used for all wind turbine levels. In addition, artificial intelligence controllers have been introduced in the field of MPPT control. An example of these controllers is the Fuzzy Logic Control for MPPT (FLC-MPP) [69], which offers benefits such as rapid convergence, insensitivity to parameter variations, and the ability to handle noisy and imprecise signals. However, the effectiveness of FLC-MPPT heavily relies on the user's knowledge in selecting the appropriate error, levels of membership functions, and rule-based table. The implementation of the system is limited by its memory needs [70]. Due to the advancement of soft computing methods, the use of Neural Network (NN) algorithms has greatly expanded in MPPT applications. NN-MPPT techniques have been employed to address the challenges related to measuring wind speed. These techniques enable the estimation of wind speed based on the real torque and speed of the machine[71].

Table 3: Comparison of MPPT control techniques

Control Methods	Advantages	Disadvantages
Tip speed ratio control	<ul style="list-style-type: none"> • Simple • High efficiency 	<ul style="list-style-type: none"> • Requires anemometer • High cost
Optimal torque control	<ul style="list-style-type: none"> • Simple • Fast • Fast tracking 	<ul style="list-style-type: none"> • Low efficiency • Depends on the prior knowledge of WT characteristics • Sensitive to climate conditions
Power signal feedback control	<ul style="list-style-type: none"> • Robust • Low cost • Reduction of the steady- state oscillation around MPP 	<ul style="list-style-type: none"> • Low efficiency • Requires the optimal power-speed curve • Requires memory
Perturbation and observation control	<ul style="list-style-type: none"> • Flexible • Simple • Does not require prior knowledge of WT parameters or anemometers 	<ul style="list-style-type: none"> • Failure in MPP tracking occurs during wind speed variation
Hybrid techniques	<ul style="list-style-type: none"> • Simple • Highly efficient • Mitigate the drawbacks of conventional MPPT algorithms 	<ul style="list-style-type: none"> • Depends on the combined MPPT techniques
Fuzzy logic control	<ul style="list-style-type: none"> • Quick response • Parameter insensitivity 	<ul style="list-style-type: none"> • Increased complexity • Requires memory
Neural Network control	<ul style="list-style-type: none"> • Robust operation • Fast tracking 	<ul style="list-style-type: none"> • Requires a long offline training • Increased complexity

1.4.4 Disturbance Observer Based Control

The Disturbance and Uncertainty Estimation and Attenuation (DUEA) is an advanced control strategy used in dynamic systems to attenuate the effects of disturbances and model uncertainties. Literature reveals that a number of studies have been conducted to apply the DUEA technique to renewable energy conversion systems. Among the widely approaches for implementing DUEA concept is Disturbance Observer-Based Control (DOBC). DOBC involves integrating a disturbance observer into the control loop, allowing the system to accurately estimate and counteract the effect of unknown disturbances in real-time. The key feature of DOBC is its ability to achieve accurate tracking of reference signal thanks to the exact rejection of the effect of modeling errors and unknown disturbances. Compared to conventional controllers, DOBC can also meet the transient response specifications even in the presence of model uncertainties and unknown disturbances. More precisely, it may achieve recovery of nominal transient performance provided that the disturbance estimator has a sufficiently high speed. The property of nominal performance recovery allows the closed-loop system to track a predefined nominal transient response, even in the presence of uncertainties and unknown disturbances. The DOBC structure consists of an outside loop that includes the controller and the plant, and an inner loop that includes the Disturbance Observer (DO). The output of the DO is subsequently inputted into the controller to mitigate the effects of the disturbance [72]. The review in [72] classifies DUEA methodologies into two categories: Linear Disturbance and Uncertainty Estimation (LDUE) techniques, and Nonlinear Disturbance and Uncertainty Estimation (NDUE) techniques. The LDUE method entails neglecting the nonlinear aspect of the controlled nonlinear system and treating it as a component of the lumped disturbance. The lumped disturbance refers to the combined representation of uncertainty and disturbance. LDUE methodologies, such as the frequency domain disturbance observer, Extended State Observer (ESO), and Unknown Input Observer (UIO), have the ability to precisely measure the influence of nonlinearity and efficiently compensate for it. LDUE methods are applicable to both linear and nonlinear systems, provided that the nonlinear state equation does not include substantial nonlinearities.

Advanced methodologies, referred to as NDUE, were implemented to achieve outstanding results in nonlinear systems. These methodologies include the basic Nonlinear Disturbance Observer (NDO), higher order NDO, and Extended High-Gain State Observer (EHGSO). The DO techniques is first proposed in 1983 [73], where a controller with an integrator was designed to achieve optimal performance by mitigating uncertainties in the plant and canceling external disturbances using their estimations through disturbance observer.

This thesis aims at applying the DOBC approach to PMSG-based wind turbine with a view to enhance its performance in the presence of balanced and unbalanced grid voltages. The DOBC approach is applied to GSC to design a power control scheme in the stationary frame and a current control scheme in the synchronous frame. In MSC, DOBC approach is used to regulate the machine current aiming to achieve precise regulation and excellent dynamic performance. The DOBC is also applied to develop a robust controller for the dc-link voltage under both balanced and unbalanced grid voltages. As pointed out above, the performance of the DOBC approach mainly relies on the accuracy of the disturbance observer. For robust control design, the disturbance input can be used to represent the effect of model uncertainties, unknown perturbations, and unmeasurable inputs. The main challenge for designing an accurate disturbance observer is the need for the exact dynamics of the disturbance input, which is generally assumed to be very slow compared to the system's variables, e.g., constant disturbance input. For PMSG-based wind turbine, this assumption can be valid only in the dq reference frame and in the presence of balanced grid voltages, where dq -axis components of current and voltage eventually converge to constant steady-state values. Such an assumption, however, does not hold true under unbalanced grid voltages due to the fact that the dq -axis components of grid current and grid voltage may experience 2ω oscillations around dc components. Trying to find the exact dynamics of a disturbance input that represents modelling errors and unknown perturbations may be difficult or even impossible. Instead, it is reasonable to assume that the disturbance input and the state variables have the same dynamics, at least during steady-state [74]. Such an assumption has been applied in several research works and has been proved to be effective in practice. This assumption is used in this thesis to develop DOBC for PMSG-based wind aiming to improve

its performance under both balanced and unbalanced grid voltages considering both synchronous frame and stationary frame.

Chapter 2: Mathematical Model

Understanding the mathematical model and reference frames of a grid-tied inverter connected to a Permanent Magnet Synchronous Generator PMSG is crucial for designing an effective controller. A mathematical model provides a simplified representation of the real-world system. By understanding the model, we can perform accurate simulations to analyze how the grid-tied inverter and PMSG interact under various conditions. This helps in predicting system behavior, identifying potential issues, and optimizing controller parameters before implementation. Mathematical models help in designing control algorithms that can regulate important variables like output voltage, frequency, and power factor. With a solid understanding of the system's dynamics, controllers can easily be designed to maintain grid synchronization, manage power flow, and respond to disturbances effectively. Certain machine inductances vary with the rotor's position, resulting in rotor-position-dependent coefficients within the differential equations (voltage equations) that characterize the machines' behavior. This often leads to the utilization of a change of variables as a strategy to simplify the intricacy of these differential equations[75]. Initially, various distinct changes of variables were believed to be unique and treated separately. However, it was subsequently discovered that these variable changes, designed to transform actual variables, can be unified under a single general transformation. This comprehensive transformation involves aligning machine variables with a rotating reference frame of arbitrary angular velocity from which all recognized real transformations can be derived by adjusting the reference frame's rotational speed.

2.1 Mathematical Model of Grid-tied Inverter

2.1.1 Mathematical Model in the Natural Frame

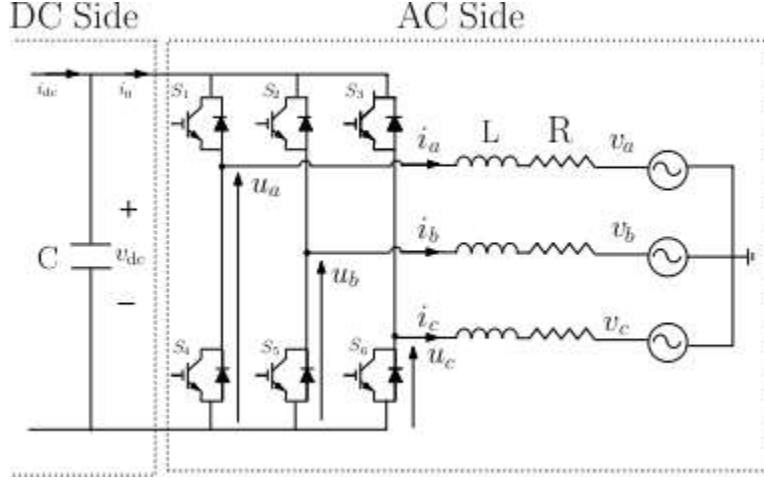


Figure 3: Ac and dc side of a three-phase rectifier.

The dynamics of grid currents can be described by three differential equations derived from the applying Kirchoff's voltage law on the AC side in Figure 3.

$$u_a = v_a + L \frac{di_a}{dt} + Ri_a \quad (2.1)$$

$$u_b = v_b + L \frac{di_b}{dt} + Ri_b \quad (2.2)$$

$$u_c = v_c + L \frac{di_c}{dt} + Ri_c \quad (2.3)$$

The three equations provided can be reorganized in the following manner:

$$\frac{di_{abc}}{dt} = -\frac{R}{L} i_{abc} + \frac{1}{L} u_{abc} - \frac{1}{L} v_{abc} \quad (2.4)$$

where i_{abc} represents the current flowing through the grid, v_{abc} represents the voltage across the grid, and u_{abc} represents the voltage across the converter. The parameters R and L represent the resistance and inductance of the filter, respectively. The aforementioned model can be reformulated utilizing a matrix representation as

$$\begin{bmatrix} \frac{di_a}{dt} \\ \frac{di_b}{dt} \\ \frac{di_c}{dt} \end{bmatrix} = -\frac{R}{L} \begin{bmatrix} i_a \\ i_b \\ i_c \end{bmatrix} + \frac{1}{L} \begin{bmatrix} u_a \\ u_b \\ u_c \end{bmatrix} - \frac{1}{L} \begin{bmatrix} u_a \\ u_b \\ u_c \end{bmatrix} \quad (2.5)$$

2.1.2 Mathematical Model in the Stationary $\alpha\beta$ Reference Frame

Clarke's transformation is a method that alters variables in order to convert three-phase signals into two stationary axes. This methodology offers the benefit of not needing to employ Phase-Locked Loop (PLL) methods to compute the phase angle of the grid. In addition, the reference frame simplifies the analysis of unbalanced three-phase systems. This is due to the fact that current references and grid voltages are presumed to fluctuate at the frequency of the grid, even in cases where the grid voltages are unbalanced. The formula for the transformation is provided as follows:

$$X_{\alpha\beta o} = \begin{bmatrix} X_\alpha \\ X_\beta \\ X_o \end{bmatrix} = \left(\frac{2}{3}\right)^m \begin{bmatrix} 1 & -\frac{1}{2} & -\frac{1}{2} \\ 0 & \frac{\sqrt{3}}{2} & -\frac{\sqrt{3}}{2} \\ \frac{1}{2^m} & \frac{1}{2^m} & \frac{1}{2^m} \end{bmatrix} X_{abc} = \left(\frac{2}{3}\right)^m \begin{bmatrix} 1 & -\frac{1}{2} & -\frac{1}{2} \\ 0 & \frac{\sqrt{3}}{2} & -\frac{\sqrt{3}}{2} \\ \frac{1}{2^m} & \frac{1}{2^m} & \frac{1}{2^m} \end{bmatrix} \begin{bmatrix} X_a \\ X_b \\ X_c \end{bmatrix} \quad (2.6)$$

where X_α and X_β are the α -axis component of X and the β -axis component of X , respectively. X_0 is called zero-sequence component of X . Here, X can be either current, voltage, or machine flux. To conserve the current amplitude (amplitude-invariant), the number m is set equal to $m = 1$, resulting in the so-called Clarke's transformation. To conserve the instantaneous power constant (power-invariant), the number m is set equal to $m = 0.5$, resulting in the so-

called Concordia transformation. In this thesis, Clarke's transformation is adopted, which can be achieved by setting $m = 1$. That is:

$$C_{\alpha\beta} = \frac{2}{3} \begin{bmatrix} 1 & -\frac{1}{2} & -\frac{1}{2} \\ 0 & \frac{\sqrt{3}}{2} & -\frac{\sqrt{3}}{2} \\ \frac{1}{2} & \frac{1}{2} & \frac{1}{2} \end{bmatrix}, \quad C_{\alpha\beta}^{-1} = \begin{bmatrix} 1 & 0 & 1 \\ -\frac{1}{2} & \frac{\sqrt{3}}{2} & 1 \\ -\frac{1}{2} & -\frac{\sqrt{3}}{2} & 1 \end{bmatrix} \quad (2.7)$$

On the other hand, as stated in [76], the grid-tied inverter does not display the zero-sequence component in the $\alpha\beta 0$ frame, due to the absence of connection between the negative side of the dc bus capacitor and the neutral point, a certain issue arises. Therefore, the final row in $C_{\alpha\beta}$, which represents the zero-sequence component, can be omitted in the Clarke's transformation., resulting in

$$C_{\alpha\beta} = \frac{2}{3} \begin{bmatrix} 1 & -\frac{1}{2} & -\frac{1}{2} \\ 0 & \frac{\sqrt{3}}{2} & -\frac{\sqrt{3}}{2} \end{bmatrix}, \quad C_{\alpha\beta}^{-1} = \begin{bmatrix} 1 & 0 \\ -\frac{1}{2} & \frac{\sqrt{3}}{2} \\ -\frac{1}{2} & -\frac{\sqrt{3}}{2} \end{bmatrix} \quad (2.8)$$

Thus, one can write:

$$\begin{bmatrix} X_\alpha \\ X_\beta \end{bmatrix} = C_{\alpha\beta} \begin{bmatrix} X_a \\ X_b \\ X_c \end{bmatrix}, \quad \begin{bmatrix} X_a \\ X_b \\ X_c \end{bmatrix} = C_{\alpha\beta}^{-1} \begin{bmatrix} X_\alpha \\ X_\beta \end{bmatrix} \quad (2.9)$$

By applying Clarke's transformation to the model in equation (2.5), the mathematical representation of the grid-tied inverter can be reformulated in the $\alpha\beta$ reference frame. To accomplish this, one can multiply both sides of the equation (2.5) by the factor $C_{\alpha\beta}$

$$C_{\alpha\beta} \begin{bmatrix} \frac{di_a}{dt} \\ \frac{di_b}{dt} \\ \frac{di_c}{dt} \end{bmatrix} = C_{\alpha\beta} \left(-\frac{R}{L} \begin{bmatrix} i_a \\ i_b \\ i_c \end{bmatrix} + \frac{1}{L} \begin{bmatrix} u_a \\ u_b \\ u_c \end{bmatrix} - \frac{1}{L} \begin{bmatrix} v_a \\ v_b \\ v_c \end{bmatrix} \right) \quad (2.10)$$

Now, by substituting (2.8) into (2.10), the mathematical model of the grid-tied inverter can be rewritten in the $\alpha\beta$ reference frame as shown below.

$$\frac{d}{dt} \begin{bmatrix} i_\alpha \\ i_\beta \end{bmatrix} = -\frac{R}{L} \begin{bmatrix} i_\alpha \\ i_\beta \end{bmatrix} + \frac{1}{L} \begin{bmatrix} u_\alpha \\ u_\beta \end{bmatrix} - \frac{1}{L} \begin{bmatrix} v_\alpha \\ v_\beta \end{bmatrix} \quad (2.11)$$

where i_α and i_β are the α -axis current and the β -axis current, respectively. u_α and u_β are the α -axis voltage and the β -axis voltage at the output of the inverter, respectively. Similarly, v_α and v_β are the α -axis grid voltage and the β -axis grid voltage, respectively.

2.1.3 Mathematical Model in the Synchronous dq Reference Frame

The Park transformation enables the direct conversion of a model from the natural frame to its synchronous frame. Another useful method is to employ the dq transformation to obtain the synchronous reference frame model from the stationary reference frame model obtained in (2.11). By ignoring the zero-sequence component, the dq transformation is represented by:

$$\begin{bmatrix} X_d \\ X_q \end{bmatrix} = C_{dq} \begin{bmatrix} X_\alpha \\ X_\beta \end{bmatrix}, \quad \begin{bmatrix} X_\alpha \\ X_\beta \end{bmatrix} = C_{dq}^{-1} \begin{bmatrix} X_d \\ X_q \end{bmatrix} \quad (2.12)$$

where

$$C_{dq} = \begin{bmatrix} \cos(\theta) & \sin(\theta) \\ -\sin(\theta) & \cos(\theta) \end{bmatrix}, \quad C_{dq}^{-1} = \begin{bmatrix} \cos(\theta) & -\sin(\theta) \\ \sin(\theta) & \cos(\theta) \end{bmatrix} \quad (2.13)$$

The parameter $\theta = \omega t$ represents the grid voltage-phase angle, sometimes referred to as the synchronization angle, and it can be determined from grid voltage measurements using the Phase-Locked Loop (PLL) algorithm. Here, ω is the frequency of the grid voltage in rad/s. To derive the mathematical model in the dq reference frame, one can use the dq transformation as

$$\frac{d}{dt} \begin{bmatrix} i_d \\ i_q \end{bmatrix} = \frac{d}{dt} \left(C_{dq} \begin{bmatrix} i_\alpha \\ i_\beta \end{bmatrix} \right) = -\omega \begin{bmatrix} \sin(\theta) & -\cos(\theta) \\ \cos(\theta) & \sin(\theta) \end{bmatrix} \begin{bmatrix} i_\alpha \\ i_\beta \end{bmatrix} + C_{dq} \frac{d}{dt} \begin{bmatrix} i_\alpha \\ i_\beta \end{bmatrix} \quad (2.14)$$

where i_d and i_q are the d -axis current and the q -axis current, respectively. The differential equations governing the behavior of the grid currents in the dq frame can be derived by substituting (2.11) along with (2.13) into (2.14), yielding

$$\begin{aligned} \frac{d}{dt} \begin{bmatrix} i_d \\ i_q \end{bmatrix} &= -\omega \begin{bmatrix} \sin(\theta) & -\cos(\theta) \\ \cos(\theta) & \sin(\theta) \end{bmatrix} \begin{bmatrix} i_\alpha \\ i_\beta \end{bmatrix} + C_{dq} \left(-\frac{R}{L} \begin{bmatrix} i_\alpha \\ i_\beta \end{bmatrix} + \frac{1}{L} \begin{bmatrix} u_\alpha \\ u_\beta \end{bmatrix} - \frac{1}{L} \begin{bmatrix} v_\alpha \\ v_\beta \end{bmatrix} \right) \\ &= -\omega \begin{bmatrix} \sin(\theta) & -\cos(\theta) \\ \cos(\theta) & \sin(\theta) \end{bmatrix} C_{dq}^{-1} \begin{bmatrix} i_d \\ i_q \end{bmatrix} - \frac{R}{L} \begin{bmatrix} i_d \\ i_q \end{bmatrix} + \frac{1}{L} \begin{bmatrix} u_d \\ u_q \end{bmatrix} - \frac{1}{L} \begin{bmatrix} v_d \\ v_q \end{bmatrix} \\ &= -\omega \begin{bmatrix} \sin(\theta) & -\cos(\theta) \\ \cos(\theta) & \sin(\theta) \end{bmatrix} \begin{bmatrix} \cos(\theta) & -\sin(\theta) \\ \sin(\theta) & \cos(\theta) \end{bmatrix} \begin{bmatrix} i_d \\ i_q \end{bmatrix} - \frac{R}{L} \begin{bmatrix} i_d \\ i_q \end{bmatrix} + \frac{1}{L} \begin{bmatrix} u_d \\ u_q \end{bmatrix} - \frac{1}{L} \begin{bmatrix} v_d \\ v_q \end{bmatrix} \end{aligned} \quad (2.15)$$

u_d and u_q are the d -axis voltage and the q -axis voltage at the output of the inverter, respectively. Similarly, v_d and v_q are the d -axis grid voltage and the q -axis grid voltage, respectively. The final model in the dq reference frame can be further simplified into

$$\frac{d}{dt} \begin{bmatrix} i_d \\ i_q \end{bmatrix} = -\omega \begin{bmatrix} 0 & -1 \\ 1 & 0 \end{bmatrix} \begin{bmatrix} i_d \\ i_q \end{bmatrix} - \frac{R}{L} \begin{bmatrix} i_d \\ i_q \end{bmatrix} + \frac{1}{L} \begin{bmatrix} u_d \\ u_q \end{bmatrix} - \frac{1}{L} \begin{bmatrix} v_d \\ v_q \end{bmatrix} \quad (2.16)$$

The synchronization angle θ is often determined by setting v_q to zero, aligning the d -axis with the fundamental of the grid voltage. When considering the specific angle θ , the grid-tied inverter model in the synchronous reference is simplified to:

$$\frac{d}{dt} \begin{bmatrix} i_d \\ i_q \end{bmatrix} = -\frac{R}{L} \begin{bmatrix} i_d \\ i_q \end{bmatrix} + \begin{bmatrix} -\omega i_d \\ \omega i_q \end{bmatrix} + \frac{1}{L} \begin{bmatrix} u_d \\ u_q \end{bmatrix} - \frac{1}{L} \begin{bmatrix} v_d \\ 0 \end{bmatrix} \quad (2.17)$$

2.1.4 Mathematical Model Using P and Q as State Variables

The previous stationary reference frame model in (2.11), which is required for the construction of a current controller in the reference frame, is stated in terms of grid currents as state variables. To develop a power control system, it is necessary to use a mathematical model that includes active and reactive powers as state variables. The power computations in the $\alpha\beta$ reference frame can be mathematically represented as

$$P = \frac{3}{2}(v_\alpha i_\alpha + v_\beta i_\beta), \quad Q = \frac{3}{2}(v_\beta i_\alpha - v_\alpha i_\beta) \quad (2.18)$$

where P and Q are the active and reactive powers, respectively. By differentiating **Error! Reference source not found.**, the time derivative of the active and reactive powers can be obtained in the following manner

$$\begin{aligned} \frac{dP}{dt} &= \frac{3}{2} \left(\frac{dv_\alpha}{dt} i_\alpha + \frac{dv_\beta}{dt} i_\beta + v_\alpha \frac{di_\alpha}{dt} + v_\beta \frac{di_\beta}{dt} \right) \\ \frac{dQ}{dt} &= \frac{3}{2} \left(\frac{dv_\beta}{dt} i_\alpha - \frac{dv_\alpha}{dt} i_\beta + v_\beta \frac{di_\alpha}{dt} - v_\alpha \frac{di_\beta}{dt} \right) \end{aligned} \quad (2.18)$$

During balanced grid conditions, the voltage magnitude of v_α is equivalent to that of v_β . Hence, the rate of change of v_α and v_β over time fulfills:

$$\frac{dv_\alpha}{dt} = -\omega v_\beta, \quad \frac{dv_\beta}{dt} = \omega v_\alpha \quad (2.19)$$

Substituting (2.11) and (2.19) into (2.18) results in

$$\begin{aligned} \frac{d}{dt} \begin{bmatrix} P \\ Q \end{bmatrix} &= \frac{3}{2} \omega \begin{bmatrix} -v_\beta & v_\alpha \\ v_\alpha & v_\beta \end{bmatrix} \begin{bmatrix} i_\alpha \\ i_\beta \end{bmatrix} + \frac{3}{2} \begin{bmatrix} v_\alpha & v_\beta \\ v_\beta & -v_\alpha \end{bmatrix} \left(-\frac{R}{L} \begin{bmatrix} i_\alpha \\ i_\beta \end{bmatrix} + \frac{1}{L} \begin{bmatrix} u_\alpha \\ u_\beta \end{bmatrix} - \frac{1}{L} \begin{bmatrix} v_\alpha \\ v_\beta \end{bmatrix} \right) \\ &= \frac{3}{2} \omega \begin{bmatrix} -v_\beta & v_\alpha \\ v_\alpha & v_\beta \end{bmatrix} \begin{bmatrix} i_\alpha \\ i_\beta \end{bmatrix} - \frac{3}{2L} \left(R \begin{bmatrix} v_\alpha & v_\beta \\ v_\beta & -v_\alpha \end{bmatrix} \begin{bmatrix} i_\alpha \\ i_\beta \end{bmatrix} - \begin{bmatrix} v_\alpha & v_\beta \\ v_\beta & -v_\alpha \end{bmatrix} \begin{bmatrix} u_\alpha \\ u_\beta \end{bmatrix} + \begin{bmatrix} v_\alpha & v_\beta \\ v_\beta & -v_\alpha \end{bmatrix} \begin{bmatrix} v_\alpha \\ v_\beta \end{bmatrix} \right) \end{aligned} \quad (2.20)$$

which can be further simplified as

$$\begin{aligned} \frac{d}{dt} \begin{bmatrix} P \\ Q \end{bmatrix} &= \frac{3}{2} \omega \begin{bmatrix} -Q \\ P \end{bmatrix} - \frac{3}{2L} \left(R \begin{bmatrix} P \\ Q \end{bmatrix} - \begin{bmatrix} v_\alpha & v_\beta \\ v_\beta & -v_\alpha \end{bmatrix} \begin{bmatrix} u_\alpha \\ u_\beta \end{bmatrix} + \begin{bmatrix} v_\alpha & v_\beta \\ v_\beta & -v_\alpha \end{bmatrix} \begin{bmatrix} v_\alpha \\ v_\beta \end{bmatrix} \right) \\ &= \frac{3}{2} \begin{bmatrix} -\frac{R}{L} & -\omega \\ \omega & -\frac{R}{L} \end{bmatrix} \begin{bmatrix} P \\ Q \end{bmatrix} + \frac{3}{2L} \begin{bmatrix} v_\alpha & v_\beta \\ v_\beta & -v_\alpha \end{bmatrix} \begin{bmatrix} u_\alpha \\ u_\beta \end{bmatrix} - \frac{3}{2L} \begin{bmatrix} v_\alpha^2 + v_\beta^2 \\ 0 \end{bmatrix} \end{aligned} \quad (2.21)$$

Thus, one can write:

$$\begin{bmatrix} \dot{P} \\ \dot{Q} \end{bmatrix} = \frac{3}{2} \begin{bmatrix} -\frac{R}{L} & -\omega \\ \omega & -\frac{R}{L} \end{bmatrix} \begin{bmatrix} P \\ Q \end{bmatrix} + \frac{3}{2L} \begin{bmatrix} v_\alpha & v_\beta \\ v_\beta & -v_\alpha \end{bmatrix} \begin{bmatrix} u_\alpha \\ u_\beta \end{bmatrix} - \begin{bmatrix} \frac{3}{2L} \\ 0 \end{bmatrix} V_M^2 \quad (2.22)$$

where

$$V_M = \sqrt{v_\alpha^2 + v_\beta^2} \quad (2.23)$$

In this context, V_M denotes the maximum value of the grid voltage. let $u_{PQ} = [u_{Peq} \quad u_{Qeq}]^T$ be the control that is equal to or corresponds to the active and reactive powers is such that:

$$\begin{bmatrix} u_{Peq} \\ u_{Qeq} \end{bmatrix} = \begin{bmatrix} v_\alpha & v_\beta \\ v_\beta & -v_\alpha \end{bmatrix} \begin{bmatrix} u_\alpha \\ u_\beta \end{bmatrix} \quad (2.24)$$

Substituting (2.24) into (2.22) leads to

$$\begin{bmatrix} \dot{P} \\ \dot{Q} \end{bmatrix} = \frac{3}{2} \begin{bmatrix} -\frac{R}{L} & -\omega \\ \omega & -\frac{R}{L} \end{bmatrix} \begin{bmatrix} P \\ Q \end{bmatrix} + \frac{3}{2L} \begin{bmatrix} u_{peq} \\ u_{Qeq} \end{bmatrix} - \begin{bmatrix} \frac{3}{2L} \\ 0 \end{bmatrix} V_M^2 \quad (2.25)$$

Therefore, it can be demonstrated that the elements of u_{peq} and u_{Qeq} remain constant throughout balanced steady-state circumstances. Under balanced grid voltages, any basic controller, such as a PI regulator, can be used to effectively regulate the active and reactive powers. However, controlling the active and reactive powers under unbalanced grid voltages involves a careful choice of the control design as the equivalent control may not be constant at steady state.

2.2 Mathematical Model of Permanent Magnet Synchronous Generator

2.2.1 Aerodynamic Model of Wind Turbine

The wind turbine captures power from wind and then converts it into mechanical power. The amount of aerodynamic torque T_r is related to the wind speed as follows [77]

$$T_r = 0.5 \rho \pi R_b^2 \frac{v_w^2}{\omega_r} C_p(\lambda, \beta) \quad (2.26)$$

where ρ is the air density, R_b is the rotor plane radius, v_w is the wind speed, and C_p is the power coefficient, β is the pitch angle of the rotor, ω_r is the turbine rotor speed, and λ is the tip speed ratio which is a ratio between the linear velocity ($R_b \omega_r$) of the blade tip and the wind velocity v_w ; that is

$$\lambda = \frac{\omega_r R_b}{v_w} \quad (2.27)$$

The extracted aerodynamic power P_r is given by:

$$P_r = T_r \omega_r = 0.5 \rho \pi R^2 v_w^3 C_p(\lambda, \beta) \quad (2.28)$$

The previous equation can be rewritten in terms of the blades swept area A as

$$P_r = 0.5 \rho A C_p(\lambda, \beta) \times \left(\frac{\omega_r R_b}{\lambda} \right)^3 \quad (2.29)$$

Here, $C_p(\lambda, \beta)$ is the performance coefficient of the wind turbine which is a nonlinear function depending on the blade pitch angle β and tip speed ratio λ . $C_p(\lambda, \beta)$ can be expressed as

$$C_p(\lambda, \beta) = \frac{1}{2} \left(\frac{116}{\lambda_i} - 0.4\beta - 5 \right) e^{-\left(\frac{21}{\lambda_i}\right)} \quad (2.30)$$

where

$$\frac{1}{\lambda_i} = \frac{1}{\lambda + 0.08\beta} - \frac{0.035}{\beta^3 + 1} \quad (2.31)$$

According to [78], for a given value of β , the plot of the nonlinear coefficient $C_p(\lambda, \beta)$ as a function of λ shows a concave behavior. In other words, for a given value of β , the nonlinear coefficient $C_p(\lambda, \beta)$ has a maximum value that corresponds to a specific value of λ , denoted by λ_{opt} . From (2.27), it follows that, for a given wind speed v_w (m/s), the optimal value λ_{opt} corresponds to an optimal value of the rotor speed, denoted by ω_{r-opt} and given by

$$\omega_{r-opt} = \frac{v_w}{R_b} \lambda_{opt} \quad (2.32)$$

In summary, for a given wind speed v_w (m/s), wind turbine can capture the maximum available power from wind if the rotor speed can be regulated at ω_{r-opt} , leading to the so-called Maximum Power Point Tracking (MPPT).

2.2.2 Mathematical Model of PMSG in the Natural abc Reference Frame

This section is concerned with the derivation of the PMSG model, which is the same as the model of permanent magnet synchronous motor PMSM. The only difference between the PMSM model and the PMSG model is the direction of the stator winding current. Figure 4 depicts the model of a three-phase PMSM along with a three-phase power converter.

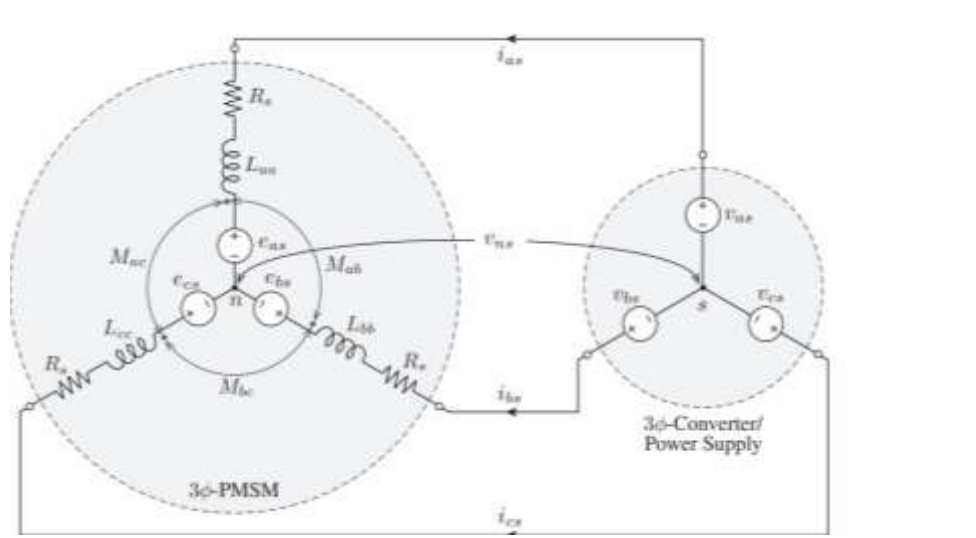


Figure 4: Model of PMSG along with a three-phase power converter.

As illustrated in the diagram, the machine's neutral point is disconnected from the power converter. The current direction is gauged from the power converter to the PMSG. By applying Kirchhoff's voltage law, it can easily be shown that the PMSG stator voltages v_{as} , v_{bs} , and v_{cs} are expressed as [49]

$$\begin{aligned}
 v_{as} &= R_s i_{as} + \frac{d\psi_{as}}{dt} + v_{ns} \\
 v_{bs} &= R_s i_{bs} + \frac{d\psi_{bs}}{dt} + v_{ns} \\
 v_{cs} &= R_s i_{cs} + \frac{d\psi_{cs}}{dt} + v_{ns}
 \end{aligned} \tag{2.33}$$

where ψ_{as} , ψ_{bs} , and ψ_{cs} are stator flux linkages, i_{as} , i_{bs} , and i_{cs} are stator currents of PMSG, and R_s represents the machine stator winding resistance, v_{ns} is the machine neutral-point voltage. The above model can be rewritten in a matrix form as

$$\begin{bmatrix} v_{as} \\ v_{bs} \\ v_{cs} \end{bmatrix} = \begin{bmatrix} R_s & 0 & 0 \\ 0 & R_s & 0 \\ 0 & 0 & R_s \end{bmatrix} \begin{bmatrix} i_{as} \\ i_{bs} \\ i_{cs} \end{bmatrix} + \frac{d}{dt} \begin{bmatrix} \psi_{as} \\ \psi_{bs} \\ \psi_{cs} \end{bmatrix} + \begin{bmatrix} v_{ns} \\ v_{ns} \\ v_{ns} \end{bmatrix} \quad (2.34)$$

The stator flux linkages in the abc frame result from both the permanent magnetic flux linkages and the current that flows through the self and mutual inductances of the machine. That is,

$$\begin{bmatrix} \psi_{as} \\ \psi_{bs} \\ \psi_{cs} \end{bmatrix} = \begin{bmatrix} L_{aa} & M_{ab} & M_{ac} \\ M_{ab} & L_{bb} & M_{bc} \\ M_{ac} & M_{bc} & L_{cc} \end{bmatrix} \begin{bmatrix} i_{as} \\ i_{bs} \\ i_{cs} \end{bmatrix} + \begin{bmatrix} \psi_r \cos(p\theta_r) \\ \psi_r \cos\left(p\theta_r - \frac{2\pi}{3}\right) \\ \psi_r \cos\left(p\theta_r - \frac{4\pi}{3}\right) \end{bmatrix} \quad (2.35)$$

where L_{aa} , L_{bb} , and L_{cc} are the machine phase abc self-inductances, M_{ab} , M_{bc} , and M_{ac} , are the machine mutual inductances between phase abc . Here, ψ_r is the peak value of flux linkage created by the permanent magnets, while p is the number of pole pairs. The parameter θ_r represents the mechanical angle in rad. The expressions of L_{aa} , L_{bb} , L_{cc} , M_{ab} , M_{bc} , and M_{ac} are given by:

$$\begin{cases} L_{aa} = l_f + L_0 - L_{ms} \cos(2p\theta_r) \\ L_{bb} = l_f + L_0 - L_{ms} \cos(2p\theta_r - 2\pi/3) \\ L_{cc} = l_f + L_0 - L_{ms} \cos(2p\theta_r + 2\pi/3) \end{cases} \quad (2.36)$$

And

$$\begin{cases} M_{ab} = M_{ba} = L_0 \cos(2\pi/3) - L_{ms} \cos(2p\theta_r - 2\pi/3) \\ M_{ac} = M_{ca} = L_0 \cos(4\pi/3) - L_{ms} \cos(2p\theta_r + 2\pi/3) \\ M_{bc} = M_{cb} = L_0 \cos(2\pi/3) - L_{ms} \cos(2p\theta_r - 2\pi) \end{cases} \quad (2.37)$$

where L_0 , l_f , and L_{ms} are due to leakage flux and magnetization. It is important to emphasize that, for a non-salient pole machine, the magnetization inductance is equal to zero, i.e., $L_{ms} = 0$. The expression of the torque T_e of the machine can be derived by considering the co-energy of the machine. When it does so, one can show that:

$$T_e = \frac{1}{2} i_s^T \frac{dL_{s2}(\theta)}{d\theta} i_s - i_s^T p \psi_r \begin{bmatrix} \sin(p\theta_r) & \sin(p\theta_r - 2\pi/3) & \sin(p\theta_r + 2\pi/3) \end{bmatrix}^T \quad (2.38)$$

where the current i_s is given by

$$i_s = \begin{bmatrix} i_{as} & i_{bs} & i_{cs} \end{bmatrix}^T \quad (2.39)$$

The term is given by $L_{s2}(\theta)$ is expressed as

$$L_{s2}(\theta) = -L_{ms} \begin{bmatrix} \cos(2p\theta_r) & \cos 2(p\theta_r - \pi/3) & \cos 2(p\theta_r + \pi/3) \\ \cos 2(p\theta_r - \pi/3) & \cos 2(p\theta_r - 2\pi/3) & \cos(2p\theta_r) \\ \cos 2(p\theta_r + \pi/3) & \cos(2p\theta_r) & \cos 2(p\theta_r + 2\pi/3) \end{bmatrix} \quad (2.40)$$

It is clear that, for a non-salient machine, the expression of the torque reduces to

$$T_e = -i_s^T p \psi_r \begin{bmatrix} \sin(p\theta_r) & \sin(p\theta_r - 2\pi/3) & \sin(p\theta_r + 2\pi/3) \end{bmatrix}^T \quad (2.41)$$

2.2.3 Mathematical Model of PMSG in the Stationary Frame

As before, by applying Clarke transformation to (2.35), the expression of the flux can be rewritten in the $\alpha\beta$ reference frame as

$$\begin{bmatrix} \psi_{\alpha s} \\ \psi_{\beta s} \end{bmatrix} = \begin{bmatrix} l_f + \frac{3L_0}{2} - \frac{3L_{ms}}{2} \cos(2p\theta_r) & -\frac{3L_{ms}}{2} \sin(2p\theta_r) \\ -\frac{3L_{ms}}{2} \sin(2p\theta_r) & l_f + \frac{3L_0}{2} + \frac{3L_{ms}}{2} \cos(2p\theta_r) \end{bmatrix} \begin{bmatrix} i_{\alpha s} \\ i_{\beta s} \end{bmatrix} + \psi_r \begin{bmatrix} \cos(p\theta_r) \\ \sin(p\theta_r) \end{bmatrix} \quad (2.42)$$

where $\psi_{\alpha s}$ and $\psi_{\beta s}$ are the α -axis and β -axis components of the flux, while $i_{\alpha s}$ and $i_{\beta s}$ are the α -axis and β -axis components of the stator current. In the case of a non-salient pole machine, one can put $L_{ms} = 0$ in the above equation to obtain:

$$\begin{bmatrix} \psi_{\alpha s} \\ \psi_{\beta s} \end{bmatrix} = \begin{bmatrix} l_f + \frac{3L_0}{2} & 0 \\ 0 & l_f + \frac{3L_0}{2} \end{bmatrix} \begin{bmatrix} i_{\alpha s} \\ i_{\beta s} \end{bmatrix} + \psi_r \begin{bmatrix} \cos(p\theta_r) \\ \sin(p\theta_r) \end{bmatrix} \quad (2.43)$$

Similarly, the voltage equations can be reformulated in the $\alpha\beta$ reference frame by implementing the Clarke transformation. (2.34), yielding

$$\begin{bmatrix} v_{\alpha s} \\ v_{\beta s} \end{bmatrix} = R_s \cdot I_{2 \times 2} \cdot \begin{bmatrix} i_{\alpha s} \\ i_{\beta s} \end{bmatrix} + \frac{d}{dt} \begin{bmatrix} \psi_{\alpha s} \\ \psi_{\beta s} \end{bmatrix} \quad (2.44)$$

where $v_{\alpha s}$ and $v_{\beta s}$ are the α -axis voltage and β -axis voltage, respectively. The voltage equations for a non-salient machine can be obtained by substituting $L_{ms} = 0$ in the flux equations (2.41), yielding:

$$\begin{bmatrix} \frac{di_{\alpha s}}{dt} \\ \frac{di_{\beta s}}{dt} \end{bmatrix} = \begin{bmatrix} -\frac{R_s}{L_{cs}} & 0 \\ 0 & -\frac{R_s}{L_{cs}} \end{bmatrix} \cdot \begin{bmatrix} i_{\alpha s} \\ i_{\beta s} \end{bmatrix} + \frac{p}{L_{cs}} \psi_r \begin{bmatrix} \sin(p\theta_r) \\ -\cos(p\theta_r) \end{bmatrix} \frac{d\theta_r}{dt} + \begin{bmatrix} \frac{v_{\alpha s}}{L_{cs}} \\ \frac{v_{\beta s}}{L_{cs}} \end{bmatrix} \quad (2.45)$$

where

$$L_{cs} = l_f + \frac{3L_0}{2} \quad (2.46)$$

Let θ_e be the electrical angle, it is expressed as a function of the mechanical angle θ_r as follows:

$$\theta_e = p\theta_r, \quad \theta_r = \omega_r t, \quad \Rightarrow \theta_e = p\omega_r t = \omega_e t, \quad \omega_e = p\omega_r \quad (2.47)$$

where ω_e is the electrical angular speed in rad/s. In other words, ω_e is the frequency of the stator voltage in rad/s. The voltage equations can be described in state space form as

$$\dot{x}_m = A_m x_m + B_m u_m + F_m \quad (2.48)$$

where

$$A_m = \begin{bmatrix} \frac{-R_s}{L_{cs}} & 0 \\ 0 & \frac{-R_s}{L_{cs}} \end{bmatrix}, \quad B_m = \begin{bmatrix} \frac{1}{L_{cs}} & 0 \\ 0 & \frac{1}{L_{cs}} \end{bmatrix}, \quad F_m = \frac{\omega_e}{L_{cs}} \psi_r \begin{bmatrix} -\sin(\theta_e) \\ \cos(\theta_e) \end{bmatrix} \quad (2.49)$$

And

$$u_m = \begin{bmatrix} v_{\alpha s} \\ v_{\beta s} \end{bmatrix}, \quad x_m = \begin{bmatrix} i_{\alpha s} \\ i_{\beta s} \end{bmatrix} \quad (2.50)$$

The torque T_e can also be rewritten in the $\alpha\beta$ reference frame. Towards this end, recall that:

$$i_s = C_{\alpha\beta}^{-1} \begin{bmatrix} i_{\alpha s} \\ i_{\beta s} \end{bmatrix} \quad (2.51)$$

By using the above equation in the expression of the torque T_e , one can show that:

$$T_e = p \begin{bmatrix} i_{\alpha s} & i_{\beta s} \end{bmatrix} \left(\frac{3L_{ms}}{2} \begin{bmatrix} \sin(2\theta_e) & -\cos(2\theta_e) \\ -\cos(2\theta_e) & -\sin(2\theta_e) \end{bmatrix} \begin{bmatrix} i_{\alpha s} \\ i_{\beta s} \end{bmatrix} - \frac{3}{2} \psi_r \begin{bmatrix} \sin(\theta_e) \\ -\cos(\theta_e) \end{bmatrix} \right) \quad (2.52)$$

For a non-salient machine, the above expression of the torque reduces to

$$T_e = -p \frac{3}{2} \begin{bmatrix} i_{\alpha s} & i_{\beta s} \end{bmatrix} \psi_r \begin{bmatrix} \sin(\theta_e) \\ -\cos(\theta_e) \end{bmatrix} = p \frac{3}{2} \psi_r (i_{\beta s} \cos(\theta_e) - i_{\alpha s} \sin(\theta_e)) \quad (2.53)$$

2.2.4 Mathematical Model of PMSG in the Synchronous Frame

2.2.4.1 Stator Voltages in Synchronous Frame d -axis current and the q -axis current

By breaking down the steady-state stator phase current into two parts, one aligned with the Electromagnetic Field (EMF) and the other shifted by 90° , two stator Magneto Motive Forces (MMFs) can be identified. Both of these MMFs, moving at rotor speed, were observed. The first one generates a field in the air gap, reaching its peak alignment with the rotor poles d -axis. Meanwhile, the second MMF is aligned with the q -axis. The primary objective of the

$d - q$ model is to remove the reliance of inductances on the rotor's position. In order to achieve this, it's necessary to affix the coordinate system to the specific part of the machine that exhibits magnetic saliency [79]. The transition from an abc frame model to a dq frame involves a two-stage procedure: first, the abc models presented in equations (2.34) is transformed into a stationary frame using the abc to $\alpha\beta$ conversion; subsequently, the $\alpha\beta$ frame models are transitioned into dq a frame via $\alpha\beta$ to dq transformation. The resulting dq frame voltage equations are derived from equation (2.34)

$$\begin{bmatrix} v_{ds} \\ v_{qs} \end{bmatrix} = \begin{bmatrix} R_s & 0 \\ 0 & R_s \end{bmatrix} \begin{bmatrix} i_{ds} \\ i_{qs} \end{bmatrix} + \frac{d}{dt} \begin{bmatrix} \psi_{ds} \\ \psi_{qs} \end{bmatrix} + \begin{bmatrix} 0 & -\omega_e \\ \omega_e & 0 \end{bmatrix} \begin{bmatrix} \psi_{ds} \\ \psi_{qs} \end{bmatrix} \quad (2.54)$$

where v_{ds} and v_{qs} are the machine stator voltages in dq frame, i_{ds} and i_{qs} are the machine stator currents in dq frame, ψ_{ds} and ψ_{qs} are the machine stator flux linkages in dq frame. By comparing Equation (2.34) to Equation (2.54) , it is evident that the conversion involves transforming the three-phase voltages, currents, and flux linkages into their corresponding dq variables. Notably, the stator neutral-point voltage, v_{ns} is excluded from the machine model during the abc to $\alpha\beta$ transformation. The final term within Equation (2.54) corresponds to the induced voltages, often referred to as speed voltages. The $\alpha\beta$ to dq transformation commonly results in speed voltages within various three-phase systems, including electric machines, power converters, and harmonic filters. The dq frame standard model for the PMSG, as established by Equation(2.54) , is depicted in Figure 5.

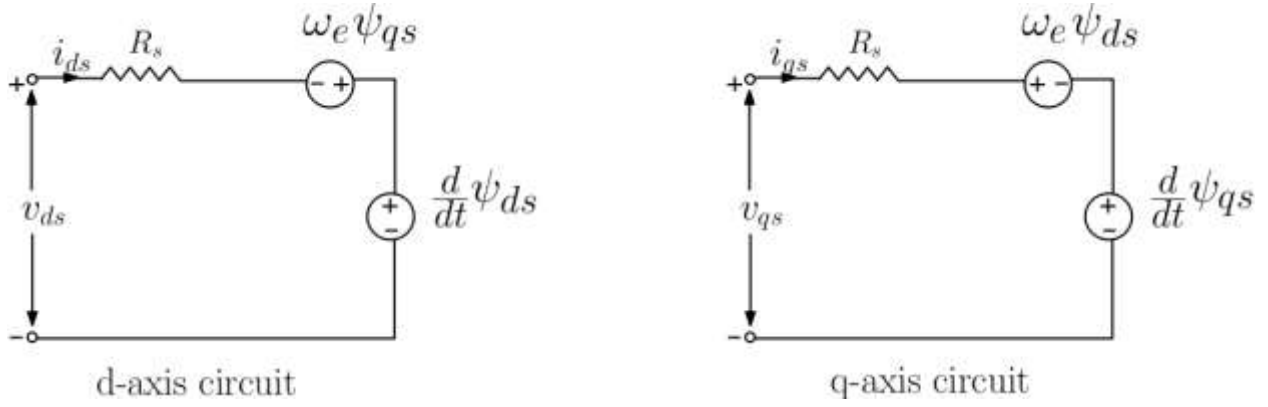


Figure 5: dq frame model for the PMSG.

2.2.4.2 Stator Flux Linkages in Synchronous Frame

In a corresponding manner, the $\alpha\beta$ -frame magnetic linkage values presented in equation (2.35) are transformed into the dq frame.

$$\begin{bmatrix} \psi_{ds} \\ \psi_{qs} \end{bmatrix} = \begin{bmatrix} l_f + \frac{3L_0}{2} - \frac{3L_{ms}}{2} & 0 \\ 0 & l_f + \frac{3L_0}{2} + \frac{3L_{ms}}{2} \end{bmatrix} \begin{bmatrix} i_{ds} \\ i_{qs} \end{bmatrix} + \psi_r \begin{bmatrix} 1 \\ 0 \end{bmatrix} \quad (2.55)$$

which can be rewritten as

$$\begin{bmatrix} \psi_{ds} \\ \psi_{qs} \end{bmatrix} = \begin{bmatrix} L_{ds} & 0 \\ 0 & L_{qs} \end{bmatrix} \begin{bmatrix} i_{ds} \\ i_{qs} \end{bmatrix} + \begin{bmatrix} \psi_r \\ 0 \end{bmatrix} \quad (2.56)$$

where

$$L_{ds} = l_f + \frac{3L_0}{2} - \frac{3L_{ms}}{2}, \quad L_{qs} = l_f + \frac{3L_0}{2} + \frac{3L_{ms}}{2} \Rightarrow L_{ms} = \frac{L_{qs} - L_{ds}}{3} \quad (2.57)$$

In the dq reference frame the parameters L_{ds} and L_{qs} in addition to ψ_r become time-invariant unlike in the natural abc frame where these parameters vary with the change of the rotor electrical position angle θ_e due to this circumstance the modeling and control in dq frame is simplest.

2.2.4.3 Stator Current Dynamics in Synchronous Frame

In the context of control design, the focus is directed towards the derivative of the stator currents to address the relationship combining equation (2.54) along with (2.56) resulting in the following relation

$$\begin{bmatrix} v_{ds} \\ v_{qs} \end{bmatrix} = \begin{bmatrix} R_s & -L_{qs}\omega_e \\ L_{ds}\omega_e & R_s \end{bmatrix} \begin{bmatrix} i_{ds} \\ i_{qs} \end{bmatrix} + \begin{bmatrix} L_{ds} & 0 \\ 0 & L_{qs} \end{bmatrix} \frac{d}{dt} \begin{bmatrix} i_{ds} \\ i_{qs} \end{bmatrix} + \begin{bmatrix} 0 \\ \omega_e \psi_r \end{bmatrix} \quad (2.58)$$

The model of PMSG in dq reference frame based on the previous stator voltage dynamic model is expressed in Figure 6. The stator current dynamic can be expressed from the model (2.3) which represents the state space in continuous time CT model which can be directly used for the control design in this thesis.

$$\frac{d}{dt} \begin{bmatrix} i_{ds} \\ i_{qs} \end{bmatrix} = \begin{bmatrix} -\frac{R_s}{L_{ds}} & \frac{L_{qs}}{L_{ds}} \omega_e \\ -\frac{L_{qs}}{L_{qs}} \omega_e & -\frac{R_s}{L_{qs}} \end{bmatrix} \begin{bmatrix} i_{ds} \\ i_{qs} \end{bmatrix} + \begin{bmatrix} \frac{1}{L_{ds}} & 0 \\ 0 & \frac{1}{L_{qs}} \end{bmatrix} \begin{bmatrix} v_{ds} \\ v_{qs} \end{bmatrix} + \begin{bmatrix} 0 \\ -\frac{\psi_r \omega_e}{L_{qs}} \end{bmatrix} \quad (2.59)$$

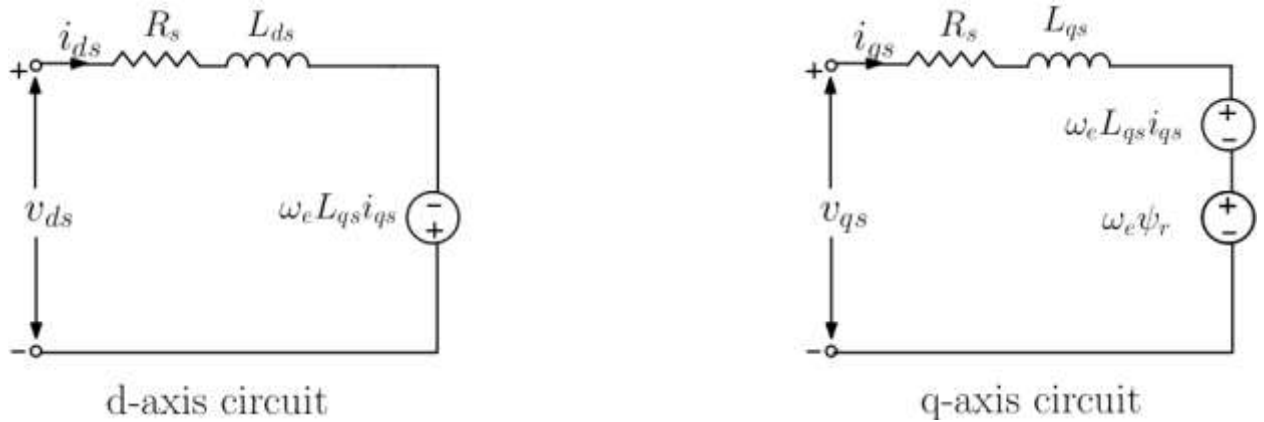


Figure 6: dq frame model for the PMSG including stator voltage dynamics.

2.2.4.4 Stator Active and Reactive Power in Synchronous Frame

The connection between the apparent power of the stator and the dq components of stator voltages and currents is formulated in the subsequent manner.

$$\begin{aligned} P_s &= \frac{3}{2}(v_{ds}i_{ds} + v_{qs}i_{qs}) \\ Q_s &= \frac{3}{2}(v_{qs}i_{ds} - v_{ds}i_{qs}) \end{aligned} \quad (2.60)$$

After substituting the v_{ds} and v_{qs} values from (2.54) into (2.60), the stator active and reactive power are expressed as follows:

$$\begin{aligned} P_s &= \frac{3}{2}R_s(i_{ds}^2 + i_{qs}^2) + \frac{3}{2}\left(i_{ds}\frac{d\psi_{ds}}{dt} + i_{qs}\frac{d\psi_{qs}}{dt}\right) + \frac{3}{2}\omega_e(\psi_{ds}i_{qs} - \psi_{qs}i_{ds}) \\ Q_s &= \frac{3}{2}\left(i_{ds}\frac{d\psi_{qs}}{dt} - i_{qs}\frac{d\psi_{ds}}{dt}\right) + \frac{3}{2}\omega_e(\psi_{ds}i_{ds} + \psi_{qs}i_{qs}) \end{aligned} \quad (2.61)$$

In the power equation, the initial component signifies the resistive losses within the stator winding, the subsequent element accounts for the energy stored in the magnetic field, and the final component represents the air gap power P_m that gives rise to the generation of torque T_e .

2.2.5 Electromagnetic Torque

The relationship between the torque and the power is given by:

$$P_m = T_e \omega_r = \frac{T_e \omega_e}{p} \quad (2.62)$$

where

$$T_e = \frac{P_m p}{\omega_e} \quad (2.63)$$

Upon replacing the third element of power equation (2.61), which pertains to the generation of torque within equation (2.63), the resultant expression yields the electromagnetic torque in the subsequent manner

$$T_e = \frac{3p}{2} \left[\psi_r i_{qs} + (L_{ds} - L_{qs}) i_{ds} i_{qs} \right] \quad (2.64)$$

2.3 Dynamics of the DC-link Voltage

By utilizing Kirchhoff's current law in the analysis of the dc circuit, one can get the differential equation that accurately represents the behavior of the dc voltage as

$$C \frac{dv_{dc}}{dt} = i_{dc} - i_0 \quad (2.65)$$

where the capacitor C , referred to as the dc-link capacitor, is utilized to mitigate the fluctuations in the dc voltage, i_{dc} refers to the dc current, while i_0 represents the input current of the grid-tied inverter. In this context, v_{dc} denotes the voltage across the dc-link capacitor.

2.3.1 Model for DC-link Voltage under Balanced Grid Voltages

Under balanced grid voltages, the grid-tied inverter is employed to regulate the dc-link voltage by adjusting the current i_0 injected into the grid-tied inverter. This can be achieved through the control of either the grid current or the active power injected into the grid. To see this, note that the current i_0 can be expressed as a function of the dc-link voltage and the power that flows through the three-phase inverter; that is:

$$i_0 = \frac{P_{dc}}{v_{dc}} \quad (2.66)$$

where P_{dc} is the dc power at the input of the three-phase inverter. From (2.65) and (2.66), it follows that

$$\frac{dv_{dc}}{dt} = \frac{i_{dc}}{C} - \frac{P_{dc}}{Cv_{dc}} \quad (2.67)$$

Now, ignoring power converter and filter losses, it is reasonable to assume that the dc power P_{dc} at the input of the grid-tied inverter is equal to the ac power P delivered to the grid, resulting in

$$P_{dc} = P \quad (2.68)$$

In the natural reference frame, the instantaneous power P delivered to the grid, is given by:

$$P = v_a i_a + v_b i_b + v_c i_c \quad (2.69)$$

Hence, substituting (2.69) into (2.67), gives

$$\frac{dv_{dc}}{dt} = \frac{i_{dc}}{C} - \frac{v_a i_a + v_b i_b + v_c i_c}{C v_{dc}} \quad (2.70)$$

In the $\alpha\beta$ reference frame, the power P represents the active power; that is:

$$P = \frac{3}{2} (v_\alpha i_\alpha + v_\beta i_\beta) \quad (2.71)$$

Hence, substituting (2.71) into (2.67), gives

$$\frac{dv_{dc}}{dt} = \frac{i_{dc}}{C} - \frac{3(v_\alpha i_\alpha + v_\beta i_\beta)}{2C v_{dc}} \quad (2.72)$$

In the dq synchronous reference frame, the power P can be rewritten as

$$P = \frac{3}{2} (v_d i_d + v_q i_q) \quad (2.73)$$

Hence, substituting (2.73) into (2.67), gives

$$\frac{dv_{dc}}{dt} = \frac{i_{dc}}{C} - \frac{3(v_d i_d + v_q i_q)}{2Cv_{dc}} \quad (2.74)$$

The synchronization angle θ is typically determined by setting v_q to zero, which aligns the d -axis with the fundamental of the grid voltage. At this specific angle θ , the active and reactive powers supplied to the grid reduce to

$$P = \frac{3}{2} v_d i_d, \quad Q = -\frac{3}{2} v_d i_q \quad (2.75)$$

which implies

$$\frac{dv_{dc}}{dt} = \frac{i_{dc}}{C} - \frac{3v_d}{2Cv_{dc}} i_d \quad (2.76)$$

The above equations indicate that the reactive power Q can be controlled by adjusting the q -axis current. In particular, the grid-tied inverter can operate at unity power factor by setting the command value of i_q to be equal to zero. On the other hand, the dc-link voltage can be regulated by controlling either the active power P or the d -axis current of the grid current. It is important to emphasize that the current i_{dc} is assumed to be unknown in (2.76), which mandates the need for a tight controller to ensure a stable and accurate regulation of the dc-link voltage.

2.3.2 Model for DC-link Voltage under Unbalanced Grid Voltages

Under unbalanced grid voltages, grid-tied inverter should be able to inject appropriate active and reactive powers to the grid to satisfy the so-called Fault Ride-Through (FRT) requirement. This requirement can be met by considering the grid-tied inverter for the control of the active and reactive powers injected into the grid, while the dc-link voltage regulation can be achieved through the use of the machine side converter. In particular, the dc-link voltage can be regulated by adjusting the torque of the PMSG to follow an appropriate command value. To see this, note that the current i_{dc} can be rewritten as a function of the dc-link voltage and the power delivered by the PMSG; that is:

$$i_{dc} = \frac{P_G}{v_{dc}} \quad (2.77)$$

where P_G is the electrical power produced by the PMSG. Thus, (2.65) reduces to

$$\frac{dv_{dc}}{dt} = \frac{P_G}{C} - \frac{i_0}{C} \quad (2.78)$$

Here, the current i_0 is assumed to be unknown. It's worth noting that the torque equation mentioned above is applicable when the system operates as a motor. Consequently, the expression for the electrical power generated by PMSG can be formulated as follows.

$$P_G = -T_e \omega_r \quad (2.79)$$

Substituting (2.79) into (2.78) yields

$$\frac{dv_{dc}}{dt} = -\frac{\omega_r}{C} T_e - \frac{i_0}{C} \quad (2.80)$$

Recall that:

$$T_e = \frac{3p}{2} (\psi_r i_{qs} + (L_{ds} - L_{qs}) i_{qs} i_{ds}) \quad (2.81)$$

When controlling PMSG, it's common practice to regulate the d-axis current i_{ds} at zero. As a result, it is possible to formulate the following expression.

$$\frac{dv_{dc}}{dt} = -\frac{3p\psi_r\omega_r}{2v_{dc}C} i_{qs} - \frac{i_0}{C} \quad (2.82)$$

It is important to emphasize that the current i_0 is assumed to be unknown, which mandates the need for a tight controller to ensure a stable and accurate regulation of the dc-link voltage.

2.4 Summary

This chapter has introduced the mathematical representation of a two-level grid-tied inverter and Permanent Magnet Synchronous Generator (PMSG) in three distinct reference frames: the natural frame, stationary frame, and synchronous frame. Moreover, the grid model was acquired by considering the active and reactive powers as state variables to facilitate designing a power controller for grid-tied inverter. The machine model was derived by representing machine currents as state variables that need to be regulated. The mathematical models described in this chapter will be subsequently employed in the upcoming chapters to facilitate designing accurate controllers for PMSG and grid-tied inverter under both balanced and unbalanced grid voltages.

Chapter 3: Control of PMSG-Based Wind Energy Generation System in Stationary Reference $\alpha\beta$ Frame

The interaction between a PMSG-based wind turbine and a balanced grid is a dynamic and intricate process, involving multiple facets such as power quality, synchronization, and stability. The control algorithms employed must not only regulate the electrical power output to match the grid demand but also ensure that the generator's mechanical and electrical systems work harmoniously. Achieving such a coordination demands a profound understanding of the intricate interplay between the PMSG's mechanical dynamics, electrical characteristics, and the grid's requirements. This chapter embarks on a comprehensive exploration of the control strategies including the design, analysis, and simulation tests tailored for PMSG-based wind turbine in scenarios where the grid operates under balanced and unbalanced conditions. This research aims to contribute to the enhancement of the overall efficiency, reliability, and seamless integration of wind energy systems into grids. The converter used to control the power exchange between the grid and the PMSG is back-to-back converter which consists of a Machine-Side Converter (MSC) and a Grid-Side Converter (GSC) that are interconnected through a dc-link capacitor. This chapter mainly focuses on designing robust controllers for both converters GSC and MSC to cope with both balanced and unbalanced grid voltages.

During unbalanced grid voltage, the existence of the negative sequence component of the grid voltage causes the generation of second-order harmonic oscillations in the grid-side active power and dc-link voltage. Injecting oscillating active power into the grid represents a violation of the grid code regulation which requires the delivered active power to be devoid of any ripples. Another concern of voltage unbalance is due to the dc-link voltage ripples that can have an adverse impact on the response of the torque developed by the generator. This impact can result in high torque ripples, which can in turn lead to unwanted vibrations, thus reducing the durability and the lifetime of the drive-train that is used to connect the generator to the wind turbine. The torque ripples can be attributed to the propagation of dc-link voltage oscillations into the stator currents. The objective of this chapter is to apply DOBC approach

to design robust controllers for GSC and MSC with a view to regulate the dc-link voltage, inject constant active power to the grid under both balanced and unbalanced grid voltages, extract the maximum available power from the wind during balanced voltages, and maintain ripple-free machine torque.

This chapter presents the design, development, and performance testing of a reconfigurable control scheme for GSC and MSC. The word “reconfigurable” comes from the fact that both GCS and MSC interchange their roles when the grid conditions change. In the balanced case, the GSC is responsible for controlling the dc-link voltage through the use of a cascade control scheme that consists of two loops. In this cascade structure, the outer loop is used to regulate the dc-link voltage, while the inner loop is used to control the grid power using $\alpha\beta$ coordinates. In this case, the main function of MSC is limited to extracting the maximum available power from the wind, which is achieved by controlling the torque of PMSG to follow an appropriate command value provided by Maximum Power Point Tracking (MPPT) algorithm. In this chapter, the control of the torque machine is assured by adjusting the $\alpha\beta$ -axis components of the stator currents to follow specific references. However, during unbalanced grid conditions, the role of GSC can be restricted to assure only the control of active and reactive powers delivered to the grid in order to allow implementing Fault Ride Through (FRT) control strategy [52]. In such a case, MSC assures the regulation of the dc-link voltage via the employment of a cascade control scheme. In this cascade structure, the outer loop is employed to maintain dc-link voltage at its command value, while the inner loop is designed to control the stator currents of the machine using $\alpha\beta$ coordinates. All controllers for both cases are designed based on DOBC approach, which consists of combining a state-feedback controller with a disturbance observer. The structure of the disturbance observer is generally featured with either integral action property, resonant action property, or both of them to achieve accurate tracking of both sinusoidal and constant signal references. Integral/resonant action property remains the main concern for employing disturbance observer as it requires appropriate initialization for achieving a fast disturbance estimation. Note that the faster the disturbance observer, the smaller the tracking error during transients. Therefore, if the disturbance observer associated with the control of the dc-link voltage can

be accurately initialized after the change of the grid conditions, a smooth interchange of the roles of the converters can be achieved. In other words, a good initialization of the disturbance observer associated with the control of the dc-link voltage ensures that the dc-link voltage can remain close to its command value in response to sudden changes in the grid conditions. In the proposed control scheme, the disturbance observer can easily be initialized by considering the disturbance estimation just before the voltage balance/unbalance event occurs. Such an advantage cannot be offered by classical controllers such as PI and PR controllers. It remains to address the concern of torque ripples under unbalanced grid voltages, which are caused by the inherent dc-link voltage oscillations. This concern is overcome in this thesis by applying a notch filter to the measurement of the dc-link voltage before feeding it into the dc-link voltage controller in order to cancel the effect of 2ω oscillations. As a result, only dc component of dc-link voltage measurement is fed into the voltage regulator, which is enough to prevent the propagation of 2ω oscillations to the command value for the inner current loop.

Several simulation studies were performed to verify the efficacy of this control technique. The findings obtained have verified the effectiveness of the inner loop control method in accurately tracking the grid power references and machine stator current references, regardless of whether the grid conditions are balanced or unbalanced. Figure 7 illustrates a comprehensive cascaded power control strategy in the $\alpha\beta$ stationary frame.

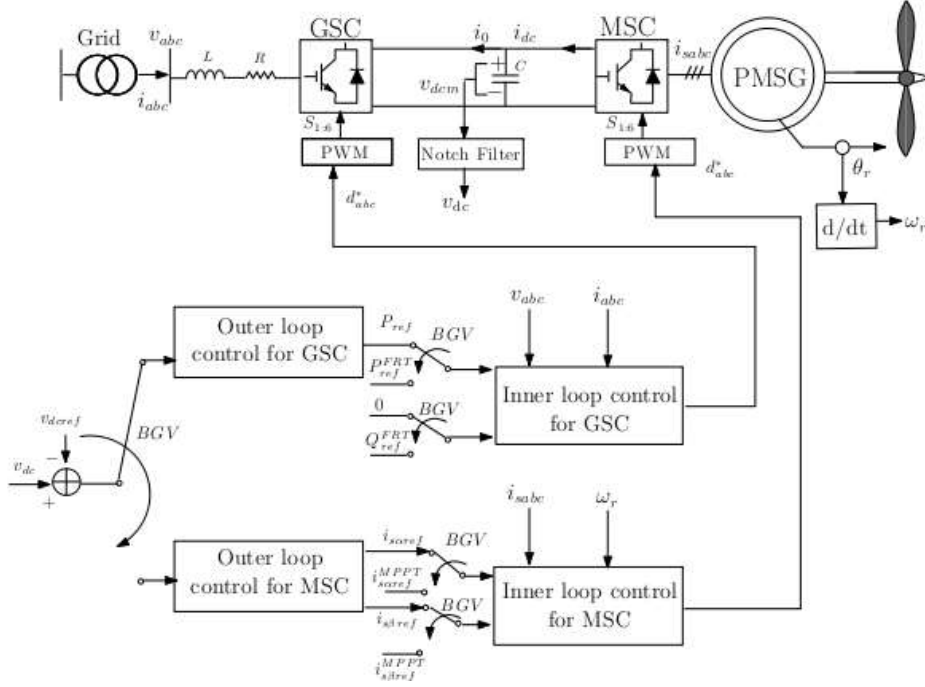


Figure 7: General power control scheme.

3.1 Power Control of the Grid-Side Converter

3.1.1 Perturbed Model of the Grid-Side Converter

The model of the grid-tied inverter, with P and Q are the state variables, is given below as presented in (2.21)

$$\frac{d}{dt} \begin{bmatrix} P \\ Q \end{bmatrix} = \begin{bmatrix} -\frac{R}{L} & -\omega \\ \omega & -\frac{R}{L} \end{bmatrix} \begin{bmatrix} P \\ Q \end{bmatrix} + \frac{3}{2L} \begin{bmatrix} v_\alpha & v_\beta \\ v_\beta & -v_\alpha \end{bmatrix} \begin{bmatrix} u_\alpha \\ u_\beta \end{bmatrix} - \frac{3}{2L} \begin{bmatrix} v_\alpha^2 + v_\beta^2 \\ 0 \end{bmatrix} \quad (3.1)$$

By considering model uncertainties (b), one can rewrite the above model as:

$$\begin{aligned} \dot{x} &= Ax + Bu + F + Db \\ y &= C_x x \end{aligned} \quad (3.2)$$

where

$$A = \begin{bmatrix} -\frac{R}{L} & -\omega \\ \omega & -\frac{R}{L} \end{bmatrix}, \quad B = \frac{3}{2L} \begin{bmatrix} v_\alpha & v_\beta \\ v_\beta & -v_\alpha \end{bmatrix}, \quad C_x = \begin{bmatrix} 1 & 0 \\ 0 & 1 \end{bmatrix} \quad (3.3)$$

and

$$F = -\frac{3}{2L} \begin{bmatrix} v_\alpha^2 + v_\beta^2 \\ 0 \end{bmatrix}, \quad D = \begin{bmatrix} \frac{1}{L} & 0 \\ 0 & \frac{1}{L} \end{bmatrix}, \quad b = \begin{bmatrix} b_P \\ b_Q \end{bmatrix} \quad (3.4)$$

The output to be controlled is the active and reactive powers P and Q .

3.1.2 Feedback Controller

The design of the feedback controller operates on the premise that both the state information x and the disturbance b are accessible. With this assumption in place, effective control over the active and reactive powers becomes achievable through the utilization of feedback controller. Following [80], a feedback controller for grid-side converter can be expressed as

$$u = B^{-1} (Ke + \dot{y}_{ref} - Ax - F - Db) \quad (3.5)$$

where the control gain K is expressed as $K = \text{diag}\{k, k\}$. The variable e represents the tracking error, which is defined as the difference between the reference output y_{ref} and the actual output y , i.e., $e = y_{ref} - y$. The main goal of the feedback controller is to make sure that the controlled variable closely follows its reference pattern in a specific time frame with zero steady-state error, provided that the closed-loop system is stable. Indeed, the stability of the closed-loop system can be investigated by studying the closed-loop error dynamics. This can be achieved by substituting (3.5) into (3.2), resulting in

$$\begin{aligned}
\dot{x} &= Ax + Bu + F + Db \\
&= Ax + BB^{-1}(Ke + \dot{y}_{ref} - Ax - F - Db) + F + Db \\
&= Ke + \dot{y}_{ref}
\end{aligned} \tag{3.6}$$

Recall that $y = x$, therefore, the above equation can be rewritten as

$$\dot{y} = Ke + \dot{y}_{ref} \Rightarrow \dot{e} = -Ke \tag{3.7}$$

where

$$e = y_{ref} - y = \begin{bmatrix} P_{ref} - P \\ Q_{ref} - Q \end{bmatrix}, \tag{3.8}$$

Here, P_{ref} and Q_{ref} are the command values of the active and reactive powers. Since K is a 2×2 diagonal matrix, one can rewrite (3.7) as

$$\dot{e}_p = -ke_p, \quad \dot{e}_q = -ke_q \tag{3.9}$$

where

$$e_p = P_{ref} - P, \quad e_q = Q_{ref} - Q \tag{3.10}$$

The dynamics of the closed-loop system is well defined by a first-order system with a time constant of $1/k$. Hence, the larger k , the faster the system's response. The suggested feedback controller might not be feasible for practical implementation due to the challenge of measuring the disturbance b . To address this limitation, a potential solution involves replacing the real disturbance b with its estimated counterpart \hat{b} under the condition that a suitable estimator capable of generating \hat{b} is available. Consequently, the modified controller can be represented as follows:

$$u = B^{-1}(Ke + \dot{y}_{ref} - Ax - F - D\hat{b}) \tag{3.11}$$

3.1.3 Disturbance Observer

This thesis delves into the utilization of disturbance observers as a pivotal control strategy for enhancing the performance of PMSG-based wind energy generation system for grid-tied applications. The objective is to address the intricate interplay between system dynamics, disturbances, and grid fluctuations, aiming to achieve robust and stable operation under varying conditions. The disturbance observer functions as an inner-loop output-feedback controller, tasked with counteracting external disturbances and bolstering the resilience of the outer-loop baseline controller against uncertainties inherent in the plant. The design of a disturbance observer for the given system described in equation (3.2) becomes a viable avenue for estimating \hat{b} to allow implementing the feedback controller. Following [72], the design of such a disturbance observer requires knowledge of the dynamics of b . In other words, the expression of \dot{b} is needed for the synthesis of an estimator that is capable of producing an accurate estimate of b . Toward this end, it is important to note that when the grid voltages are balanced, the active and reactive powers remain constant. Conversely, in the presence of unbalanced grid voltages, the active and reactive powers can fluctuate at twice the fundamental frequency. Therefore, the disturbance can be represented in the following manner:

$$b_p = \bar{b}_p + \tilde{b}_p, \quad b_q = \bar{b}_q + \tilde{b}_q \quad (3.12)$$

where $\bar{b}_{p,q}$ is a dc component and $\tilde{b}_{p,q}$ is an ac signal that oscillates at twice the fundamental frequency. Specifically, $\tilde{b}_{p,q}$ can be approximated with

$$\tilde{b}_p = b_{PM} \cos(2\omega t + \psi_p), \quad \tilde{b}_q = b_{QM} \cos(2\omega t + \psi_q) \quad (3.13)$$

The time derivative of the disturbance is then given by:

$$\dot{\tilde{b}}_p = -b_{PM} 2\omega \sin(2\omega t + \psi_p), \quad \dot{\tilde{b}}_q = -b_{QM} 2\omega \sin(2\omega t + \psi_q) \quad (3.14)$$

As $\bar{b}_{P,Q}$ is a dc component, it is clear that:

$$\dot{\bar{b}}_P = 0, \quad \dot{\bar{b}}_Q = 0 \quad (3.15)$$

The expression representing the time derivative of $\tilde{b}_{P,Q}$ is a non-linear and time-varying function which is formulated as a function of unknown parameters, namely $b_{PM}, b_{QM}, \psi_P,$ and ψ_Q . Hence, employing such an expression for the construction of a DO is not a straightforward task. In order to streamline the observer design, one can introduce an auxiliary disturbance input $\sigma_{P,Q}$ such that:

$$\sigma_P = b_{PM} \sin(2\omega t + \psi_P), \quad \sigma_Q = b_{QM} \sin(2\omega t + \psi_Q) \quad (3.16)$$

The time derivative of the auxiliary disturbance is given by:

$$\dot{\sigma}_P = b_{PM} 2\omega \cos(2\omega t + \psi_P) = 2\omega \tilde{b}_P, \quad \dot{\sigma}_Q = b_{QM} 2\omega \cos(2\omega t + \psi_Q) = 2\omega \tilde{b}_Q \quad (3.17)$$

Similarly, one can show that.

$$\dot{\tilde{b}}_P = -b_{PM} 2\omega \sin(2\omega t + \psi_P) = -2\omega \sigma_P, \quad \dot{\tilde{b}}_Q = -b_{QM} 2\omega \sin(2\omega t + \psi_Q) = -2\omega \sigma_Q \quad (3.18)$$

From the above equations, it follows that:

$$\begin{aligned} \dot{\bar{b}}_P &= 0 \\ \dot{\bar{b}}_Q &= 0 \\ \dot{\tilde{b}}_P &= -2\omega \sigma_P \\ \dot{\tilde{b}}_Q &= -2\omega \sigma_Q \\ \dot{\sigma}_P &= 2\omega \tilde{b}_P \\ \dot{\sigma}_Q &= 2\omega \tilde{b}_Q \end{aligned} \quad (3.19)$$

Assuming a new state variable z as follows

$$z = [\bar{b}_P \quad \bar{b}_Q \quad \tilde{b}_P \quad \tilde{b}_Q \quad \sigma_P \quad \sigma_Q]^T \quad (3.20)$$

The first-time derivative of z yields

$$\dot{z} = \begin{bmatrix} \dot{\bar{b}}_P \\ \dot{\bar{b}}_Q \\ \dot{\tilde{b}}_P \\ \dot{\tilde{b}}_Q \\ \dot{\sigma}_P \\ \dot{\sigma}_Q \end{bmatrix} = \begin{bmatrix} 0 & 0 & 0 & 0 & 0 & 0 \\ 0 & 0 & 0 & 0 & 0 & 0 \\ 0 & 0 & 0 & 0 & -2\omega & 0 \\ 0 & 0 & 0 & 0 & 0 & -2\omega \\ 0 & 0 & 2\omega & 0 & 0 & 0 \\ 0 & 0 & 0 & 2\omega & 0 & 0 \end{bmatrix} \begin{bmatrix} \bar{b}_P \\ \bar{b}_Q \\ \tilde{b}_P \\ \tilde{b}_Q \\ \sigma_P \\ \sigma_Q \end{bmatrix} = \Omega z \quad (3.21)$$

where Ω is given by:

$$\Omega = \begin{bmatrix} 0 & 0 & 0 & 0 & 0 & 0 \\ 0 & 0 & 0 & 0 & 0 & 0 \\ 0 & 0 & 0 & 0 & -2\omega & 0 \\ 0 & 0 & 0 & 0 & 0 & -2\omega \\ 0 & 0 & 2\omega & 0 & 0 & 0 \\ 0 & 0 & 0 & 2\omega & 0 & 0 \end{bmatrix}, \quad (3.22)$$

The disturbance b can be represented as a mathematical function of z in the following manner:

$$b = \begin{bmatrix} b_P \\ b_Q \end{bmatrix} = \begin{bmatrix} \bar{b}_P + \tilde{b}_P \\ \bar{b}_Q + \tilde{b}_Q \end{bmatrix} = \begin{bmatrix} 1 & 0 & 1 & 0 & 0 & 0 \\ 0 & 1 & 0 & 1 & 0 & 0 \end{bmatrix} \begin{bmatrix} \bar{b}_P \\ \bar{b}_Q \\ \tilde{b}_P \\ \tilde{b}_Q \\ \sigma_P \\ \sigma_Q \end{bmatrix} = Hz \quad (3.23)$$

where

$$H = \begin{bmatrix} 1 & 0 & 1 & 0 & 0 & 0 \\ 0 & 1 & 0 & 1 & 0 & 0 \end{bmatrix} \quad (3.24)$$

In summary, the disturbance b is governed by the differential equation:

$$\dot{z} = \Omega z, \quad b = Hz \quad (3.25)$$

Substituting $b = Hz$ into (3.1) yields

$$\dot{x} = Ax + Bu + F + Db = Ax + Bu + F + DHz \quad (3.26)$$

By taking into account the \dot{x} -equation and the \dot{z} -equation, one has the choice to utilize the Luenberger observer for estimating the disturbance \hat{b} through the estimation of the state variable \hat{z} . As in [81], a Luenberger observer can be formulated as

$$\begin{aligned} \dot{\hat{x}} &= Ax + Bu + F + DH\hat{z} + G_{1p}(y - \hat{y}) \\ \dot{\hat{z}} &= \Omega\hat{z} + G_{2p}(y - \hat{y}) \\ \hat{b} &= H\hat{z} \end{aligned} \quad (3.27)$$

The observer gains G_{1p} and G_{2p} can be selected based on the stability condition of the disturbance observer. Toward this end, first note that the output y and its estimate \hat{y} are given by:

$$y = x = \begin{bmatrix} P \\ Q \end{bmatrix}, \quad \hat{y} = \hat{x} = \begin{bmatrix} \hat{P} \\ \hat{Q} \end{bmatrix} \quad (3.28)$$

The stability of the observer can be investigated by analyzing the dynamics of the estimation error e_{obs} , given by

$$e_{obs} = \begin{bmatrix} \hat{x} - x \\ \hat{z} - z \end{bmatrix} \quad (3.29)$$

The estimation error is governed by the following differential equation:

$$\begin{aligned}
\dot{e}_{obs} &= \begin{bmatrix} \dot{\hat{x}} \\ \dot{\hat{z}} \end{bmatrix} - \begin{bmatrix} \dot{x} \\ \dot{z} \end{bmatrix} = \begin{bmatrix} Ax + Bu + F + DH\hat{z} \\ \Omega\hat{z} \end{bmatrix} + \begin{bmatrix} G_{1p} \\ G_{2p} \end{bmatrix} (y - \hat{y}) - \begin{bmatrix} Ax + Bu + F + DHz \\ \Omega z \end{bmatrix} \\
&= \begin{bmatrix} DH\hat{z} - DHz \\ \Omega\hat{z} - \Omega z \end{bmatrix} + \begin{bmatrix} G_{1p} \\ G_{2p} \end{bmatrix} (Cx - C\hat{x}) = \begin{bmatrix} DH(\hat{z} - z) \\ \Omega(\hat{z} - z) \end{bmatrix} - \begin{bmatrix} G_{1p} \\ G_{2p} \end{bmatrix} (\hat{x} - x) \\
&= \begin{bmatrix} -G_{1p} & DH \\ -G_{2p} & \Omega \end{bmatrix} \begin{bmatrix} x - \hat{x} \\ \hat{z} - z \end{bmatrix}
\end{aligned} \tag{3.30}$$

which can be rewritten as

$$\dot{e}_{obs} = \Omega_{cl} e_{obs} \tag{3.31}$$

where

$$\Omega_{cl} = \begin{bmatrix} -G_{1p} & DH \\ -G_{2p} & \Omega \end{bmatrix} \tag{3.32}$$

Hence, the observer's stability is ensured through an appropriate choice of the observer gains G_{1p} and G_{2p} , in a manner that makes the observer matrix Ω_{cl} Hurwitz. This implies that the real parts of the eigenvalues of Ω_{cl} are negative. A straightforward and pragmatic approach involves initially assigning the desired locations in the left-half of the complex plane for the eigenvalues of Ω_{cl} . Subsequently, the observer gains can be determined to align the eigenvalues of Ω_{cl} with the desired locations. The MATLAB function “*place*” can be used to find the observer gain G_p as

$$G_p^T = place \left(\begin{bmatrix} 0_{2 \times 2} & DH \\ 0_{6 \times 2} & \Omega \end{bmatrix}^T, \begin{bmatrix} I_{2 \times 2} \\ 0_{6 \times 2} \end{bmatrix}, S_p \right) \tag{3.33}$$

where S_p includes the eight desired observer eigenvalues $\lambda_{\{1:4\}}$; it can be selected as

$$S_p = [\lambda_1; \lambda_1; \lambda_2; \lambda_2; \lambda_3; \lambda_3; \lambda_4; \lambda_4] \tag{3.34}$$

The desired observer eigenvalues $\lambda_{\{1:4\}}$ can be selected as

$$\lambda_{1,2} = \zeta\omega_{n1} \pm j\omega_{n1}\sqrt{1-\zeta^2}, \quad \lambda_{3,4} = \zeta\omega_{n2} \pm j\omega_{n2}\sqrt{1-\zeta^2} \quad (3.35)$$

where ζ is the damping factor, while ω_{n1} and ω_{n2} are the natural pulsations that should be chosen as large as feasible to ensure rapid convergence of the disturbance observer. Typically, the value of ζ can be set to 0.707. Had G_p been calculated, G_{1p} and G_{2p} could have been calculated as

$$G_p = \begin{bmatrix} G_{1p} \\ G_{2p} \end{bmatrix}, \quad \text{with} \quad G_{1p} \in \mathbb{R}^{2 \times 2} \quad \text{and} \quad G_{2p} \in \mathbb{R}^{6 \times 2} \quad (3.36)$$

During real-time implementation, there may be discrepancies between the control input u , which is provided by the controller, and the actual control input, particularly during transitory times. This difference between the actual control input and that generated by the controller may occur only during transients due to the possible saturation of the control input. This saturation of control input during transients should be considered in the observer design through the use of a simple saturation function. Thus, the developed Luenberger observer can be modified by replacing the control input u by $\text{sat}(u)$ in (3.27), yielding

$$\begin{aligned} \dot{\hat{x}} &= Ax + B\text{sat}(u) + F + DH\hat{z} + G_{1p}(y - C\hat{x}) \\ \dot{\hat{z}} &= \Omega\hat{z} + G_{2p}(y - C\hat{x}) \end{aligned} \quad (3.37)$$

where $\hat{x}(0) = 0$ and $\hat{z}(0) = 0$. The above disturbance observer can be made even more straightforward by replacing u by its expression given by (3.11). To this end, first note that the $\dot{\hat{x}}$ -equation of the above disturbance observer can be rewritten as

$$\begin{aligned} \dot{\hat{x}} &= Ax + B\text{sat}(u) + F + DH\hat{z} + G_{1p}(y - C\hat{x}) + B(u - u) \\ &= Ax - B(u - \text{sat}(u)) + Bu + F + DH\hat{z} + G_{1p}(y - C\hat{x}) \\ &= Ax + Bu + F + DH\hat{z} + G_{1p}(y - C\hat{x}) - B\Delta u \end{aligned} \quad (3.38)$$

where

$$\Delta u = u - sat(u) \quad (3.39)$$

The simplification process can be achieved by replacing u by its expression given by (3.3).

That is,

$$\begin{aligned} \dot{\hat{x}} &= Ax + BB^{-1} \left(Ke + \dot{y}_{ref} - Ax - F - D\hat{b} \right) + F + DH\hat{z} + G_{1P} (y - C\hat{x}) - B\Delta u \\ &= Ax + \left(Ke + \dot{y}_{ref} - Ax - F - DH\hat{z} \right) + F + DH\hat{z} + G_{1P} (y - C\hat{x}) - B\Delta u \\ &= \left(Ke + \dot{y}_{ref} \right) + G_{1P} (y - C\hat{x}) - B\Delta u \end{aligned} \quad (3.40)$$

Therefore, the Luenberger observer reduces to

$$\begin{aligned} \dot{\hat{x}} &= \left(Ke + \dot{y}_{ref} \right) + G_{1P} (y - C\hat{x}) - B\Delta u \\ \dot{\hat{z}} &= \Omega\hat{z} + G_{2P} (y - C\hat{x}) \end{aligned} \quad (3.41)$$

The implementation of the above observer (3.41) requires the information about \dot{y}_{ref} which is not recommended as the reference can be a function of measurements. In other words, the calculation of \dot{y}_{ref} can result in a magnification of the measurement noises if y_{ref} is a function of measurements such as dc-link voltage. To simplify the above observer, one can consider the following change of variable as

$$\xi = \hat{x} - y_{ref} \quad (3.42)$$

Thus, the time derivative of ξ can be calculated as

$$\begin{aligned} \dot{\xi} &= \dot{\hat{x}} - \dot{y}_{ref} = \left(Ke + \dot{y}_{ref} \right) + G_{1P} (x - \hat{x}) - B\Delta u - \dot{y}_{ref} \\ &= Ke + G_{1P} (x - \hat{x}) - B\Delta u \\ &= Ke + G_{1P} \left(x - (\xi + y_{ref}) \right) - B\Delta u \\ &= Ke - G_{1P}\xi + G_{1P} (y - y_{ref}) - B\Delta u \\ &= Ke - G_{1P}\xi - G_{1P}e - B\Delta u \\ &= (K - G_{1P})e - G_{1P}\xi - B\Delta u \end{aligned} \quad (3.43)$$

Proceeding in the same manner, $\dot{\hat{z}}$ -equation can be rewritten as

$$\begin{aligned}
\dot{\hat{z}} &= \Omega\hat{z} + G_{2p}(x - \hat{x}) \\
&= \Omega\hat{z} + G_{2p}\left(x - (\xi + y_{ref})\right) \\
&= \Omega\hat{z} - G_{2p}\xi + G_{2p}(x - y_{ref}) \\
&= \Omega\hat{z} - G_{2p}\xi - G_{2p}e_p
\end{aligned} \tag{3.44}$$

Finally, the simplified Luenberger observer can be implemented without the need for \dot{y}_{ref} as

$$\begin{aligned}
\dot{\xi} &= -G_{1p}\xi + (K_p - G_{1p})e_p - B\Delta u \\
\dot{\hat{z}} &= -G_{2p}\xi + \Omega\hat{z} - G_{2p}e_p \\
b &= H\hat{z}
\end{aligned} \tag{3.45}$$

where

$$\begin{aligned}
\xi(0) &= y(0) - y_{ref}(0) = -e(0) \\
\hat{z}(0) &= 0
\end{aligned} \tag{3.46}$$

Recall that the practical implementation of the feedback controller u , given by (3.11) requires the measurement of \dot{y}_{ref} , which is not possible for the system under study. This difficulty in measuring the variable \dot{y}_{ref} can be reduced by calculating \dot{y}_{ref} directly from the information about y_{ref} . It is crucial to acknowledge that y_{ref} itself may be calculated directly from the measurement of dc-link voltage and the grid voltages. Hence, the inclusion of \dot{y}_{ref} in the feedback controller may result in a deterioration of the steady-state performance as a consequence of potential amplification of the effect of measurement noises. One possible approach to address this concern for real-time implementation is to disregard the term \dot{y}_{ref} from the expression of the control input u . This is because the disturbance observer has the capability to effectively counteract the impact of any disturbances that exhibit oscillations at a frequency of 2ω , including \dot{y}_{ref} . Hence, the feedback controller (3.11) can be implemented as

$$u = B^{-1}(Ke - Ax - F - D\hat{b}) \tag{3.47}$$

3.2 DC-Link Control under Balanced Grid Voltages

3.2.1 Feedback Controller

This section is concerned with the design of a controller for the dc-link voltage. As pointed out above, during balanced grid voltages, the dc-link voltage is regulated using the grid-side converter, where a cascade control scheme, involving two loops, is employed to implement the dc-link voltage controller. With this particular control scheme, an inner power loop is designed to adjust the active and reactive powers injected into the grid, while an outer voltage loop is synthesized to achieve asymptotic regulation of the dc-link voltage. In such a control scheme, the outer voltage loop provides the command active power P_{ref} for the grid-tied inverter power controller. The command reactive power Q_{ref} for the grid-tied inverter power controller can be set equal to zero to ensure unity power factor operation. Recall that the differential equation governing the dynamics of the dc-link voltage is given by:

$$\frac{dv_{dc}}{dt} = \frac{i_{dc}}{C} - \frac{P}{Cv_{dc}} \quad (3.48)$$

where P is the active power delivered to the grid. Now, by treating P as the control input, equation (3.48) can be represented using the state space model as

$$\dot{x}_v = A_{vb}x_v + B_{vb}(x_v)P + D_{vb}b_{vb} \quad (3.49)$$

where

$$x_v = v_{dc}, \quad A_{vb} = 0, \quad B_{vb}(x_v) = -\frac{1}{Cv_{dc}}, \quad D_{vb} = \frac{1}{C} \quad (3.50)$$

The current i_{dc} is assumed to be an unknown disturbance for the control design. Thus, the disturbance $b_{vb} = i_{dc} + b_{vb}$ represents the current i_{dc} and all unknown disturbances that are not considered in the modeling. The dc-link voltage controller can be designed by proceeding as in the case of the power controller. The dc-link voltage has a constant steady-state value, so it can be assumed that:

$$\dot{\hat{b}}_{vb} = 0 \quad (3.51)$$

Therefore, by proceeding as before, the reference P_{ref} for the active power can be generated by the outer loop as follows:

$$P_{ref} = -v_{dc} C \left(k_v e_v + \frac{dv_{dcref}}{dt} - \frac{b_{vb}}{C} \right) \quad (3.52)$$

where $e_v = v_{dcref} - v_{dc}$ is the tracking error, and k_v is the control gain. By assuming knowledge of b_{vb} and choosing $k_v > 0$, the developed feedback controller can asymptotically stabilize the dc-link voltage. More precisely, one can show that the transient response of dc-link voltage to a step change in the set-point can exhibit a first-order system with a time constant of $1/k_v$. Therefore, it is clear that increasing k_v causes the tracking error to vanish faster in response to a sudden change in the command value. As pointed out above, it is not trivial to measure the disturbance b_{vb} because of model uncertainties. To tackle such a problem, the above controller can be implemented as

$$P_{ref} = -v_{dc} C \left(k_v e_v + \frac{dv_{dcref}}{dt} - \frac{\hat{b}_{vb}}{C} \right) \quad (3.53)$$

where \hat{b}_{vb} is the estimate of the actual b_{vb} .

3.2.2 Disturbance Observer

The implementation of (3.53) creates the need for a disturbance observer to estimate \hat{b}_{vb} . This can be achieved through the use of the so-called reduced-order disturbance observer; it can be formulated as [72]

$$\begin{aligned} \dot{\hat{b}}_{vb} &= G_v \left(\dot{x}_v - A_{vb} x_v - B_{vb}(x_v) P_{ref} - D_{vb} \hat{b}_{vb} \right) \\ &= -G_v \frac{1}{C} \hat{b}_{vb} + G_v \left(\frac{dv_{dc}}{dt} + \frac{P_{ref}}{v_{dc} C} \right) \end{aligned} \quad (3.54)$$

The observer gain G_v should be selected to satisfy the stability condition of the disturbance observer. In particular, the observer gain G_v can be selected considering the stability of the estimation error $e_{obsv} = \hat{b}_{vb} - b_{vb}$. By assuming $\dot{b}_{vb} = 0$ and proceeding as in the previous section, it can easily be verified that the estimation error satisfies.

$$\begin{aligned}
\dot{e}_{obsv} &= -G_v \frac{1}{C} \hat{b}_{vb} + G_v \left(\frac{dv_{dc}}{dt} + \frac{P_{ref}}{v_{dc}C} \right) \\
&= -G_v \frac{\hat{b}_{vb}}{C} + G_v \frac{b_{vb}}{C} \\
&= -\frac{G_v}{C} e_{obsv}
\end{aligned} \tag{3.55}$$

The above differential equation indicates that by choosing $G_v > 0$, the estimation error is asymptotically stable for all disturbance b_{vb} satisfying $\dot{b}_{vb} = 0$. More importantly, one can conclude that the response of the estimate \hat{b}_{vb} to a step change in b_{vb} can exhibit a first-order system with a time constant of $1/G_v$. Therefore, it is clear that a larger value of G_v can cause the estimation error to decay faster toward zero. However, in real-time implementation, the command power P_{ref} provided by the controller might deviate from the true control input during transients because of the saturation effect. This should be reflected in the expression of the disturbance observer by introducing a saturation mechanism to restrict P_{ref} during transient periods. In other words, it is required to replace P_{ref} by $sat(P_{ref})$ in the expression of the disturbance observer; that is:

$$\dot{\hat{b}}_{vb} = -G_v \frac{1}{C} \hat{b}_{vb} + G_v \left(\frac{dv_{dc}}{dt} + \frac{1}{v_{dc}C} sat(P_{ref}) \right) \tag{3.56}$$

which leads to:

$$\begin{aligned}
\dot{\hat{b}}_{vb} &= -G_v \frac{1}{C} \hat{b}_{vb} + G_v \left(\frac{dv_{dc}}{dt} + \frac{1}{v_{dc}C} \text{sat}(P_{ref}) \right) \\
&= -G_v \frac{1}{C} \hat{b}_{vb} + G_v \left(\frac{dv_{dc}}{dt} + \frac{1}{v_{dc}C} \text{sat}(P_{ref}) + \frac{1}{v_{dc}C} P_{ref} - \frac{1}{v_{dc}C} P_{ref} \right) \\
&= -G_v \frac{1}{C} \hat{b}_{vb} + G_v \left(\frac{dv_{dc}}{dt} + \frac{1}{v_{dc}C} P_{ref} - \frac{1}{v_{dc}C} \Delta P_{ref} \right)
\end{aligned} \tag{3.57}$$

where

$$\Delta P_{ref} = P_{ref} - \text{sat}(P_{ref}) \tag{3.58}$$

The disturbance observer can be further simplified by replacing the command power P_{ref} in (3.57) by its expression (3.53), yielding

$$\begin{aligned}
\dot{\hat{b}}_{vb} &= -G_v \frac{1}{C} \hat{b}_{vb} + G_v \left(\frac{dv_{dc}}{dt} - \left(k_v e_v + \frac{dv_{dcref}}{dt} - \frac{\hat{b}_{vb}}{C} \right) - \frac{1}{v_{dc}C} \Delta P_{ref} \right) \\
&= -G_v (k_v e_v + \dot{e}_v) - \frac{G_v}{v_{dc}C} \Delta P_{ref}
\end{aligned} \tag{3.59}$$

Note that the information about \dot{e}_{vb} is needed to implement the above disturbance observer. The absence of measurement of \dot{e}_{vb} creates the need for calculating \dot{e}_{vb} , which can raise a concern about measurement noise amplification due to the direct relationship between e_{vb} and the measurement of dc-link voltage. To overcome such a concern, let \hat{z}_{vb} be a new disturbance input such that:

$$\hat{z}_{vb} = \hat{b}_{vb} + G_v e_v \tag{3.60}$$

Therefore, one can estimate \hat{b}_{vb} by substituting (3.59) into (3.60)

$$\begin{aligned}
\dot{\hat{z}}_{vb} &= \dot{\hat{b}}_{vb} + G_v \dot{e}_v = -G_v k_v e_v - \frac{G_v}{v_{dc}C} \Delta P_{ref} \\
\hat{b}_{vb} &= \hat{z}_{vb} - G_v e_v
\end{aligned} \tag{3.61}$$

with

$$\hat{z}_{vb}(0) = \hat{b}_{vb}(0) + G_v e_v(0) \quad (3.62)$$

3.3 Current Control of the Machine-Side Converter

Under balanced grid voltages, the machine-side converter is controlled to regulate the current flowing through the stator windings of the PMSG, with the aim of extracting the maximum power from the wind. In this chapter, the current controller is designed in the $\alpha\beta$ reference frame, which does not require dq transformation.

3.3.1 Perturbed Model and Feedback Controller

By assuming a non-salient pole machine, the model of the PMSG in the stationary $\alpha\beta$ reference frame is given by:

$$\dot{x}_m = A_m x_m + B_m u_m + F_m \quad (3.63)$$

where

$$\begin{bmatrix} di_\alpha \\ di_\beta \end{bmatrix} = \begin{bmatrix} \frac{-R_s}{L_{cs}} & 0 \\ 0 & \frac{-R_s}{L_{cs}} \end{bmatrix} \begin{bmatrix} i_\alpha \\ i_\beta \end{bmatrix} + \begin{bmatrix} \frac{1}{L_{cs}} & 0 \\ 0 & \frac{1}{L_{cs}} \end{bmatrix} \begin{bmatrix} u_\alpha \\ u_\beta \end{bmatrix} + \frac{\omega_e}{L_{cs}} \psi_r \begin{bmatrix} -\sin(\theta_e) \\ \cos(\theta_e) \end{bmatrix} \quad (3.64)$$

and

$$u_m = \begin{bmatrix} u_{\alpha s} \\ u_{\beta s} \end{bmatrix}, \quad x_m = \begin{bmatrix} i_{\alpha s} \\ i_{\beta s} \end{bmatrix} \quad (3.65)$$

Recall that for a non-salient pole machine, the inductance L_{cs} is given by:

$$L_{cs} = L_{ds} = L_{qs} \quad (3.66)$$

The above model can be rewritten as

$$\dot{x}_m = A_m x_m + B_m u_m + D_m b_m \quad (3.67)$$

where

$$D_m = \begin{bmatrix} \frac{1}{L_{cs}} & 0 \\ 0 & \frac{1}{L_{cs}} \end{bmatrix}, \quad b_m = \begin{bmatrix} b_{s1} \\ b_{s2} \end{bmatrix} = L_{cs} F_m = \begin{bmatrix} -\omega_e \psi_r \sin(\theta_e) \\ \omega_e \psi_r \cos(\theta_e) \end{bmatrix} \quad (3.68)$$

The above model is valid only if the machine has a non-salient pole and the system's model is accurate; it does not contain uncertain parameters. However, considering the saliency in the modeling can result in a complex model due to nonlinear coupling among the stator winding currents, the rotor speed, and the rotor angle. In this thesis, the above model is adopted for both salient and non-salient pole machine; only the disturbance b_m is modified to account for the effect of saliency and modelling errors. In the stationary reference frame, the stator winding currents exhibit sinusoidal waveforms that oscillate at a known frequency (ω_e) which can be directly calculated from the rotor speed measurement. This suggests that, under steady-state conditions, the disturbance b_m approaches a sinusoidal waveform with the oscillation frequency equal to the frequency of the stator winding currents. With this suggestion, the disturbance b_m can be approximated by

$$b_m = \begin{bmatrix} b_{s1} \\ b_{s2} \end{bmatrix} = \begin{bmatrix} b_{s1M} \cos(\theta_e + \psi_{s1}) \\ b_{s2M} \cos(\theta_e + \psi_{s2}) \end{bmatrix} = \begin{bmatrix} b_{s1M} \cos(\omega_e t + \psi_{s1}) \\ b_{s2M} \cos(\omega_e t + \psi_{s2}) \end{bmatrix} \quad (3.69)$$

where the parameters b_{s1M} , b_{s2M} , ψ_{s1} , and ψ_{s2} , are not known. In addition, to ease the control design for a salient pole machine, one can assume:

$$L_{cs} = L_s = \frac{L_{ds} + L_{qs}}{2} \quad (3.70)$$

In a summary, the perturbed model (3.67) of PMSG can be used to design a controller for both salient and non-salient pole machine, where the unknown disturbance b_m is introduced to represent the effect of model uncertainties and the saliency of the machine. The

perturbed model indicates that the dynamics of $i_{\alpha s}$ and $i_{\beta s}$ are independent; therefore, a feedback controller can be designed by assuming only the mathematical model of the single-phase system. That is, by omitting the subscripts α and β , the model of PMSG for the control design in the $\alpha\beta$ reference frame can be simplified as

$$\frac{dy}{dt} = -\frac{R_s}{L_s} y + \frac{u_s}{L_s} + \frac{b_s}{L_s} \quad (3.71)$$

where

$$y = i_{\alpha s} \text{ or } i_{\beta s} \quad u_s = u_{\alpha s} \text{ or } u_{\beta s}, \quad b_s = b_{s1} \text{ or } b_{s2} \quad (3.72)$$

Similarly, one can omit the subscripts 1 and 2 in the expression of b_s to write:

$$b_s = b_{sM} \cos(\theta_e + \psi_s) \quad (3.73)$$

According to [82] a feedback controller can take the following form

$$u_s = L_s \left(\frac{R_s}{L_s} y - \frac{b_s}{L_s} + \vartheta \right) \quad (3.74)$$

The symbol ϑ represents an auxiliary control input. Now, by inserting equation (3.74) into equation (3.71), one can obtain

$$\frac{dy}{dt} = \vartheta \quad (3.75)$$

According to equation (3.75), it may be inferred that ϑ can be constructed utilizing the tools of linear control theory. In this context, the symbol ϑ is chosen in such a way that the tracking error $e_s = y_{ref} - y$ is governed by:

$$\dot{e}_s = -k_s e_s, \quad k_s > 0 \quad (3.76)$$

where y_{ref} is the current reference, and the variable k_s represents the control gain. It is clear that the closed-loop system is asymptotically stable provided that k_s is positive. In order to get a quick transient reaction and a fast disturbance rejection, it is recommended to select the control gain k_s as large as possible. The auxiliary control input ϑ can be obtained by substituting equation (3.75) into equation (3.76), resulting in

$$\vartheta = \dot{y}_{ref} + k_s e_s \quad (3.77)$$

Now, substituting (3.77) and (3.71) into (3.74) gives

$$u_s = L_s \left(k_s e_s + \dot{y}_{ref} + \frac{R_s}{L_s} y - \frac{b_s}{L_s} \right) \quad (3.78)$$

In real applications, the disturbance input b_s is often unknown, which gives rise to problems regarding the practical implementation of the output feedback controller. As before, such a problem can be tackled by replacing the actual disturbance b_s by its estimate \hat{b}_s in the feedback controller, yielding:

$$u_s = L_s \left(k_s e_s + \dot{y}_{ref} + \frac{R_s}{L_s} y - \frac{\hat{b}_s}{L_s} \right) \quad (3.79)$$

3.3.2 Disturbance Observer

The development a disturbance observer capable of estimating b_m requires the knowledge of the dynamics of b_s , particularly in the steady-state. From (3.73), it follows that:

$$\dot{b}_s = -b_{sM} \omega_e \sin(\omega_e t + \psi_s) \quad (3.80)$$

Let σ_s be an auxiliary disturbance input, where

$$\sigma_s = b_{sM} \sin(\omega_e t + \psi_s) \quad (3.81)$$

which implies

$$\dot{\sigma}_s = b_{sM} \omega_e \cos(\omega_e t + \psi_s) \quad (3.82)$$

Assuming a new state variable z_s to represent the disturbances and their first-time derivative; that is:

$$z_s = \begin{bmatrix} b_s \\ \sigma_s \end{bmatrix} \quad (3.83)$$

The differential equation presented thereafter governs the dynamics of the disturbance b_s

$$\begin{aligned} \dot{z}_s &= \Omega_s z_s \\ b_s &= [1 \quad 0] z_s \end{aligned} \quad (3.84)$$

where

$$\Omega_s = \begin{bmatrix} 0 & -\omega_e \\ \omega_e & 0 \end{bmatrix} \quad (3.85)$$

Following [81] the disturbance input b_s can be estimated using the following reduced-order disturbance observer

$$\begin{aligned} \dot{\hat{b}}_s &= -\omega_e \hat{\sigma}_s - \frac{l_1}{L_s} \hat{b}_s + l_1 \left(\frac{dy}{dt} + \frac{R_s}{L_s} y - \frac{1}{L_s} u_s \right) \\ \dot{\hat{\sigma}}_s &= \omega_e \hat{b}_s - \frac{l_2}{L_s} \hat{b}_s + l_2 \left(\frac{dy}{dt} + \frac{R_s}{L_s} y - \frac{1}{L_s} u_s \right) \end{aligned} \quad (3.86)$$

The observer gains l_1 and l_2 are chosen based on the stability criteria of the disturbance observer. In a compact form, the observer (3.86) can be expressed as

$$\dot{\hat{z}}_s = \Omega_s \hat{z}_s - M \begin{bmatrix} \frac{1}{L_s} & 0 \end{bmatrix} \hat{z}_s + M \left(\frac{dy}{dt} + \frac{R_s}{L_s} y - \frac{1}{L_s} u_s \right) \quad (3.87)$$

where

$$M = \begin{bmatrix} l_1 \\ l_2 \end{bmatrix} \quad (3.88)$$

The stability condition of the disturbance observer can be investigated by studying the dynamics of the estimation error e_{obs} , with

$$e_{obs} = \hat{z}_s - z \quad (3.89)$$

The dynamics of the estimation error is then governed by:

$$\begin{aligned} \dot{e}_{obs} &= \Omega_s \hat{z}_s - M \begin{bmatrix} 1 & 0 \\ L_s & 0 \end{bmatrix} \hat{z}_s + M \left(\frac{dy}{dt} + \frac{R_s}{L_s} y - \frac{1}{L_s} u_s \right) - \Omega_s z_s \\ &= \Omega_s \hat{z}_s - M \begin{bmatrix} 1 & 0 \\ L_s & 0 \end{bmatrix} \hat{z}_s + M \frac{b_s}{L_s} - \Omega_s z_s \\ &= \Omega_s \hat{z}_s - M \begin{bmatrix} 1 & 0 \\ L_s & 0 \end{bmatrix} \hat{z}_s + M \begin{bmatrix} 1 & 0 \\ L_s & 0 \end{bmatrix} z_s - \Omega_s z_s \\ &= \left(\Omega_s - M \begin{bmatrix} 1 & 0 \\ L_s & 0 \end{bmatrix} \right) (\hat{z}_s - z_s) \end{aligned} \quad (3.90)$$

Thus, one can write:

$$\dot{e}_{obs} = \Omega_{cls} e_{obs} \quad (3.91)$$

where

$$\Omega_{cls} = \Omega_s - M \begin{bmatrix} 1 & 0 \\ L_s & 0 \end{bmatrix} = \begin{bmatrix} 0 & -\omega_e \\ \omega_e & 0 \end{bmatrix} - \begin{bmatrix} \frac{l_1}{L_s} & 0 \\ \frac{l_2}{L_s} & 0 \end{bmatrix} = \begin{bmatrix} -\frac{l_1}{L_s} & -\omega_e \\ \omega_e - \frac{l_2}{L_s} & 0 \end{bmatrix} \quad (3.92)$$

Equation (3.91) demonstrates that the stability of the disturbance observer can be achieved by appropriately selecting the gains l_1 and l_2 , so that the matrix Ω_{cls} is Hurwitz. A simple design approach is to select the observer gains to correspond to desired eigenvalues in the open left-half plane. In such a case, the desired eigenvalues $\lambda_{1,2}$ can be selected as

$$\lambda_{1,2} = -\zeta_s \omega_{ns} \pm j\omega_{ns} \sqrt{1 - \zeta_s^2} \quad (3.93)$$

where, ζ_s and ω_{ns} represent the damping ratio and natural pulsation, respectively. More precisely, it is recommended that the value of ζ_s should be within a certain range [0 1]. Setting $\zeta_s = 0.707$ is a typical choice for a second order system. The selection of the natural pulsation ω_{ns} should be made as large as possible in order to obtain fast convergence of the disturbance observer. Once ζ_s and ω_{ns} are fixed, it can easily be verified that the observer gains l_1 and l_2 satisfy

$$l_1 = 2L_s \zeta_s \omega_{ns} \quad l_2 = -L_s \left(\frac{\omega_{ns}^2}{\omega_{ns}} - \omega_{ns} \right) \quad (3.94)$$

During transients, it is possible for the control input u_s , which is provided by the controller, to deviate from the actual control. To provide more clarification, during transients, the control input generated by the controller may exceed its allowable maximum value, which necessitates the limitation of the control input u_s to its allowable maximum value. Limitation of the control input during transients can be achieved through the use of a simple saturation block. This mandates the modification of the disturbance observer to reflect the eventual saturation of the control input during transients. This can be achieved by modifying the disturbance observer as

$$\dot{\hat{z}}_s = \Omega_s \hat{z}_s - M \begin{bmatrix} 1 & 0 \\ L_s & 0 \end{bmatrix} \hat{z}_s + M \left(\frac{dy}{dt} + \frac{R_s}{L_s} y - \frac{1}{L_s} \text{sat}(u_s) \right) \quad (3.95)$$

The above disturbance observer can be further simplified by inserting the expression of the control input u_s into the above disturbance observer expression, resulting in

$$\dot{\hat{z}}_s = \Omega_s \hat{z}_s - M \begin{bmatrix} 1 & 0 \\ L_s & 0 \end{bmatrix} \hat{z}_s + M \left(\frac{dy}{dt} + \frac{R_s}{L_s} y - \frac{1}{L_s} u_s + \Delta u_s \right) \quad (3.96)$$

where

$$\Delta u_s = u_s - \text{sat}(u_s) \quad (3.97)$$

Substituting the control input u_s in (3.79) into (3.96), yields

$$\dot{\hat{z}}_s = \Omega_s \hat{z}_s - M \left(\dot{e}_s + k_s e_s - \frac{1}{L_s} \Delta u_s \right) \quad (3.98)$$

The need for calculating \dot{e}_s can create difficulties in implementing the above disturbance observer due to the potential amplification of the effect of measurement noise. These difficulties can be reduced by introducing a new variable $\hat{\xi}_s$ satisfying:

$$\hat{\xi}_s = \hat{z}_s + M e_s \quad (3.99)$$

Substituting (3.98) into (3.99) results in a new form of disturbance observer that is more suitable for real-time implementation as it does not require the time derivative e_s . That is:

$$\begin{aligned} \dot{\hat{\xi}}_s &= \Omega_s \hat{z}_s - M \left(k_s e_s - \frac{1}{L_s} \Delta u_s \right) \\ \hat{z}_s &= \hat{\xi}_s - M e_s \\ \hat{b}_s &= [0 \quad 1] \hat{z} \end{aligned} \quad (3.100)$$

Equation (3.79) indicates that the calculation of the control input u_s requires the information about the time derivative of y_{ref} . This requirement can raise a concern about possible magnification of the measurement noises, particularly, when y_{ref} is an output of another control loop. This concern can be addressed by neglecting y_{ref} in real-time implementation as the disturbance observer can cancel the effect of all disturbances oscillating at ω_e . Hence the control input can be implemented as

$$u_s = L_s \left(k_s e_s + \dot{y}_{ref} + \frac{R_s}{L_s} y - \frac{\hat{b}_s}{L_s} \right) \quad (3.101)$$

3.3.3 Current Reference for Maximum Power Point Tracking (MPPT)

It is important to emphasize that, for a given wind speed v_w , a maximum power can be extracted from the wind if the rotor of the wind turbine rotates at an optimal speed, denoted here by ω_{r-opt} . Indeed, from Figure 8, it can be concluded that there exists a specific rotor speed that consistently yields the highest power output for every wind speed. Now, if the current controller is able to accurately track the optimal speed for every wind speed, the wind turbine can capture the maximum available power from the wind at any speed within a permissible range. According to [83], the optimal rotor speed ω_{r-opt} is a function of the wind speed v_w and the characteristic of the machine; that is

$$\omega_{r-opt} = \frac{n\lambda_{opt}}{R_b} v_w \quad (3.102)$$

where n and R_b are the gear ratio and the rotor plane radius (m), respectively. The coefficient λ_{opt} represents the optimal value of the tip speed ratio λ of the blade; it corresponds to the maximum value C_{pmax} of the power coefficient curve C_p of the wind turbine [83]. For a given wind speed v_w , the amount of the power captured by the wind turbine is given by (2.29) as

$$P_r = 0.5\rho A v_w^3 C_p(\lambda, \beta) = 0.5\rho\pi R_b^2 v_w^3 C_p(\lambda, \beta) \quad (3.103)$$

As pointed out above, the wind turbine can extract the maximum power from the wind when the tip speed ratio λ is equal to its optimal value λ_{opt} corresponding to $C_p = C_{pmax}$. This means that the expression of the maximum power takes the form of:

$$P_{r-opt} = 0.5\rho\pi R_b^2 v_w^3 C_{pmax}(\lambda, \beta) \quad (3.104)$$

which can be rewritten as a function of the optimal rotor speed ω_{r-opt} as

$$P_{r-opt} = 0.5\rho\pi R_b^2 C_{pmax}(\lambda, \beta) \left(\frac{\omega_{r-opt} R_b}{n\lambda_{opt}} \right)^3 \quad (3.105)$$

Therefore, the optimal torque that corresponds to the maximum power can be derived as

$$T_{r-opt} = \frac{P_{r-opt}}{\omega_{r-opt}} = 0.5 \rho \pi R_b^2 C_{pmax} (\lambda, \beta) \left(\frac{R_b}{n \lambda_{opt}} \right)^3 \omega_{r-opt}^2 \quad (3.106)$$

which can be rewritten as

$$T_{r-opt} = K_{opt} \omega_{r-opt}^2 \quad (3.107)$$

where

$$K_{opt} = 0.5 \rho \pi R_b^2 C_{pmax} (\lambda, \beta) \left(\frac{R_b}{n \lambda_{opt}} \right)^3 \quad (3.108)$$

Had the expression of the optimal torque T_{r-opt} been found, the command values for the current controller could have been calculated using the direct relationship between the machine torque and the stator windings currents. In the stationary reference frame, the machine torque is expressed as a non-linear and time-varying function of both α -axis current and β -axis current, which makes it difficult to express the current references $i_{\alpha sref}$ and $i_{\beta sref}$ as a function of the machine torque. The difficulty in generating the current references in the stationary reference frame can be reduced by using the dq reference frame, provided that the rotor angle is available for direct measurement. Toward this end, recall that the machine torque can be written as a function of dq coordinates as

$$T_e = \frac{3p}{2} \left[\psi_r i_{qs} + (L_{ds} - L_{qs}) i_{ds} i_{qs} \right] \quad (3.109)$$

By setting $i_{ds} = 0$, the expression of the machine torque reduces to

$$T_e = \frac{3p}{2} \psi_r i_{qs} \quad (3.110)$$

Therefore, MPPT algorithm can be achieved by setting $i_{dsref} = 0$ and selecting i_{qsref} as

$$i_{qsref} = \frac{2}{3p\psi_r} T_{r-opt} \quad (3.111)$$

where i_{dsref} and i_{qsref} are the d -axis current reference and q -axis current reference, respectively. By considering the expression of T_{r-opt} , i_{qsref} can be computed as

$$i_{qsref} = \frac{2}{3p\psi_r} K_{opt} \omega_{r-opt}^2 \quad (3.112)$$

where ω_{r-opt} is given by (3.102). Since the control is being conducted in the stationary frame, it is necessary to convert the dq coordinates to $\alpha\beta$ coordinates. That is,

$$\begin{bmatrix} i_{\alpha sref} \\ i_{\beta sref} \end{bmatrix} = \begin{bmatrix} \cos(\theta_e) & -\sin(\theta_e) \\ \sin(\theta_e) & \cos(\theta_e) \end{bmatrix} \begin{bmatrix} i_{dsref} \\ i_{qsref} \end{bmatrix} = \begin{bmatrix} \cos(\theta_e) & -\sin(\theta_e) \\ \sin(\theta_e) & \cos(\theta_e) \end{bmatrix} \begin{bmatrix} 0 \\ i_{qsref} \end{bmatrix} \quad (3.113)$$

where $i_{\alpha sref}$ and $i_{\beta sref}$ are the α -axis current reference and β -axis current reference, respectively. More precisely, these current references are simply the command values for the current controller of PMSG; that is,

$$y_{ref} = \begin{bmatrix} i_{\alpha sref} \\ i_{\beta sref} \end{bmatrix} = \begin{bmatrix} \cos(\theta_e) & -\sin(\theta_e) \\ \sin(\theta_e) & \cos(\theta_e) \end{bmatrix} \begin{bmatrix} 0 \\ \frac{2}{3p\psi_r} K_{opt} \omega_{r-opt}^2 \end{bmatrix} \quad (3.114)$$

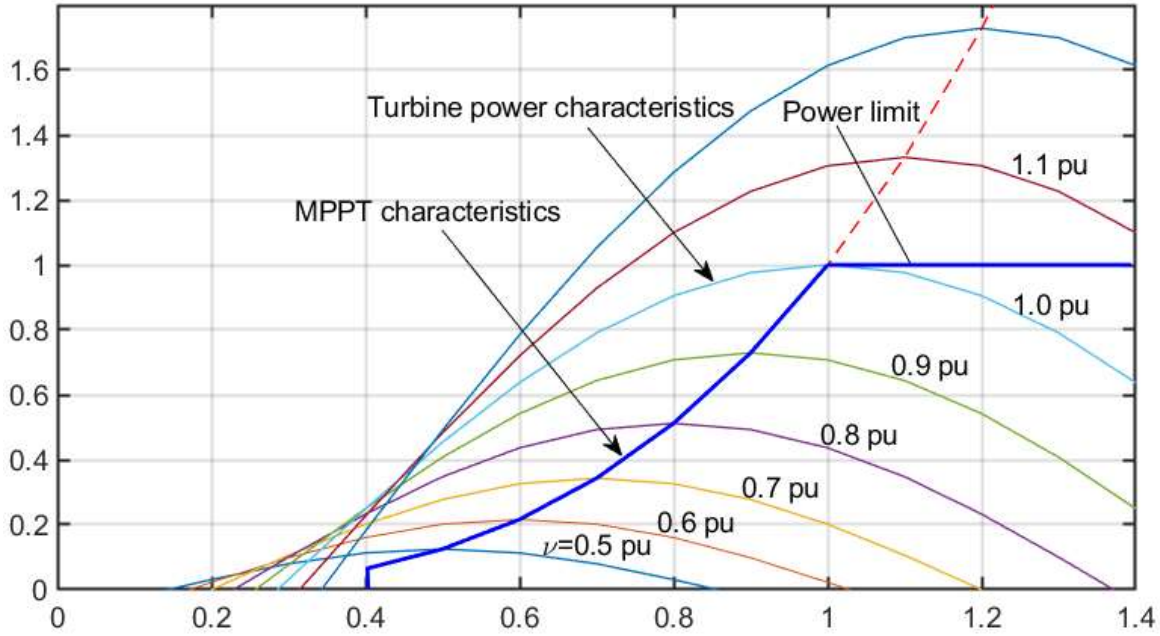


Figure 8: Mechanical power generated by the turbine in y-axis as a function of the rotor speed in x-axis for different wind speeds.

3.4 DC-Link Control under Unbalanced Grid Voltages

Under unbalanced grid voltages, the renewable energy conversion system should be able to inject appropriate active and reactive powers to the grid to satisfy Fault Ride-Through (FRT) requirement. This requirement can be met by considering the grid-side converter for the control of the active and reactive powers injected into the grid, while the dc-link voltage regulation can be achieved through the control of the machine-side converter. In other words, the dc-link voltage is no longer regulated via the grid-side converter. In such a case, the control structure of the machine-side converter consists of two loops: an outer loop is used to regulate the dc-link voltage, while an inner loop is employed to adjust the stator winding currents. The inner current loop for the machine-side converter is basically the same as that developed in the previous subsection; the only modification is that the current reference is generated by an outer voltage loop, rather than by an MPPT algorithm. The outer voltage loop can be designed by using the dynamics of the dc-link that is developed in the previous chapter. That is:

$$\frac{dv_{dc}}{dt} = -\frac{3p\psi_r\omega_r}{2v_{dc}C}i_{qs} - \frac{i_0}{C} \quad (3.115)$$

By setting $v_{dc} = x_v$ and treating i_{qs} as the control input u_{vu} , the above differential equation reduces to

$$\dot{x}_v = A_{vu}x_v + B_{vu}(x_v)u_{vu} + D_{vu}b_{vu} \quad (3.116)$$

where

$$A_{vu} = 0, \quad B_{vu}(x_v) = -\frac{3p\psi_r\omega_r}{2v_{dc}C}, \quad D_{vu} = -\frac{1}{C} \quad (3.117)$$

The disturbance $b_{vu} = i_0 + \delta$, represents the unknown current i_0 and all unknown disturbances that are not considered in the modeling including model uncertainties. As before, the control design for dc-link voltage can be made easier by assuming that:

$$\dot{b}_{vu} = 0 \quad (3.118)$$

Proceeding as in the previous sections, one can develop a composite controller for the dc-link voltage as

$$\begin{aligned} \dot{\hat{z}}_{vu} &= -G_{vu}k_{vu}e_v - G_{vu}\frac{3p\psi_r\omega_r}{2v_{dc}C}\Delta i_{qsref} \\ \hat{b}_{vu} &= \hat{z}_{vu} - G_{vu}e_v \\ i_{qsref} &= -\frac{2v_{dc}C}{3p\psi_r\omega_r}\left(k_{vu}e_v + \dot{v}_{dcref} - \frac{1}{C}\hat{b}_{vu}\right) \end{aligned} \quad (3.119)$$

where i_{qsref} is the output of the outer voltage loop and Δi_{qsref} is given by:

$$\Delta i_{qsref} = i_{qsref} - \text{sat}(i_{qsref}) \quad (3.120)$$

and

$$e_v = v_{dcref} - v_{dc} \quad (3.121)$$

Here, k_{vu} and G_{vu} are the control gain and the observer gain, respectively. As before, the composite controller can be made asymptotically stable by choosing $k_{vu} > 0$ and $G_{vu} > 0$. It can also be shown that fast transient response can be achieved by selecting the gains k_{vu} and G_{vu} as large as possible. As before, had i_{qsref} been generated, the current references $i_{\alpha sref}$ and $i_{\beta sref}$ for the current controller of the machine-side converter may have been computed as

$$y_{ref} = \begin{bmatrix} i_{\alpha sref} \\ i_{\beta sref} \end{bmatrix} = \begin{bmatrix} \cos(\theta_e) & -\sin(\theta_e) \\ \sin(\theta_e) & \cos(\theta_e) \end{bmatrix} \begin{bmatrix} 0 \\ i_{qsref} \end{bmatrix} \quad (3.122)$$

3.5 Power Reference Calculation During Unbalanced Grid Voltages

In the balanced case, the dc-link voltage regulation is carried out on the grid-side converter through the use of a cascaded control scheme consisting of an inner power loop and an outer voltage loop. In this case, the outer voltage loop takes the responsibility of generating the command value for the active power, while command reactive power can be set equal to zero to ensure unity power factor operation. However, in the scenario of an unbalanced grid voltage, the machine-side converter assumes the role of controlling the dc-link voltage so that the grid-side converter only assures the control of active and reactive powers with a view to satisfy Fault Ride-Through (FRT) requirement. In this particular scenario, multiple methodologies have been proposed to generate the command values for the active and reactive powers. In [52], the author provides a discussion on three of the most common methodologies. One approach is known as balanced positive-sequence control (BPSC), which involves oscillating the active and reactive power references in order to ensure that the input currents remain balanced and sinusoidal. Another approach is referred to as Instantaneous Active and Reactive Power Control (IARC), which focuses on suppressing the active and reactive power oscillations while allowing for the presence of multiple harmonics in the phase currents. The final approach is referred to as the Instantaneous Active Power Control (IAPC), which assures injecting constant active power to the grid at the expense of unbalanced grid currents. The strategy employed in this study is the final one, which involves utilizing Instantaneous Active

Power Control (IAPC) with the primary purpose to inject constant active power to the grid. Following [52], the command values for the active and reactive powers are calculated from the following current references in the $\alpha\beta$ reference frame

$$\begin{aligned} i_{\alpha ref} &= i_{\alpha ref}^+ + i_{\alpha ref}^- = \frac{P_{ref0} (v_{\alpha}^+ - v_{\beta}^+)}{|v_{\alpha\beta}^+|^2 - |v_{\alpha\beta}^-|^2} + \frac{Q_{ref0} (v_{\alpha}^+ + v_{\beta}^+)}{|v_{\alpha\beta}^+|^2 + |v_{\alpha\beta}^-|^2} \\ i_{\beta ref} &= i_{\beta ref}^+ + i_{\beta ref}^- = \frac{P_{ref0} (v_{\beta}^+ - v_{\alpha}^+)}{|v_{\alpha\beta}^+|^2 - |v_{\alpha\beta}^-|^2} - \frac{Q_{ref0} (v_{\alpha}^+ + v_{\beta}^+)}{|v_{\alpha\beta}^+|^2 + |v_{\alpha\beta}^-|^2} \end{aligned} \quad (3.123)$$

where v_{α}^- , v_{α}^+ , v_{β}^- , and v_{β}^+ are the positive and negative sequence voltages of the grid voltage in the $\alpha\beta$ reference frame. Here, P_{ref0} is the desired active power reference and $Q_{ref0} = 0$. The command values for the active and reactive powers P_{ref}^{FRT} and Q_{ref}^{FRT} can then be calculated as

$$P_{ref}^{FRT} = \frac{3}{2} (v_{\alpha} i_{\alpha} + v_{\beta} i_{\beta}), \quad Q_{ref}^{FRT} = \frac{3}{2} (v_{\beta} i_{\alpha} - v_{\alpha} i_{\beta}) \quad (3.124)$$

It can be shown that, under balanced grid voltages, $P_{ref} = P_{ref0}$ and $Q_{ref} = P_{ref0}$. On the other hand, voltage unbalance makes Q_{ref} to include oscillation at 2ω , while P_{ref} is kept constant to ensure delivering a constant active power to the grid. The above equations indicate the need for extracting the symmetrical components v_{α}^- , v_{α}^+ , v_{β}^- , and v_{β}^+ to calculate the power references P_{ref} and Q_{ref} . A Double Second-Order Generalized Integrator-Based Quadrature Signal Generator (DSOGI-QSG) strategy is used as a basis to calculate the symmetrical components [84]. As depicted in Figure 9, two (SOGI-QSGs) are responsible for producing the direct and in-quadrature signals for the α -axis and β -axis components of the grid voltage. These signals are subsequently fed into a positive/negative-sequence calculation block, which calculates the sequence components in the $\alpha\beta$ reference frame.

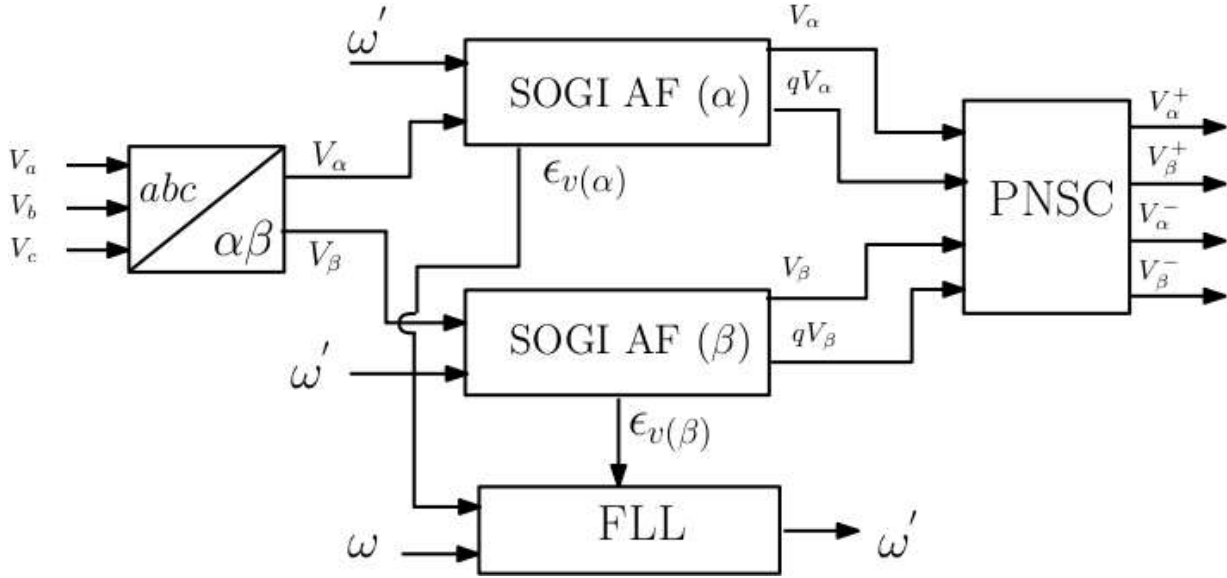


Figure 9: Structure of the DSOGI.

where ω' represent the DSOGI-QSG center frequency, $qv_{\alpha\beta}$ are in-quadrature signals of the voltages $v_{\alpha\beta}$, the synchronization error signal between the direct and in-quadrature signals is represented by the symbol $\epsilon_{v(\alpha\beta)}$.

3.6 Mitigation of 2ω -Oscillation Effect on the Machine Torque under Unbalanced Grid Voltages

During unbalanced grid voltages the proposed controller is designed to inject a constant ripple-free active power and sinusoidal currents into the grid, which requires the reactive power to oscillate with frequency 2ω . Consequently, the implementation of this technique can produce a sinusoidal oscillation with a frequency of 2ω in the dc-link voltage. The observed oscillation can be explained to a continuous transfer of energy between the L filter and the dc link capacitor, as there are no active power oscillations injected into the grid. The periodic transfer of energy can also manifest as an interchange between the dc-link voltage and the stator windings of the PMSG, leading to a torque ripple of 2ω in the PMSG. Given the absence of an external pathway for the oscillation, a viable approach would be to manipulate the controller in order to restrict the cyclic energy transfer to occur only between the L filter and the dc-link capacitor. As a result, the oscillation of the dc-link voltage is

prevented from reaching the stator windings, so effectively eliminating the 2ω ripple originating from the torque of the PMSG. In order to mitigate the impact of 2ω ripple on the voltage controller, a notch filter is implemented to the measurement of the dc-link voltage prior to its input into the dc-link voltage controller. Consequently, only dc component of dc-link voltage measurement is fed into the outer voltage loop. This approach effectively prevents the transmission of the 2ω ripple to the command value for the internal current loop.

This section presents an implementation of notch filters in the machine side converter feedback loop to eliminate the impact of reflected 2ω ripple in machine torque during unbalanced grid condition. The transfer function of the notch filter is given by [85]

$$G_{notch}(s) = \frac{\frac{s^2}{\omega_{notch}^2} + 1}{\frac{s^2}{\omega_{notch}^2} + \frac{2\xi s}{\omega_{notch}} + 1} \quad (3.125)$$

where $\omega_{notch} = 2\omega$ is the notch filter frequency, ξ represents the quality factor that determines the sharpness of the notch filter.

3.7 Simulation Results

In order to assess the effectiveness of the suggested controller, simulation experiments were carried out in the Simulink environment of MATLAB software, embracing both balanced and unbalanced grid voltage scenarios. Figure 10 depicts the block diagram illustrating the implementation of the proposed controller for the grid side and the machine side. The parameters for the Grid system can be found in Table 4: Grid parameters. Additionally, Table 5: PMSG parameters presents the parameters for the machine side PMSG, The settings for the Grid side composite controller may be found in Table 6: Grid side control parameters, whereas the parameters for the machine side composite controller are presented in Table 7: Machine side control parameters. The study examined the effectiveness of the composite controller in regulating active power, dc-link voltage, and machine torque in the presence of both balanced and unbalanced grid voltages. In the case of balanced grid voltage,

the grid side converter GSC is responsible for regulating the dc-link voltage, while the reference active and reactive power is determined by the controller of the dc output voltage through the outer loop. The machine side controller's main function is to maximize power extraction from the wind using the MPPT algorithm. In the context of unbalanced grid voltage, the functions of the Grid-Side Converter GSC and Machine-Side Converter MSC are interchanged. The MSC takes the responsibility of regulating the dc-link voltage, while the outer loop controller provides the reference machine current. On the other hand, the GSC controller is responsible for regulating the active power. In this scenario, the reference active and reactive power are determined using Instantaneous Active Power IAP algorithm.

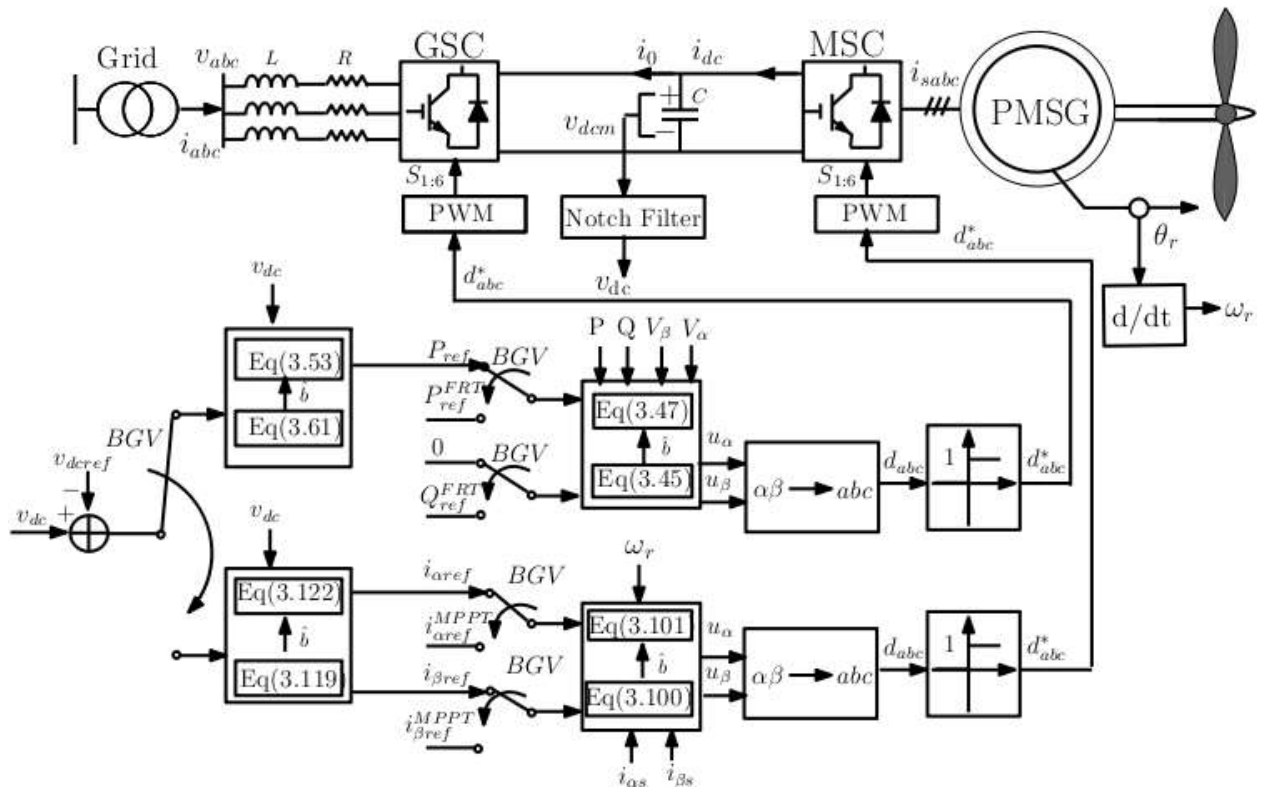


Figure 10: Control diagram for testing the developed controller.

Table 4: Grid parameters

System Parameters	Symbol	Value
Line Resistance	R	$1\text{ m}\Omega$
Line Inductance	L	10 mH
Line-neutral Voltage	v	208 V
DC-Link Voltage	v_{dc}	300 V
DC-Link Capacitor	C	$1\text{ }\mu\text{F}$
Grid Voltage Frequency	ω	50 Hz
Sampling Frequency	f_s	10 KHz
Switching Frequency	f_{sw}	5 KHz
Sampling Time for the simulator	T_s	$1\text{ }\mu\text{S}$

Table 5: PMSG parameters

Machine Parameters	Symbol	Value
Stator Phase Resistance	R_s	$840\text{ m}\Omega$
d -axis inductor	L_{ds}	12.6 mH
q -axis inductor	L_{qs}	21.8 mH
Angular velocity of the rotor	ω_r	200 r/min
flux of the rotor in the stator phase	ψ_r	0.607 Wb
Number of pole pairs	P	11
The air density	ρ	1.225 kg/m^3
The radius of the blade	R_b	1.2 m
The optimum rotor tip speed ratio	λ_{opt}	6.36
The optimum efficiency	C_{Pmax}	0.4382

Table 6: Grid side control parameters

Control Parameters	Symbol	Value
Inner Loop Control Gain	k	1000
Outer Loop Control Gain	k_v	150
Damping Ratio	ζ	0.707
Natural Pulsation 1	ω_{n1}	800 rad/s
Natural Pulsation 2	ω_{n2}	1000 rad/s
Real eigenvalue 1 and 2	$\lambda_{1,2}$	$\zeta\omega_{n1} \pm j\omega_{n1}\sqrt{1-\zeta^2}$
Real eigenvalue 3 and 4	$\lambda_{3,4}$	$\zeta\omega_{n2} \pm j\omega_{n2}\sqrt{1-\zeta^2}$

Table 7: Machine side control parameters

Control Parameters	Symbol	Value
Inner Loop Control Gain	k_s	1000
Outer Loop Control Gain	k_{vu}	150
Damping Ratio	ζ_v	0.707
Natural Pulsation	ω_n	800 rad/s
Observer Gain 1	l_1	$l_1 = 2L\zeta\omega_n$
Observer Gain 2	l_2	$l_2 = -L\left(\frac{\omega_n^2}{\omega} - \omega\right)$

3.7.1 Performance Evaluation under Balanced Grid

The first simulation experiment was conducted during balanced grid voltages, the grid voltages v_{abc} , the three-phase currents i_{abc} , the actual active and reactive powers P and Q and the reference for the active powers P_{ref} the reference for the reactive powers Q_{ref} are presented in Figure 11, while The dc-link voltage v_{dc} , the machine Torque T the machine

current in stationary frame $I_{s\alpha}$ and $I_{s\beta}$ and the reference of machine current $I_{s\alpha ref}$ and $I_{s\beta ref}$ and the machine currents i_{sabc} are shown in Figure 12. The results obtained indicate that the controller in the grid side that was designed successfully maintained the dc-link voltage at its designated setpoint of 370 V. The reason for this outcome is because the suggested controller effectively managed the PWM rectifier, ensuring that the absorbed active power precisely aligns with the specified command value derived from the outer dc voltage loop on the grid side. It is noteworthy that in balanced grid voltages, the active and reactive powers do not exhibit oscillations, as anticipated. Nevertheless, it is worth noting that the machine currents consistently complied with the reference values given by the Maximum Power Point Tracking MPPT algorithm.

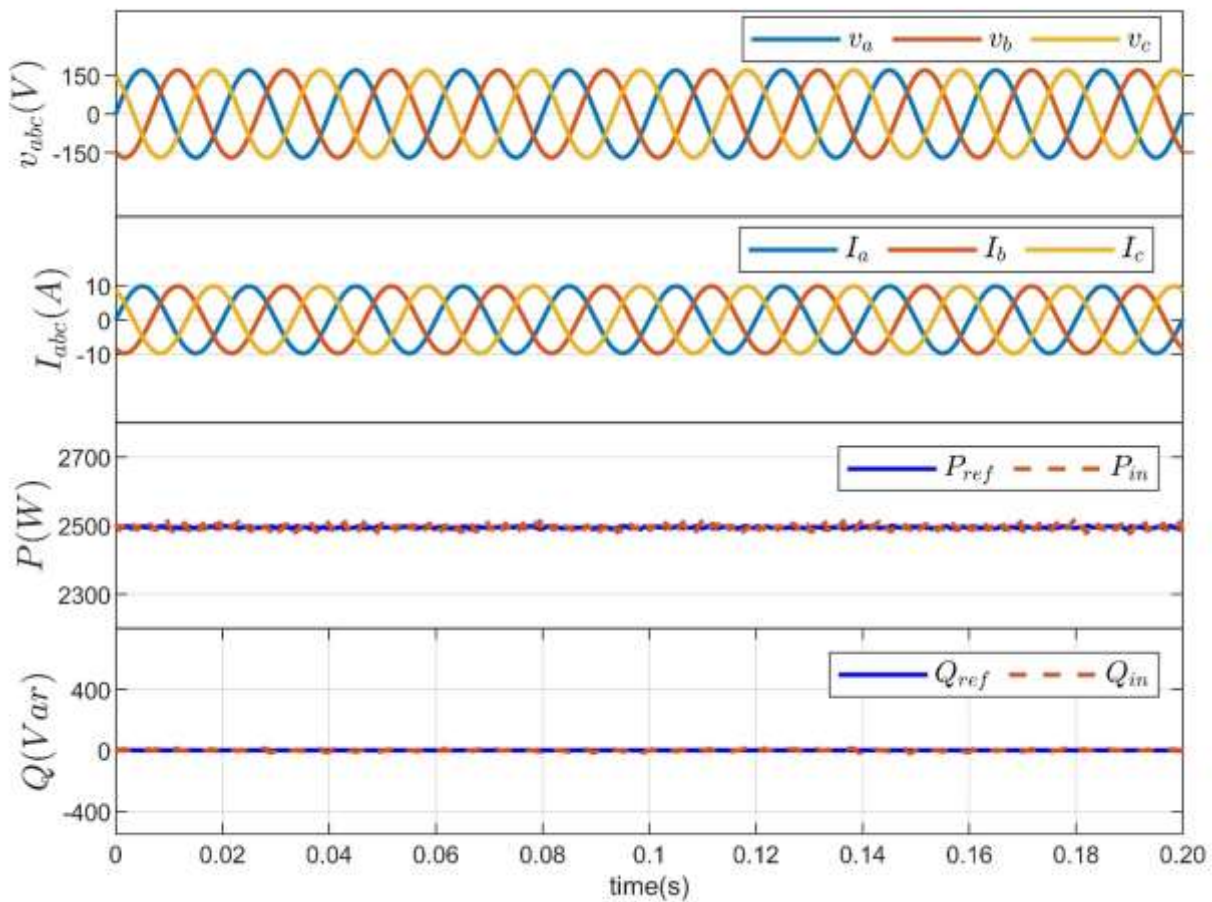


Figure 11: Grid simulation results under balanced grid voltages.

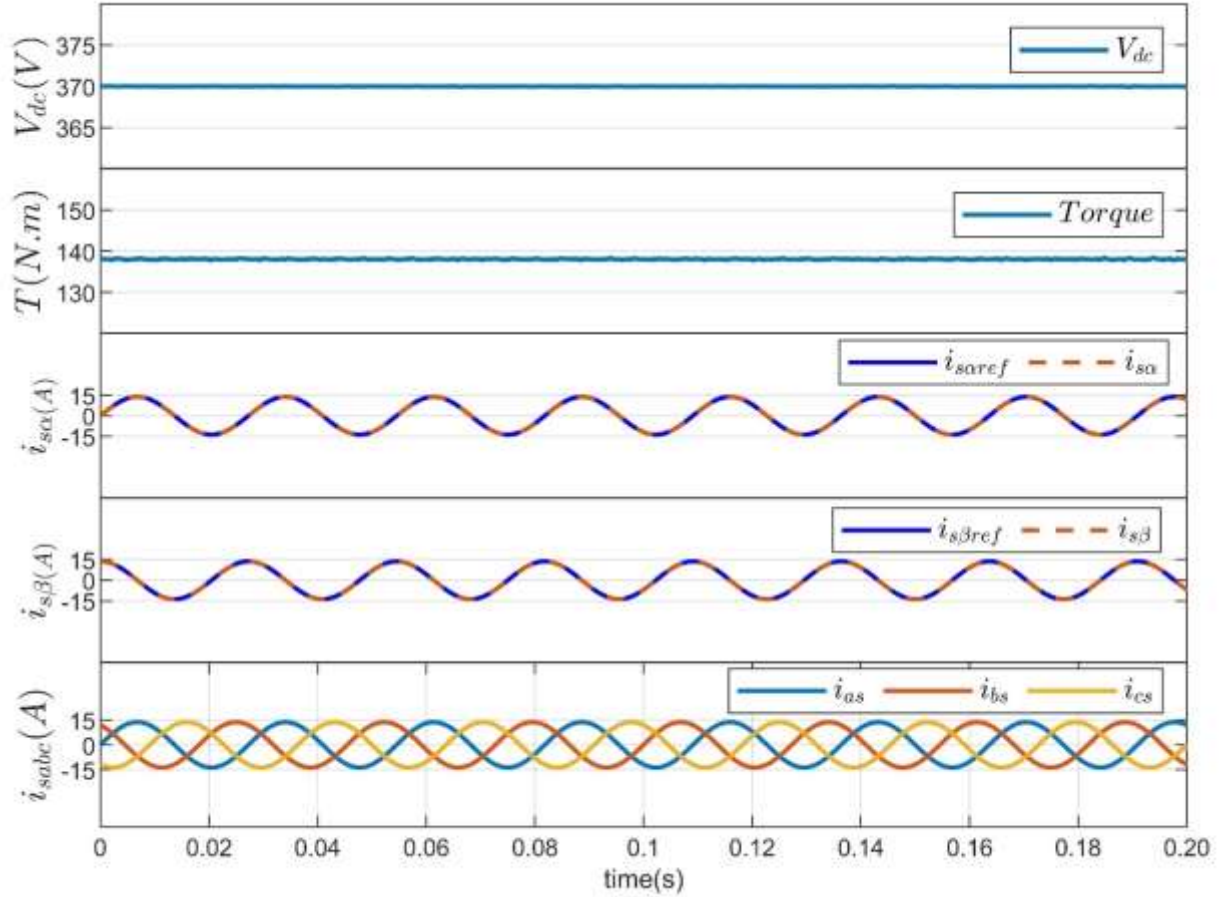


Figure 12: PMSG simulation results under balanced grid voltages.

3.7.2 Performance Evaluation under Unbalanced Grid Voltages without Notch Filter

The conditions used for this test similar to those of the preceding test, with the exception being that of a 50% voltage dip in both phase A and phase B. This alteration was made in order to examine the effectiveness of the proposed controller in the presence of unbalanced grid voltages. Figure 13 illustrates the waveforms of the grid voltages v_{abc} , the grid current I_{abc} , active power P and its reference P_{ref} , reactive power Q and its reference Q_{ref} . On the other hand, Figure 14 displays the dc-link voltage v_{dc} , the machine torque T , and both i_{α} and i_{β} together with their respective references. The purpose of this study is to examine the roles of the GSC and MSC interchanges in relation to the previous test. As predicted, the active power maintains consistent while the reactive powers fluctuate at a frequency of 2ω

around zero, in accordance with the references derived from the Fault Ride Through (FRT) theorem. As expected, the dc-link voltage shows oscillations at a frequency of 2ω due to the unbalanced condition. In this scenario, the machine side takes the responsibility of regulating the dc voltage. However, due to an unbalance in power delivery from the PMSG, the dc voltage is unable to remain constant. As a result, the torque of the machine displays oscillations at a frequency of 2ω , which is considered undesirable due to the creation of mechanical stresses and overheating. These adverse effects can lead to the deterioration of machine components, resulting in a reduced lifespan and potential insulation failure. The machine currents are now regulated based on the command values derived by the outside dc voltage controller, rather than being controlled by the Maximum Power Point Tracking (MPPT) algorithm as previously implemented. The proposed controller demonstrates the capability to achieve consistent regulation of active power and asymptotic regulation of reactive powers. However, it is worth noting that the dc-link voltage and machine torque exhibit oscillations at a frequency of 2ω .

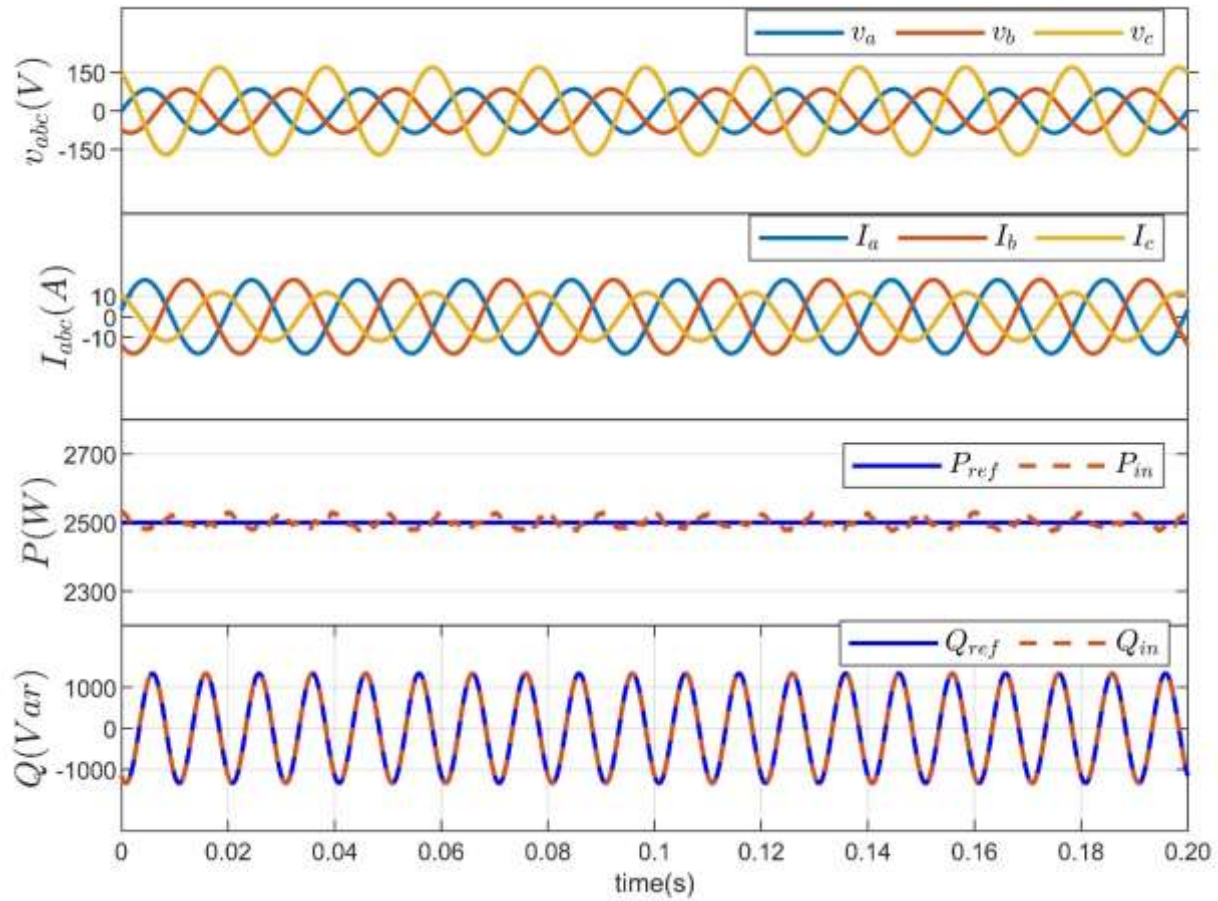


Figure 13: Grid simulation results under unbalanced grid voltages without notch filter.

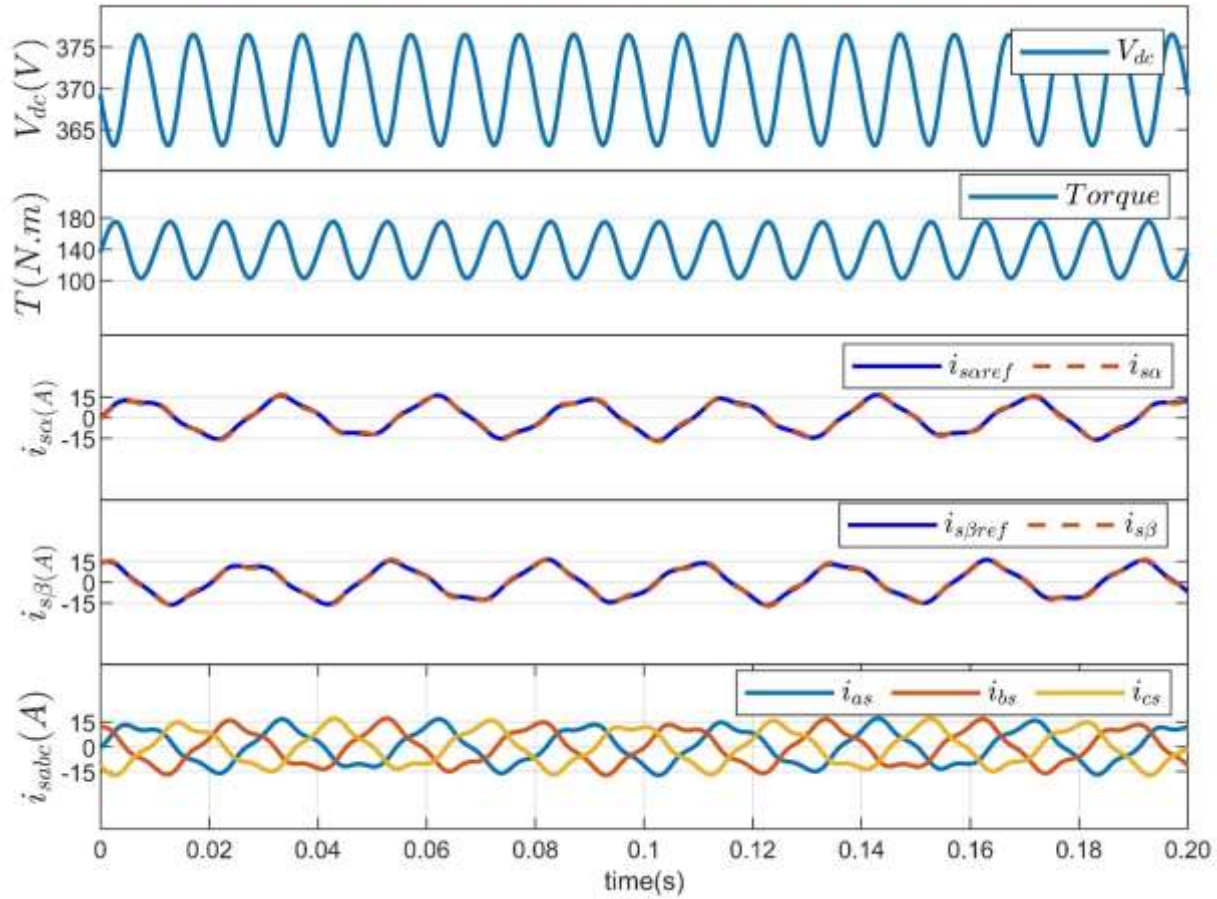


Figure 14: PMSG simulation results under unbalanced grid voltages without notch filter.

3.7.3 Performance Evaluation under Unbalanced Grid Voltages along with Notch Filter

The conditions used for this test are identical to those of the preceding test, with the exception of the inclusion of a notch filter in this study. The purpose of this simulation experiment is to examine the robustness of the controller when integrating a Notch filter into its design. Figure 16 illustrates the impact of incorporating a notch filter, which effectively mitigates the oscillation of the dc-link voltage. This impact of reducing the noise of the torque, hence eliminating the adverse effects associated with oscillating torque, in addition to a balance machine current, as previously discussed. The controller, combined with the notch filter, effectively achieved precise regulation of active and reactive powers delivered to the grid, even in the presence of sinusoidal variations in the reactive power reference. This is

because the composite controller is designed to reject both constant and sinusoidal disturbances of frequency 2ω . Furthermore, it serves the purpose of minimizing the dc-link voltage and ensuring a ripple free torque. This study shows the effectiveness of the notch filter in reducing the impact of dc-link voltage oscillation on the quality of torque generated by the permanent magnet synchronous generator PMSG.

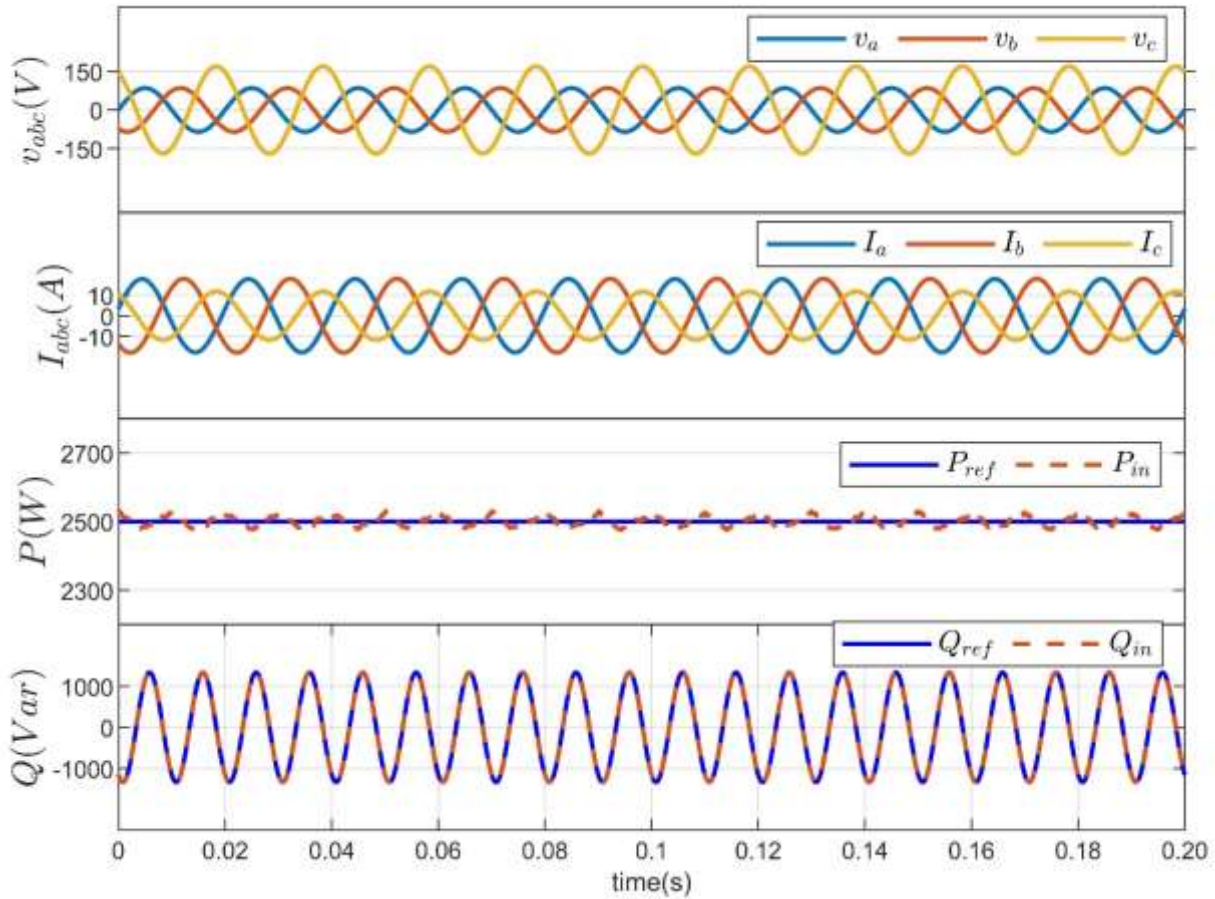


Figure 15: Grid simulation results during unbalanced grid voltages along with notch filter.

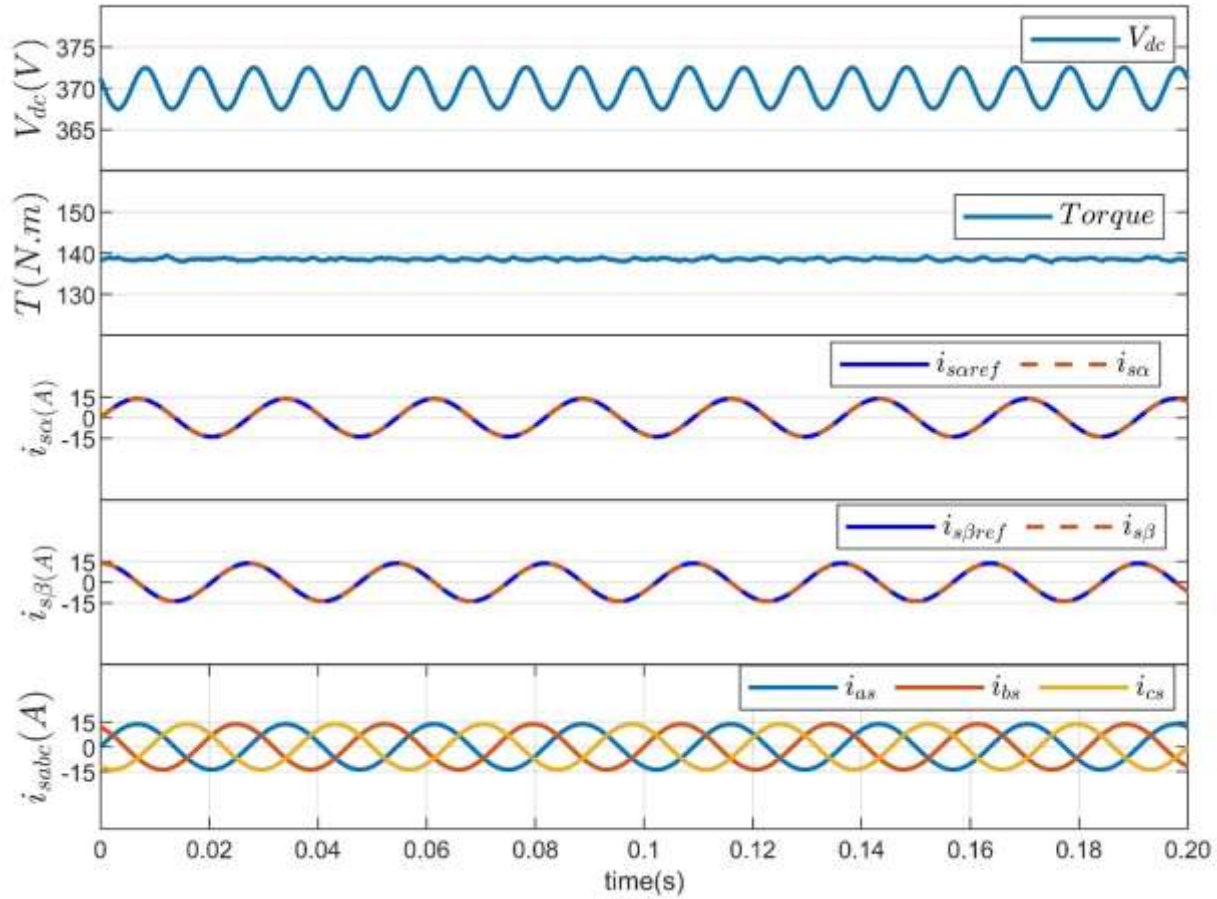


Figure 16: PMSG simulation results under unbalanced grid voltages along with notch filter.

3.7.4 Performance Evaluation of the Disturbance Observer Effect and under Unbalanced Grid Voltages

3.7.4.1 Performance Evaluation of the Disturbance Observer in Grid Side

This study aims to assess the performance of the disturbance in the gride side controller and evaluate the capacity of the feedback controller alone. The test calls for eliminating the disturbance at $t=0.1$ seconds, in other words setting the disturbance value \hat{b} to zero during at this time in the power controller equation (3.47) and it is still running in the machine side. Figure 17 illustrates that in the absence of the disturbance, the feedback controller alone fails to ensure that the active power and reactive power match with their respective references. This indicates that the feedback controller alone lacks the capability to prevent the impacts of

unknown disturbances arising from model uncertainties and voltage unbalance. The active power, in the absence of the disturbance, exhibits oscillations at a frequency twice that of the fundamental frequency. This behavior contradicts the intended objective of the controller. However, because of the oscillating active power, the dc-link voltage ripples mitigate, as depicted in Figure 18.

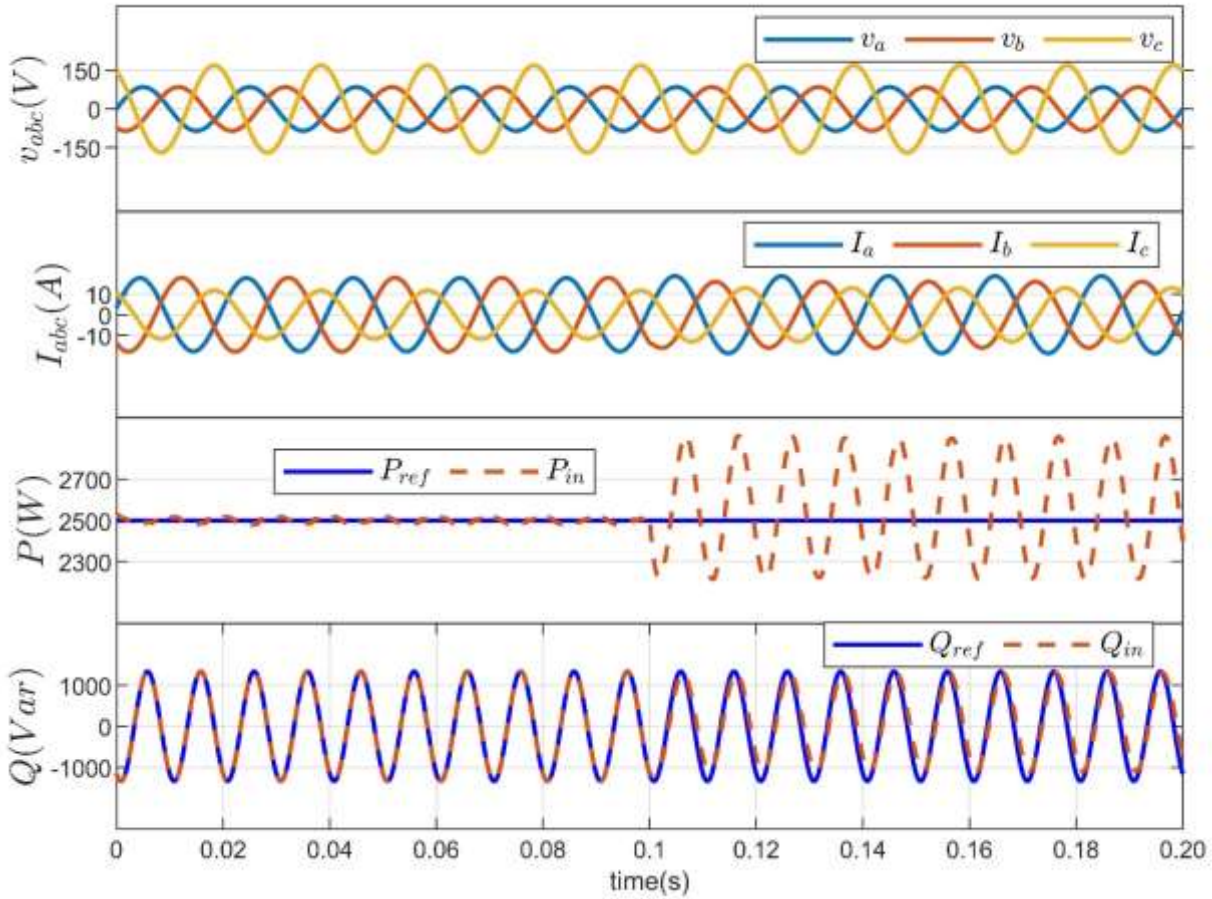


Figure 17: Grid simulation results when the disturbance observer was disabled at $t = 0.1$ s from the grid.

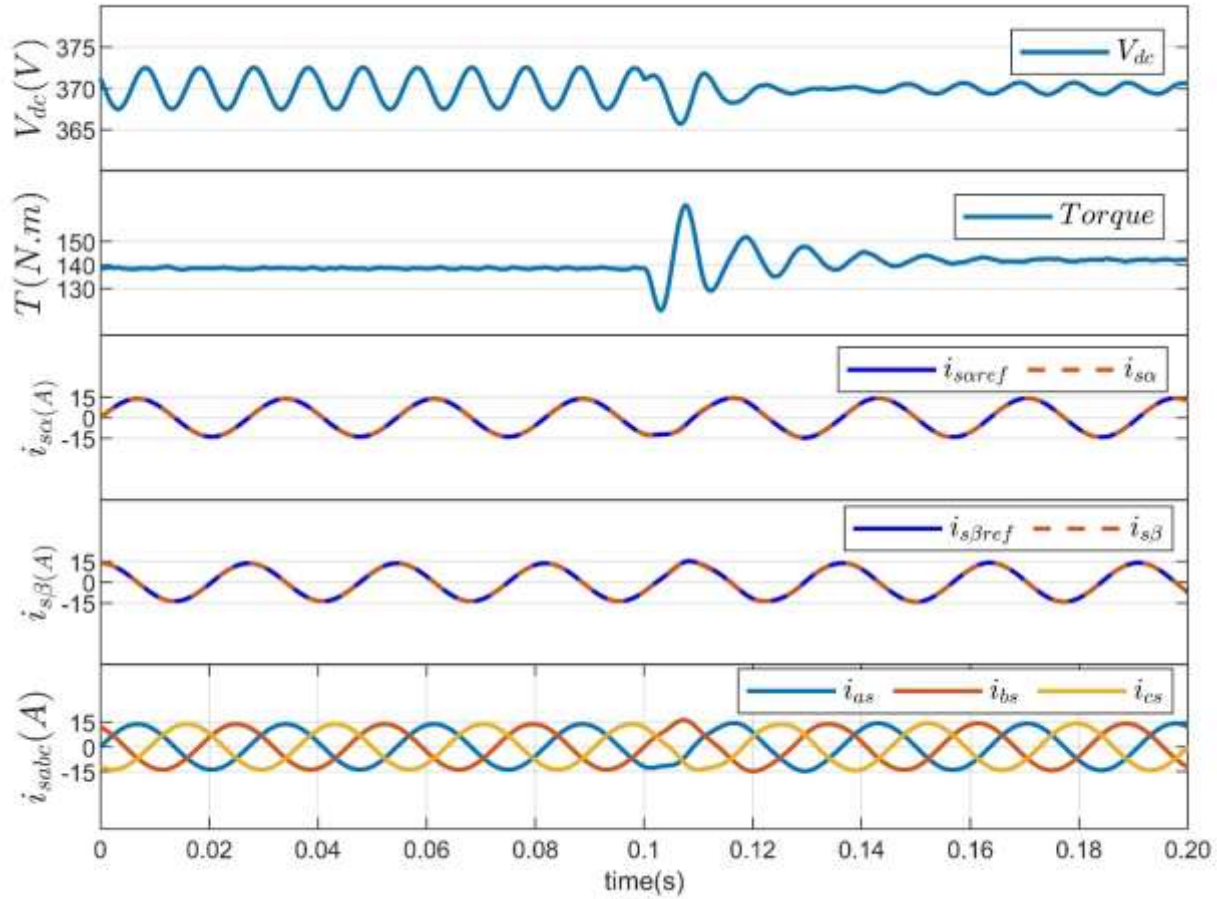


Figure 18: PMSG simulation results when the disturbance observer was disabled at $t = 0.1$ s from the grid.

3.7.4.2 Performance Evaluation of the Disturbance Observer in Machine Side

The objective of this study is to analyze the performance of the disturbance in the Machine side controller and evaluate the effectiveness of the feedback controller in isolation. The simulation experiment involves removing the disturbance at $t=0.1$ seconds, specifically by setting the disturbance value to zero in the current controller equation (3.101), while the grid side disturbance continues to operate. Figure 20 demonstrates that in the absence of the disturbance, the feedback controller alone is unable to ensure that the machine current matches their respective references. This suggests that the feedback controller alone does not possess the capability to mitigate the effects of unknown disturbances resulting from model uncertainties and voltage unbalance.

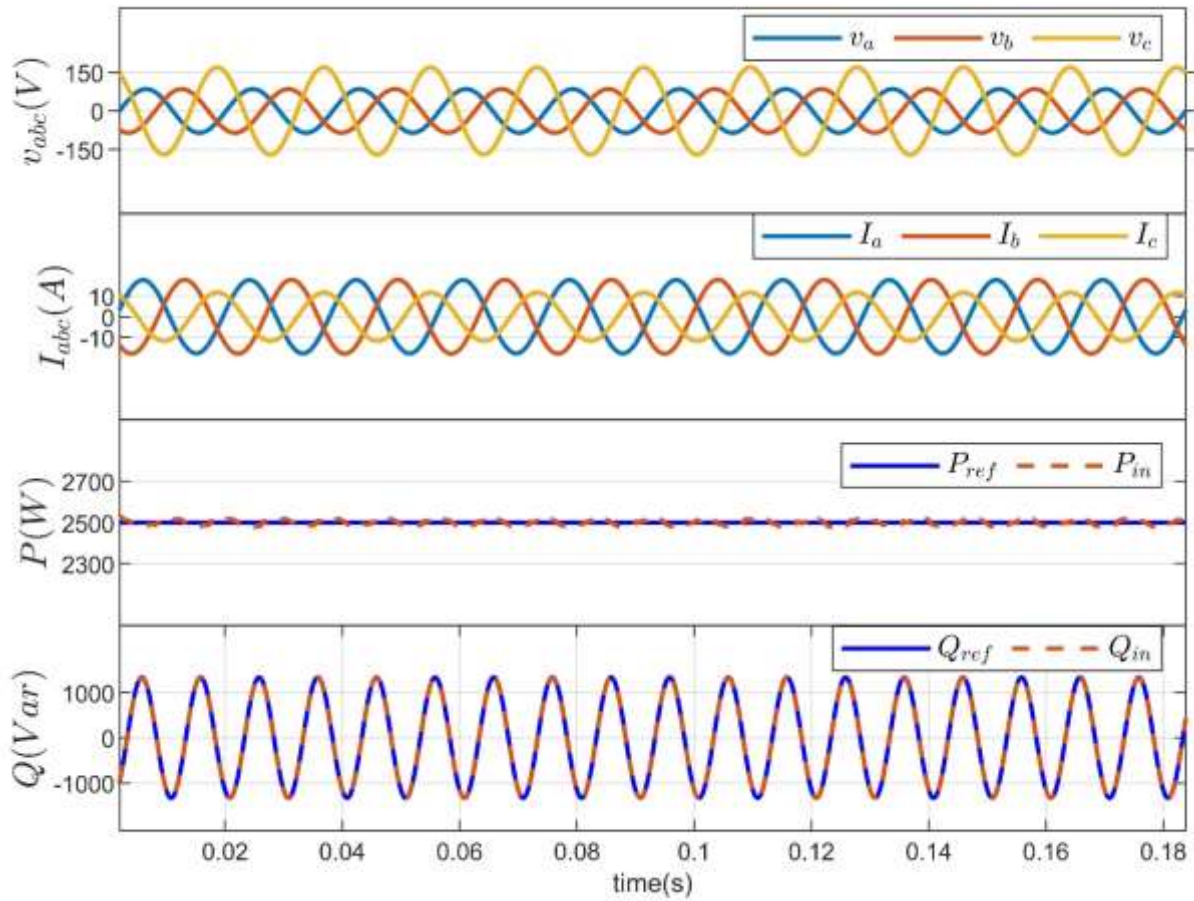


Figure 19: Grid simulation results when the disturbance observer was disabled at $t = 0.1$ s from the machine.

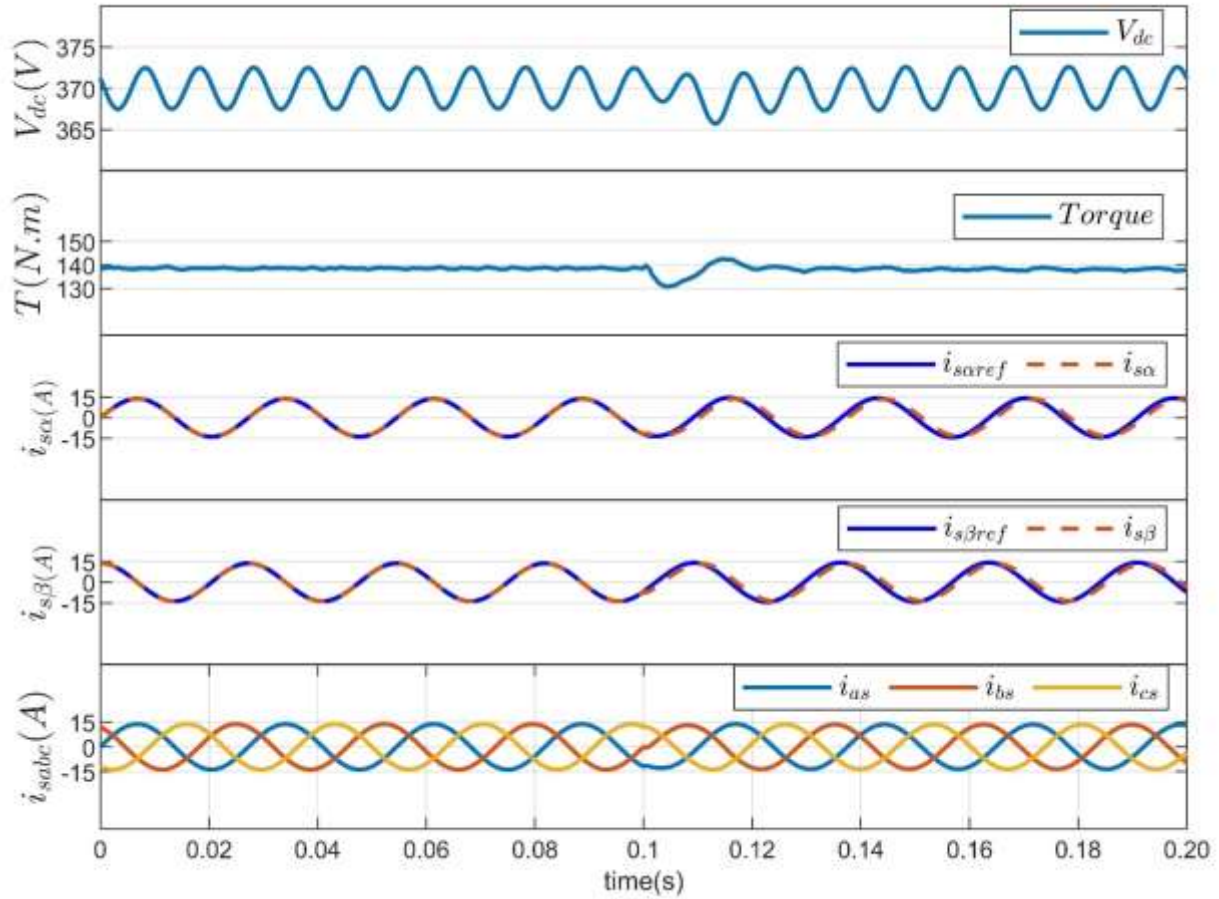


Figure 20: PMSG simulation results when the disturbance observer was disabled at $t = 0.1$ s from the machine.

3.7.5 Performance Evaluation under a Grid Condition Transition

The objective of this simulation experiment was to investigate the dynamic behavior of the composite controller and to assess the reconfigurable capability of the control function between the machine side converter MSC and the grid side controller GSC under varying grid conditions, specifically transitioning from a balanced grid to an unbalanced grid and then returning to a balanced grid. At $t=0.04$ seconds, a voltage dip of 50% is induced in phase B, which is later fixed at $t=0.14$ seconds. The simulation results are depicted in Figure 21 and Figure 22. The results obtained demonstrated the effective performance of the proposed controller in generating fast and seamless reconfiguration to a sudden disturbance. The occurrence of voltage imbalance and subsequent fault clearance had a small impact on the

transient response of active power, as well as the dc-link voltage and resulting torque. The simulation results indicate that altering the transition between grid balance and imbalance does not affect the machine currents. The currents continue to precisely follow their references without any transient behavior.

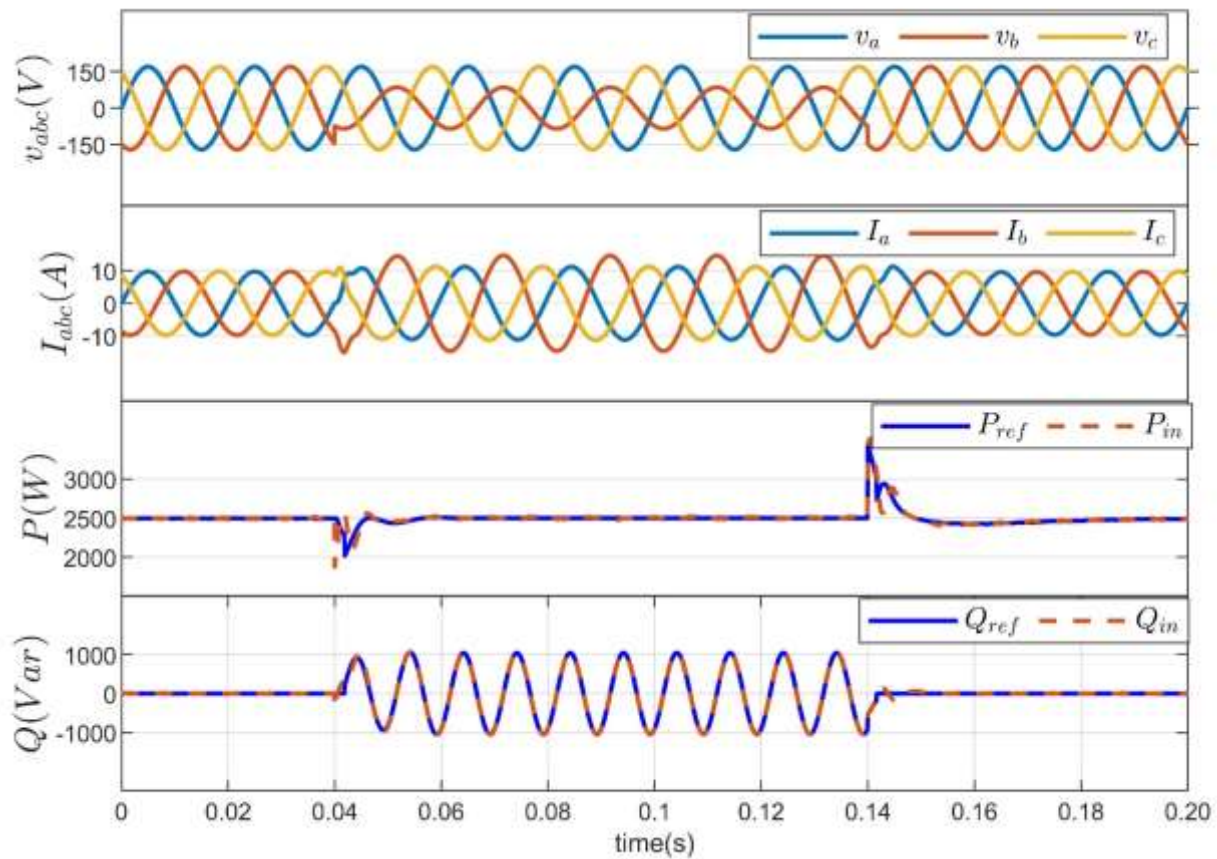


Figure 21: Grid simulation results when 50% dip in Phase B was suddenly created at $t = 0.04$ s to 0.14 s.

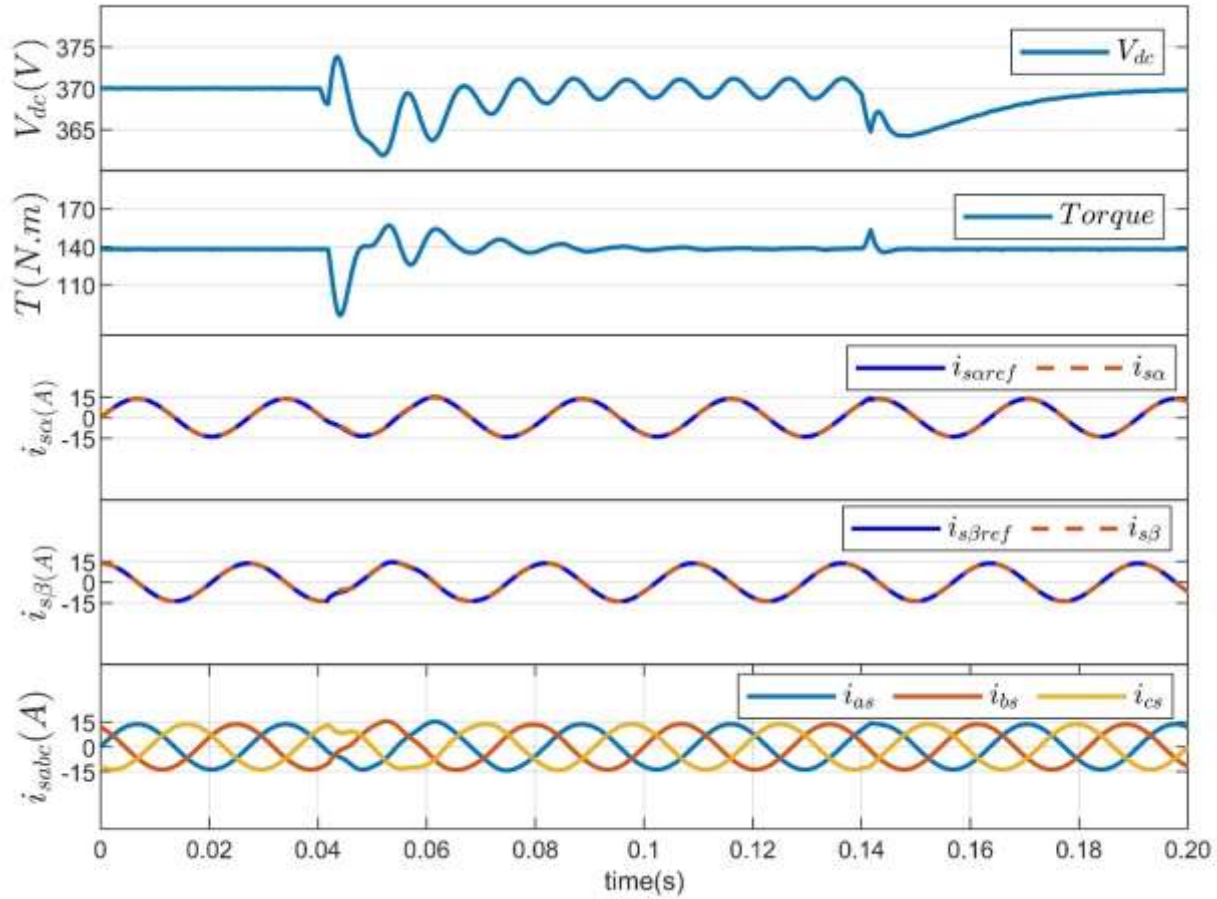


Figure 22 : PMSG simulation results when 50% dip in Phase B was suddenly created at $t = 0.04$ s to 0.14 s.

3.7.6 Performance Evaluation under Model Uncertainties and Unbalanced Grid Voltages

The purpose of this simulation experiment was to assess the controller's ability to withstand changes in parameters. Specifically, the inductance and resistance values of the controller were adjusted to 150% of their nominal levels. Furthermore, the simulation was conducted using unbalanced grid condition, and the outcomes are presented in Figure 23 and Figure 24. The results indicate that alterations in the variables L and R did not have an impact on the control performances. The variation between the actual and the nominal parameters was compensated for by the estimator \hat{b} . The effectiveness of the composite controller was demonstrated by the exact match between the actual power and its desired reference value.

which led to robust regulation of the active and reactive power, dc-link voltage, machine torque and currents.

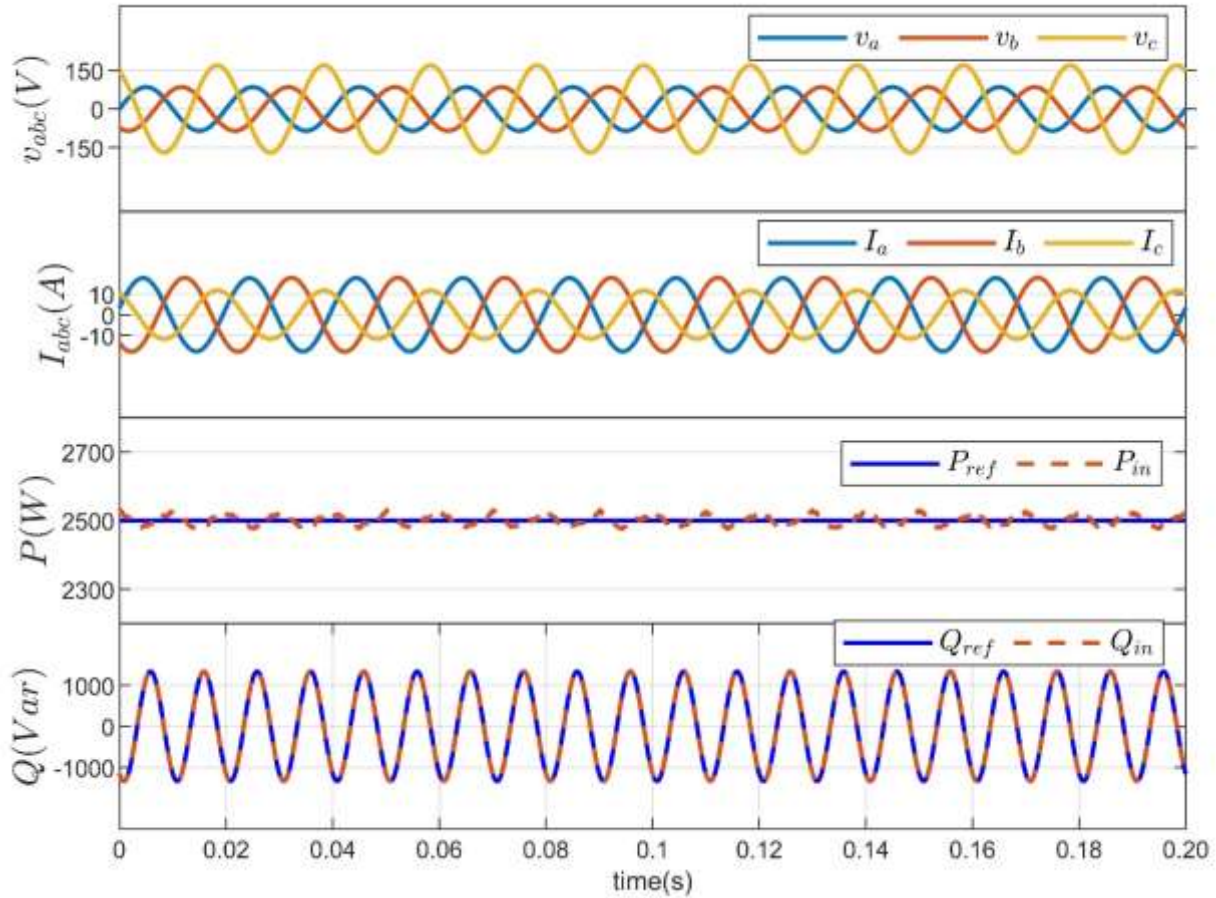


Figure 23: Grid simulated outcomes of the grid when the resistance R and inductance L utilized in the controller are increased by 150% of their nominal values.

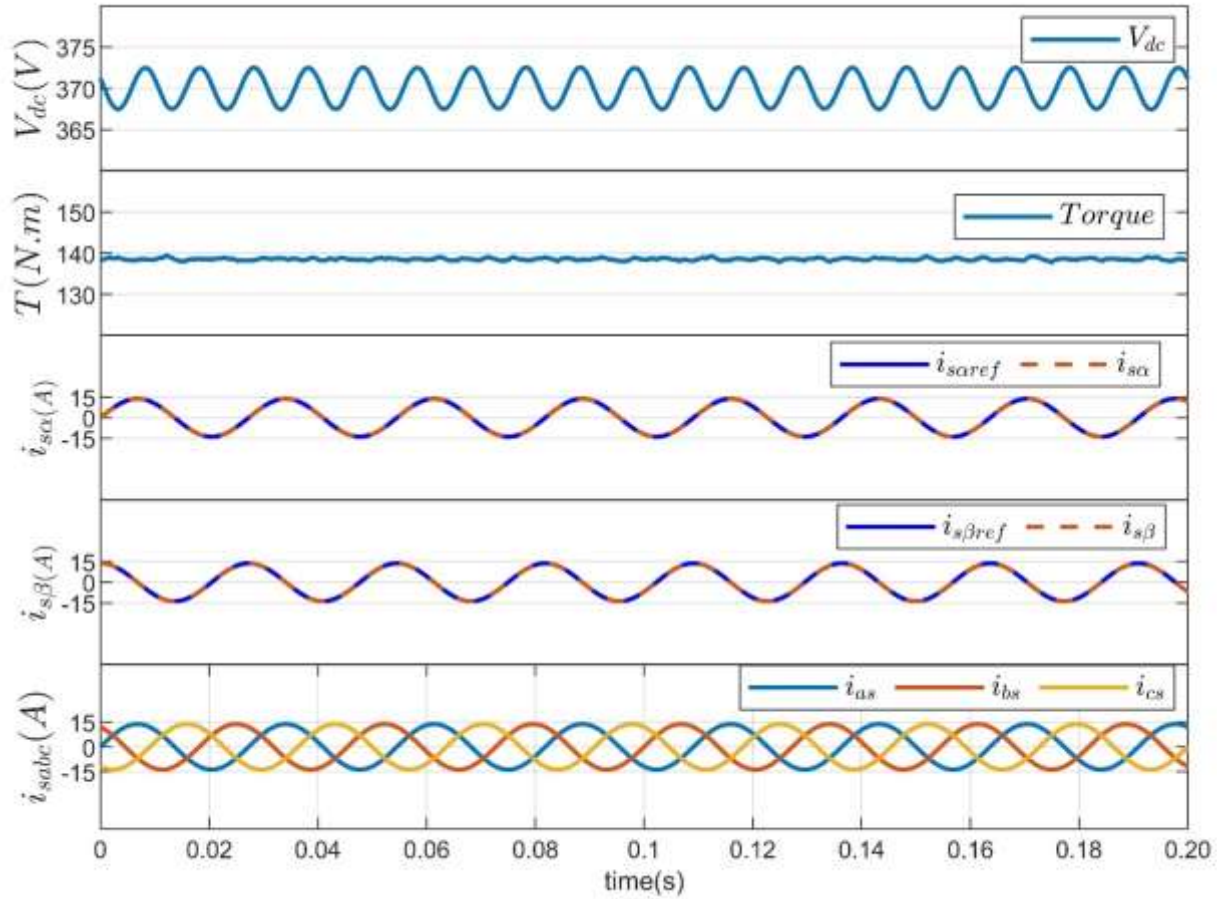


Figure 24: PMSG simulated outcomes of the grid when the resistance R and inductance L utilized in the controller are increased by 150% of their nominal values.

3.8 Summary

This chapter presents the design of an interchanged controller for both the grid side and machine side converter. The controller incorporates a combined feedback controller and disturbance observer along with a notch filter. The specific function of the controller depends on the condition of the grid. Under balanced grid conditions, the grid side is responsible for regulating the dc-link voltage by generating the power reference for an inner loop control. Meanwhile, in this condition, the machine side's role is to maximize power extraction from the wind by controlling the stator currents to follow a reference value provided by an MPPT algorithm. In situations where there is an imbalance in grid voltage, the roles of the controllers

are interchanged. The grid side controller takes charge of regulating the active and reactive powers. In this particular scenario, the reference value is determined using an instantaneous active power algorithm to maintain a constant active power supply to the grid. On the other hand, the machine side controller is responsible for regulating the dc-link voltage by controlling the machine currents. These currents are adjusted to align with the references generated from the inner loop. In this particular scenario, it is observed that an imbalance in the grid voltage can result in the generation of second-order harmonic ripples in the dc-link voltage. Consequently, this can lead to the occurrence of a sinusoidal oscillation with a frequency of 2ω in the torque of the PMSG. In order to mitigate this oscillation, a notch filter is utilized. Several simulation tests have been performed in order to verify the efficacy of the composite controller. The findings obtained from the simulation confirm the effectiveness of the control scheme in successfully attaining the targeted control objectives in the presence of both balanced and unbalanced grid voltages.

Chapter 4: Control of PMSG in Synchronous Reference Frame

The preceding chapter has presented the use of DOBC approach to implement a reconfigurable control scheme for PMSG-based wind turbine. Under balanced grid voltages, the control scheme uses GSC to regulate the dc-link voltage via controlling the active power injected into the grid, while MSC is employed to control PMSG to extract maximum available power from the wind. Under unbalanced grid voltages, the reconfigurability property of the control scheme allows interchanging the roles of the power converters in terms of dc-link voltage regulation. That is, MSC assumes the role of regulating the dc-link voltage via controlling the stator currents of PMSG, while GSC takes charge of regulating the active and reactive powers injected into the grid to implement FRT control strategy. The controllers for both GSC and MSC are designed in the stationary $\alpha\beta$ reference frame. The obtained results in the previous chapter provide evidence of the effectiveness and importance of the proposed reconfigurable control scheme in terms of meeting the grid connection requirement under both balanced and unbalanced grid voltages. More importantly, as demonstrated before, the use of the disturbance observed approach allows achieving a seamless reconfiguration of the control scheme in response to sudden changes in the grid voltage conditions.

The design procedure in this chapter is similar to that of the previous one except that the $\alpha\beta$ reference frame is replaced by dq reference frame. Besides, the power control scheme of GSC is also replaced by a current control scheme using dq coordinates. Literature review reveals that constant active power operation under unbalanced grid voltages requires dq -axis components of grid currents to oscillate around their dc components at twice the fundamental frequency. This requires the current controller of GSC to be capable of accurately tracking a sinusoidal reference signal with a non-zero dc component. As in the previous chapter, DOBC approach is employed to achieve the task of accurate tracking through the use of an accurate disturbance observer. The latter is employed to estimate the effect of model uncertainties, unknown perturbations, and unknown inputs that are not considered in the state model. The main concern for designing an accurate disturbance is the need for accurate information about the behavior of the disturbance input. As in the previous chapter, this requirement can be

simplified by assuming that the dynamics of the disturbance input is the same as that of the state variables in steady-state [74]. With this particular assumption, appropriate disturbance observer can be designed to improve the accuracy of the composite controller, consisting of state-feedback controller and disturbance observer. The same design procedure is applied to synthesize a regulator for the dc-link voltage, where the disturbance input is assumed to be constant. Similarly, DOBC approach has been also employed to design a current controller for the stator currents of PMSG using dq coordinates. The effectiveness of the suggested control method was validated through a series of simulated tests. The findings obtained have verified the effectiveness of the control system in attaining the control objectives in the presence of both balanced and unbalanced grid voltages. Figure 25 depicts a comprehensive cascaded current control technique in the dq synchronous frame.

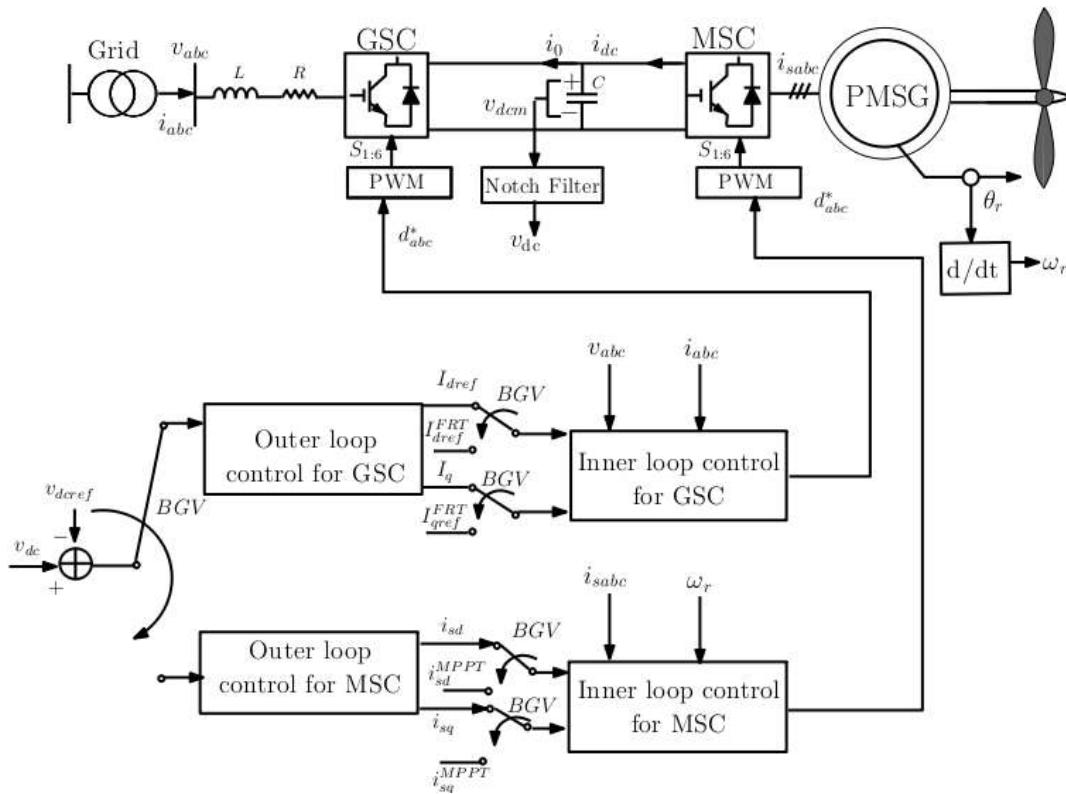


Figure 25: General current control scheme.

4.1 Current Control of the Grid-Side Converter

4.1.1 Perturbed Model of the Grid-Side Converter

The model of a grid-connected three-phase inverter with an L filter in synchronous frame is given by (2.17)

$$\frac{d}{dt} \begin{bmatrix} i_d \\ i_q \end{bmatrix} = -\frac{R}{L} \begin{bmatrix} i_d \\ i_q \end{bmatrix} + \begin{bmatrix} -\omega i_q \\ \omega i_d \end{bmatrix} + \frac{1}{L} \begin{bmatrix} u_d \\ u_q \end{bmatrix} - \frac{1}{L} \begin{bmatrix} v_d \\ 0 \end{bmatrix} \quad (4.1)$$

By considering model uncertainties (b), the model can be represented as

$$\begin{aligned} \dot{x}_i &= A_i x_i + B_i u_i + F_i + D_i b_i \\ y_i &= C_i x_i \end{aligned} \quad (4.2)$$

where $x_i = [i_d \ i_q]^T$ and $u_i = [u_d \ u_q]^T$ are the state variables and the control input, respectively. The matrices A_i , B_i , C_i , D_i , and F_i are given by:

$$A_i = \begin{bmatrix} -\frac{R}{L} & \omega \\ \omega & -\frac{R}{L} \end{bmatrix}, \quad B_i = \begin{bmatrix} \frac{1}{L} & 0 \\ 0 & \frac{1}{L} \end{bmatrix}, \quad C_i = \begin{bmatrix} 1 & 0 \\ 0 & 1 \end{bmatrix}, \quad F_i = -\frac{1}{L} \begin{bmatrix} v_d \\ 0 \end{bmatrix}, \quad D_i = \begin{bmatrix} \frac{1}{L} & 0 \\ 0 & \frac{1}{L} \end{bmatrix} \quad (4.3)$$

The disturbance input b_i as well as the output y_i are given by:

$$b_i = \begin{bmatrix} b_{id} \\ b_{iq} \end{bmatrix}, \quad y_i = \begin{bmatrix} i_d \\ i_q \end{bmatrix} \quad (4.4)$$

4.1.2 Feedback Controller

The primary objective of the controller is to effectively regulate the output y_i , in order to achieve precise tracking of the sinusoidal reference y_{ref} . To achieve this objective, a state-feedback control law can be formulated in the form:

$$u_i = B_i^{-1} (K_i e_i + \dot{y}_{iref} - A_i x_i - F_i - D_i b_i) \quad (4.5)$$

where k_i is the control gain and $e_i = y_{iref} - y_i$ is the tracking error. It is important to mention that y_i and y_{iref} represent the dq current and its reference, respectively. The current is the

output that has to be regulated. The main goal of the feedback controller is to make sure that the controlled variable closely follows its reference pattern in a specific time frame with zero steady-state error, provided that the closed-loop system is stable. Indeed, the stability of the closed-loop system can be investigated by studying the closed-loop error dynamics. This can be achieved by substituting (4.5) into (4.2) , resulting in

$$\dot{e}_i = -k_i e_i \quad (4.6)$$

where

$$e_i = y_{iref} - y_i = \begin{bmatrix} \dot{i}_{dref} - \dot{i}_d \\ \dot{i}_{qref} - \dot{i}_q \end{bmatrix}, \quad (4.7)$$

The behavior of the closed-loop system can be accurately described by a first-order system with a time constant equal to $1/k_i$. Therefore, as the value of k_i increases, the speed of the system's response also increases. The proposed feedback controller may not be available for actual implementation due to the difficulty in measuring the disturbance b_i . In order to overcome this constraint, a possible resolution entails replacing the actual disturbance b_i with its estimated equivalent \hat{b}_i , provided that a suitable estimator capable of producing \hat{b}_i is accessible. Thus, the altered controller might be depicted in the following manner.

$$u_i = B_i^{-1} \left(K_i e_i + \dot{y}_{iref} - A_i x_i - F_i - D_i \hat{b}_i \right) \quad (4.8)$$

4.1.3 Disturbance Observer

As mentioned before, estimating the disturbance is necessary for implementing the feedback controller. In order to achieve precise estimation of sinusoidal disturbances, it is necessary to utilize a disturbance observer. Moreover, b_i can also be employed to demonstrate the impact of voltage unbalance on modeling. The injection of constant active power to the grid may result in second-order harmonics in the d -axis current and q -axis current due to unbalanced grid voltages. In the absence of exact information about the disturbance, one can assume that has b_i the same dynamics as that of the dq -axis current components. Therefore, one can write $b_i = [b_{id} \quad b_{iq}]$ as

$$b_{id} = \bar{b}_{id} + \tilde{b}_{id}, \quad b_{iq} = \bar{b}_{iq} + \tilde{b}_{iq} \quad (4.9)$$

where \bar{b}_{id} and \bar{b}_{iq} are the dc components of b_{id} and b_{iq} . The terms \tilde{b}_{id} and \tilde{b}_{iq} are ac signals that oscillate at twice the fundamental frequency. Specifically, \tilde{b}_{id} and \tilde{b}_{iq} can be expressed as

$$\tilde{b}_{id} = b_{idM} \cos(2\omega t + \psi_{id}), \quad \tilde{b}_{iq} = b_{iqM} \cos(2\omega t + \psi_{iq}) \quad (4.10)$$

where b_{idM} , b_{iqM} , ψ_{id} , and ψ_{iq} are unknown variables. The time derivatives of \tilde{b}_{id} and \tilde{b}_{iq} are then given by

$$\dot{\tilde{b}}_{id} = b_{idM} 2\omega \sin(2\omega t + \psi_{id}), \quad \dot{\tilde{b}}_{iq} = b_{iqM} 2\omega \sin(2\omega t + \psi_{iq}) \quad (4.11)$$

As \bar{b}_{id} and \bar{b}_{iq} are dc components, it is clear that:

$$\dot{\bar{b}}_{id} = 0, \quad \dot{\bar{b}}_{iq} = 0 \quad (4.12)$$

The time derivatives of \tilde{b}_{id} and \tilde{b}_{iq} is described as non-linear and time-varying functions. These functions are formulated based on certain unknown parameters, specifically b_{idM} , b_{iqM} , ψ_{id} , and ψ_{iq} . Therefore, the process of utilizing such functions for the purpose of constructing a DO is not straightforward. To facilitate the design process of the disturbance observer, it is possible to incorporate auxiliary disturbance inputs σ_{id} and σ_{iq} with the purpose of simplifying the process such that:

$$\sigma_{id} = 2\omega b_{idM} \cos(2\omega t + \psi_{id}), \quad \sigma_{iq} = 2\omega b_{iqM} \cos(2\omega t + \psi_{iq}) \quad (4.13)$$

The time derivatives of the auxiliary disturbance inputs σ_{id} and σ_{iq} are given by:

$$\dot{\sigma}_{id} = -4\omega^2 b_{idM} \sin(2\omega t + \psi_{id}) = -4\omega^2 \tilde{b}_{id}, \quad \dot{\sigma}_{iq} = -4\omega^2 b_{iqM} \sin(2\omega t + \psi_{iq}) = -4\omega^2 \tilde{b}_{iq} \quad (4.14)$$

Likewise, it can be shown that:

$$\begin{aligned}\dot{\bar{b}}_{id} &= 0, & \dot{\tilde{b}}_{id} &= \sigma_{id}, & \dot{\sigma}_{id} &= -4\omega^2 \tilde{b}_{id} \\ \dot{\bar{b}}_{iq} &= 0, & \dot{\tilde{b}}_{iq} &= \sigma_{iq}, & \dot{\sigma}_{iq} &= -4\omega^2 \tilde{b}_{iq}\end{aligned}\quad (4.15)$$

Let z_i represent a newly introduced state variable such that:

$$z_i = \begin{bmatrix} \bar{b}_{id} & \bar{b}_{iq} & \tilde{b}_{id} & \tilde{b}_{iq} & \sigma_{id} & \sigma_{iq} \end{bmatrix}^T \quad (4.16)$$

Therefore, equation (4.15) can be rewritten in a compact form as:

$$\begin{aligned}\dot{z}_i &= \Omega_i z_i \\ b_i &= H_i z_i\end{aligned}\quad (4.17)$$

where

$$\Omega_i = \begin{bmatrix} 0_{2 \times 2} & 0_{2 \times 2} & 0_{2 \times 2} \\ 0_{2 \times 2} & 0_{2 \times 2} & I_{2 \times 2} \\ 0_{2 \times 2} & -4\omega^2 I_{2 \times 2} & 0_{2 \times 2} \end{bmatrix}, \quad H_i = \begin{bmatrix} I_{2 \times 2} \\ I_{2 \times 2} \\ 0_{2 \times 2} \end{bmatrix}^T \quad (4.18)$$

Substituting $b_i = H_i z_i$ into (4.2) yields

$$\dot{x}_i = A_i x_i + B_i u_i + F_i + D_i H_i z_i \quad (4.19)$$

Following [81], the full order disturbance observer can be formulated for estimating \hat{b}_i as

$$\begin{aligned}\hat{\dot{x}}_i &= A_i x_i + B_i u_i + F_i + D_i \hat{b}_i + G_{1i} (y_i - \hat{y}_i) \\ \hat{\dot{z}}_i &= \Omega_i z_i + G_{2i} (y_i - \hat{y}_i) \\ \hat{b}_i &= H_i \hat{z}_i\end{aligned}\quad (4.20)$$

As mentioned before, the observer gains G_{1i} and G_{2i} can be selected based on the stability condition of the disturbance observer. With $y_i = x_i$ and $\hat{y}_i = \hat{x}_i$, the stability of the observer can be investigated by analyzing the dynamics of the estimation error e_{iobs} , given by

$$e_{iobs} = \begin{bmatrix} \hat{x}_i - x_i \\ \hat{z}_i - z_i \end{bmatrix} \quad (4.21)$$

The estimation error is governed by the following differential equation:

$$\begin{aligned} \dot{e}_{iobs} &= \begin{bmatrix} \dot{\hat{x}}_i \\ \dot{\hat{z}}_i \end{bmatrix} - \begin{bmatrix} \dot{x}_i \\ \dot{z}_i \end{bmatrix} = \begin{bmatrix} A_i x_i + B_i u_i + F_i + D_i H_i \hat{z}_i \\ \Omega_i \hat{z}_i \end{bmatrix} + \begin{bmatrix} G_{1i} \\ G_{2i} \end{bmatrix} (y_i - \hat{y}_i) - \begin{bmatrix} A_i x_i + B_i u_i + F_i + D_i H_i z_i \\ \Omega_i z_i \end{bmatrix} \\ &= \begin{bmatrix} D_i H_i \hat{z}_i - D_i H_i z_i \\ \Omega_i \hat{z}_i - \Omega_i z_i \end{bmatrix} + \begin{bmatrix} G_{1i} \\ G_{2i} \end{bmatrix} (y_i - \hat{y}_i) = \begin{bmatrix} D_i H_i (\hat{z}_i - z_i) \\ \Omega_i (\hat{z}_i - z_i) \end{bmatrix} - \begin{bmatrix} G_{1i} \\ G_{2i} \end{bmatrix} (\hat{x}_i - x_i) \\ &= \begin{bmatrix} -G_{1i} & D_i H_i \\ -G_{2i} & \Omega_i \end{bmatrix} \begin{bmatrix} x_i - \hat{x}_i \\ \hat{z}_i - z_i \end{bmatrix} \end{aligned} \quad (4.22)$$

which can be rewritten as:

$$\dot{e}_{iobs} = \Omega_{icl} e_{iobs} \quad (4.23)$$

where

$$\Omega_{icl} = \begin{bmatrix} -G_{1i} & D_i H_i \\ -G_{2i} & \Omega_i \end{bmatrix} \quad (4.24)$$

According to equation (4.24), the disturbance observer has the potential to attain asymptotic stability by selecting the observer gains G_{1i} and G_{2i} such that the 8×8 matrix Ω_{icl} is Hurwitz. As before the precise selection of G_{1i} and G_{2i} is chosen in order to guarantee that the matrix Ω_{icl} contains eight eigenvalues characterized by negative real parts.

During transient periods, the control input u_i , provided by the controller, may not correspond to the actual control input applied to the system. The disparity between the real control input and the one produced by the controller may only arise during transient periods as a result of potential control input saturation. The observer design should consider the saturation of control input during transients by using a straightforward saturation function. Therefore, the above-mentioned observer can be modified by substituting the control input u_i with the saturation function $\text{sat}(u_i)$ in equation (4.20), resulting in

$$\begin{aligned}\dot{\hat{x}}_i &= A_i x_i + B_i \text{sat}(u_i) + F_i + D_i \hat{b}_i + G_{1i} (y_i - \hat{y}_i) \\ \dot{\hat{z}}_i &= \Omega_i z_i + G_{2i} (y_i - \hat{y}_i)\end{aligned}\quad (4.25)$$

where $\hat{x}_i(0) = 0$ and $\hat{z}_i(0) = 0$. The previous disturbance observer can be further simplified by substituting the control law u_i by its expression (4.8) resulting in

$$\begin{aligned}\dot{\hat{x}}_i &= (K_i e_i + \dot{y}_{iref}) + G_{1i} (y_i - \hat{y}_i) - B_i \Delta u_i \\ \dot{\hat{z}}_i &= \Omega_i \hat{z}_i + G_{2i} (y_i - \hat{y}_i) \\ \hat{b}_i &= H_i \hat{z}_i\end{aligned}\quad (4.26)$$

where

$$\Delta u_i = u_i - \text{sat}(u_i) \quad (4.27)$$

The above observer can be simplified to make it more suitable for real-time implementation by introducing a new state variable η such that $\eta = \hat{x}_i - y_{iref}$. Therefore, the final observer can take the form of:

$$\begin{aligned}\dot{\eta} &= -G_{1i} \eta + (K_i - G_{1i}) e_i - B_i \Delta u_i \\ \dot{\hat{z}}_i &= -G_{2i} \eta + \Omega_i \hat{z}_i - G_{2i} e_i \\ \hat{b}_i &= H_i \hat{z}_i\end{aligned}\quad (4.28)$$

where

$$\begin{aligned}\eta(0) &= y_i(0) - y_{iref}(0) = -e_i(0) \\ \hat{z}_i(0) &= 0\end{aligned}\quad (4.29)$$

It is important to emphasize that the reduced observer (4.28) does not have \dot{y}_{iref} , thus resolving the problem of amplification of measurement noises. Moreover, the inclusion of \dot{y}_{iref} in the feedback controller may result in the same problem. Hence, the term \dot{y}_{iref} can be omitted during the real-time implementation of the feedback controller.,(4.8) as the observer can compensate for it, resulting in

$$u_i = B_i^{-1} \left(K_i e_i - A_i x_i - F_i - D_i \hat{b}_i \right) \quad (4.30)$$

4.2 DC-Link Control under Balanced Grid Voltages

4.2.1 Feedback Controller

As in the previous chapter, during balanced grid voltages, GSC is deployed to regulate the dc-link voltage through the use of a cascade control scheme consisting of two loops: an inner loop and an outer loop. The outer loop assumes the role of regulating the dc-link voltage and the inner loop takes charge of controlling the dq -axis current components. In such a control scheme, the outer loop provides the command value (i_{dref}) for the d -axis current component, while the command value for the q -axis current component can be set to zero to ensure unity power factor operation. The inner loop is realized with the above-mentioned current controller. It remains to design the outer loop for regulating the dc-link voltage. Towards this end, recall that the differential equation governing the dynamics of the dc-link voltage is given by:

$$\frac{dv_{dc}}{dt} = \frac{i_{dc}}{C} - \frac{P}{Cv_{dc}} \quad (4.31)$$

The power delivered to the grid with the assumption that $v_q = 0$ can be represented as

$$P = \frac{3}{2} v_d i_d \quad (4.32)$$

By substituting (4.32) into (4.31), the differential equation becomes

$$\frac{dv_{dc}}{dt} = \frac{i_{dc}}{C} - \frac{3v_d i_d}{2Cv_{dc}} \quad (4.33)$$

Now, by setting $v_{dc} = x_v$ and $i_{dc} = b_{vd}$ and treating i_d as the control input u_{vd} , equation (4.33) can be expressed in state space model as

$$\dot{x}_v = A_{vd} x_v + B_{vd}(x_v) i_d + D_{vd} b_{vd} \quad (4.34)$$

where

$$A_{vd} = 0, \quad B_{vd}(x_v) = -\frac{3v_d}{2Cv_{dc}}, \quad D_{vd} = \frac{1}{C} \quad (4.35)$$

It is important to note that the dc-link voltage converges to a constant steady-state value. Therefore, one can assume that the disturbance b_{vd} has the same dynamics as that of v_{dc} , at least in the steady-state, yielding $\dot{b}_{vd} = 0$. Similar approach as in the previous chapter can be used to construct a composite controller for the dc-link voltage regulation, that is:

$$i_{dref} = \frac{-2v_{dc}C}{3v_d} \left(k_{iv}e_v + \frac{dv_{dcref}}{dt} - \frac{b_{vd}}{C} \right) \quad (4.36)$$

where $e_v = v_{dcref} - v_{dc}$ is the tracking error, and k_{iv} is the control gain. As mentioned before the composite controller can be made asymptotically stable by choosing $k_{iv} > 0$. It can also be shown that fast transient response can be achieved by selecting the gains k_{iv} as large as possible. However, it is not trivial to measure the disturbance b_{vd} because of model uncertainties. To address this issue, the above controller can be implemented as

$$i_{dref} = \frac{-2v_{dc}C}{3v_d} \left(k_{iv}e_v + \frac{dv_{dcref}}{dt} - \frac{\hat{b}_{vd}}{C} \right) \quad (4.37)$$

4.2.2 Disturbance Observer

As before, the estimation of the disturbance \hat{b}_{vd} can be achieved through a reduced order disturbance observer as

$$\begin{aligned} \dot{\hat{b}}_{vd} &= G_{vd} \left(\dot{x}_v - A_{vd}x_v - B_{vv}(x_v)i_{dref} - D_{vd}\hat{b}_{vd} \right) \\ &= -G_{vd} \frac{1}{C} \hat{b}_{vd} + G_{vd} \left(\frac{dv_{dc}}{dt} + \frac{3v_d i_{dref}}{2v_{dc}C} \right) \end{aligned} \quad (4.38)$$

where G_{vd} is the observer gain which should be selected to satisfy the stability condition of the disturbance observer. In particular, the observer gain G_{vd} can be selected considering the

stability of the estimation error $e_{obsd} = \hat{b}_{vd} - b_{vd}$. By assuming $\dot{b}_{vd} = 0$ and proceeding as in the previous chapter, the composite controller can be simplified as

$$\begin{aligned}\dot{\hat{z}}_{vd} &= -G_{vd}k_{iv}e_v - G_{vd}\frac{3v_d}{2Cv_{dc}}\Delta i_{dref} \\ \hat{b}_{vd} &= \hat{z}_{vd} - G_{vd}e_v\end{aligned}\tag{4.39}$$

where Δi_{dref} is given by:

$$\Delta i_{dref} = i_{dref} - sat(i_{dref})\tag{4.40}$$

4.3 Phase-Locked Loop (PLL)

To perform dq transformation, the current control approach necessitates extracting the grid voltage-phase angle θ in the dq reference frame. When the grid is balanced, it is easy to estimate the angle θ since there is no negative sequence voltage component. When faced with such a situation, utilizing an SRF-PLL method with a wide bandwidth can swiftly and precisely detect the angle θ , as in [86]. However, under unbalanced grid condition a reduction of SRF-PLL bandwidth is needed to reject and cancel out the effect of the harmonics from the distorted voltage which is undesirable. Hence, a Decoupled Double Synchronous Reference Frame Phase-Locked Loop (DDSRF-PLL) is implemented as in [87]. This technique defines an unbalanced voltage vector, consisting of both positive- and negative-sequence components, and expresses it on a dual synchronous reference frame voltage characterization dq^m and dq^n respectively, the estimation of the angle can be done by using a DSRF-PLL, then a Decoupling Network (DN) is implemented along with a Low Pass Filter (LPF) for both dq^m and dq^n which results in a fast, precise, and robust positive-sequence voltage detection even under unbalanced and distorted grid conditions.

4.4 Current Control of the Machine-Side Converter

This part is concerned with the development of a current controller to regulate the current flowing through the stator winding of the PMSG under both balanced and unbalanced grid voltages using dq coordinates.

4.4.1 Perturbed Model and Feedback Controller

The model of PMSG in dq reference frame is given by (2.59) [74]

$$\frac{d}{dt} \begin{bmatrix} i_{ds} \\ i_{qs} \end{bmatrix} = \begin{bmatrix} -\frac{R_s}{L_{ds}} & \frac{L_{qs}}{L_{ds}} \omega_e \\ -\frac{L_{qs}}{L_{qs}} \omega_e & -\frac{R_s}{L_{qs}} \end{bmatrix} \begin{bmatrix} i_{ds} \\ i_{qs} \end{bmatrix} + \begin{bmatrix} \frac{1}{L_{ds}} & 0 \\ 0 & \frac{1}{L_{qs}} \end{bmatrix} \begin{bmatrix} u_{ds} \\ u_{qs} \end{bmatrix} + \begin{bmatrix} 0 \\ -\frac{\psi_r \omega_e}{L_{qs}} \end{bmatrix} \quad (4.41)$$

By considering model uncertainties (b_{md}), the above model can be rewritten in a compact form as

$$\dot{x}_m = A_m x_m + B_m u_m + F_m + D_m b_m \quad (4.42)$$

where

$$A_m = \begin{bmatrix} -\frac{R_s}{L_{ds}} & \frac{L_{qs}}{L_{ds}} \omega_e \\ -\frac{L_{qs}}{L_{qs}} \omega_e & -\frac{R_s}{L_{qs}} \end{bmatrix}, \quad B_m = D_m = \begin{bmatrix} \frac{1}{L_{ds}} & 0 \\ 0 & \frac{1}{L_{qs}} \end{bmatrix}, \quad F_m = \begin{bmatrix} 0 \\ -\frac{\psi_r \omega_e}{L_{qs}} \end{bmatrix} \quad (4.43)$$

and

$$u_m = \begin{bmatrix} u_{ds} \\ u_{qs} \end{bmatrix}, \quad x_m = \begin{bmatrix} i_{ds} \\ i_{qs} \end{bmatrix} \quad (4.44)$$

According to [80], one can design of a state-feedback controller for PMSG as

$$u_m = B_m^{-1} (K_m e_m + \dot{y}_{mref} - A_m x_m - F_m - D_m b_m) \quad (4.45)$$

where

$$y_{mref} = \begin{bmatrix} i_{dsref} \\ i_{qsref} \end{bmatrix}, \quad e_m = \begin{bmatrix} i_{dsref} - i_{ds} \\ i_{qsref} - i_{qs} \end{bmatrix}, \quad K_m = \begin{bmatrix} K_{md} & 0 \\ 0 & K_{mq} \end{bmatrix} \quad (4.46)$$

where i_{dsref} and i_{qsref} are the command values for the d -axis and q -axis current. As before, the stability of the closed-loop system can be investigated by studying the closed-loop error dynamics. This can be achieved by substituting (4.45) into (4.42). When it does so, it can be shown that the dynamics of the closed-loop system is well defined by a first-order system with a time constant of $1/k_{md}$. Hence, the larger k_{md} , the faster the system's response. The suggested feedback controller might not be feasible for practical implementation due to the challenge of measuring the disturbance b_m . To address this limitation, a potential solution involves replacing the real disturbance b_m with its estimated counterpart \hat{b}_m under the condition that a suitable estimator capable of generating \hat{b}_m is available. Consequently, the modified controller can be represented as follows:

$$u_m = B_m^{-1} \left(K_m e_m + \dot{y}_{mref} - A_m x_m - F_m - D_m \hat{b}_m \right) \quad (4.47)$$

4.4.2 Disturbance Observer

As stated earlier, it is necessary to estimate the disturbance in order to apply the feedback controller. Therefore, it is necessary to utilize a disturbance observer that is capable of accurately estimating sinusoidal disturbances. Indeed, regardless of whether the grid voltages are balanced or unbalanced, the dq -axis components of the stator currents are assumed to have constant steady-state values, therefore, one can assume that:

$$\dot{b}_m = 0 \quad (4.48)$$

Following [81], and proceeding as in the previous sections, the simplified disturbance observer to estimate b_m can be expressed as

$$\begin{aligned}\dot{\eta}_m &= -G_{1m}\eta_m + (K_m - G_{1m})e_m - B_m\Delta u_m \\ \dot{\hat{b}}_m &= -G_{2m}\eta_m - G_{2m}e_m\end{aligned}\quad (4.49)$$

where G_{1m} and G_{2m} are the observer gains; they can be selected to correspond to the stability of the disturbance observer. As before, the stability of the observer can be investigated by analyzing the dynamics of the estimation error e_{mobs} . Toward this end, it can be shown that:

$$\dot{e}_{mobs} = \begin{bmatrix} -G_{1m} & D_m \\ -G_{2m} & 0 \end{bmatrix} e_{mobs} = \Omega_{clm} e_{mobs} \quad (4.50)$$

which can be written as

$$\dot{e}_{mobs} = \Omega_{clm} e_{mobs} \quad (4.51)$$

where

$$\Omega_{clm} = \begin{bmatrix} -G_{1m} & D_m \\ -G_{2m} & 0 \end{bmatrix} \quad (4.52)$$

following the same technique as in previous sections. The observer gains G_{1m} and G_{2m} can be selected such that the matrix is Ω_{clm} Hurwitz. To simplify the observer design, one can use the pole placement technique to select the observer gains that can assign the eigenvalues of Ω_{clm} in the desired locations in the open left-half complex.

Remark 1: The control of dc-link voltage under unbalance case is achieved by MSC, which is exactly the same as in chapter 3 except that in this chapter the control is taking place in dq reference frame. Hence, the composite controller derived in (3.119) is used in this chapter given by

$$\begin{aligned}\dot{\hat{z}}_{vu} &= -G_{vu}k_{vu}e_v - G_{vu}\frac{3p\psi_r\omega_r}{2v_{dc}C}\Delta i_{qsref} \\ \hat{b}_{vu} &= \hat{z}_{vu} - G_{vu}e_v\end{aligned}\quad (4.53)$$

and

$$i_{qsref} = -\frac{2v_{dc}C}{3p\psi_r\omega_r} \left(k_{vu}e_v + \dot{v}_{dcref} - \frac{1}{C}\hat{b}_{vu} \right) \quad (4.54)$$

Remark 2: As mentioned before, under balanced grid voltage condition MSC is responsible for extracting the maximum power available from the wind using MPPT Algorithm. Toward this end and as in the previous chapter, the machine current reference i_{qsref} is calculated for the controller of PMSG as in equation (3.112), where the d-axis current is set to zero $i_{dsref} = 0$ and i_{qsref} is

$$i_{qsref} = \frac{2}{3p\psi_r} K_{opt}\omega_{r-opt}^2 \quad (4.55)$$

4.5 current Reference Calculation During Unbalanced Grid Voltages

In the balanced grid condition, the d -axis current reference is generated by an outer voltage loop to regulate the dc link voltage, while the q -axis current reference is set to zero. However, under unbalanced grid voltages, the MSC assumes the role of controlling the dc-link voltage so that the GSC only takes charge of injecting constant active power to the grid by adjusting the grid currents to align with the designated sinusoidal current references. Following [88], the positive-negative dq -axis current references that can make the active power constant are given by

$$\begin{bmatrix} i_{dref}^+ \\ i_{qref}^+ \\ i_{dref}^- \\ i_{qref}^- \end{bmatrix} = \begin{bmatrix} v_d^+ & v_q^+ & v_d^- & v_q^- \\ v_q^+ & -v_d^+ & v_q^- & -v_d^- \\ v_d^- & v_q^- & v_d^+ & v_q^+ \\ v_q^- & -v_d^- & -v_q^+ & v_d^+ \end{bmatrix}^{-1} \times \frac{2}{3} \begin{bmatrix} P_{ref0} \\ 0 \\ 0 \\ 0 \end{bmatrix} \quad (4.56)$$

Finally, dq -axis currents that can satisfy constant active power are then given by:

$$\begin{aligned} i_{dref}^{FRT} &= i_{dref}^+ + i_{dref}^- \\ i_{qref}^{FRT} &= i_{qref}^+ + i_{qref}^- \end{aligned} \quad (4.57)$$

Table 8: Grid parameters

System Parameters	Symbol	Value
Line Resistance	R	$1\text{ m}\Omega$
Line Inductance	L	10 mH
Line-neutral Voltage	v	208 V
DC-Link Voltage	v_{dc}	300 V
DC-Link Capacitor	C	$1\text{ }\mu\text{F}$
Grid Voltage Frequency	ω	50 Hz
Sampling Frequency	f_s	10 KHz
Switching Frequency	f_{sw}	5 KHz
Sampling Time for the simulator	T_s	$1\text{ }\mu\text{S}$

Table 9: PMSG parameters

Machine Parameters	Symbol	Value
Stator Phase Resistance	R_s	$840\text{ m}\Omega$
d -axis inductor	L_{ds}	12.6 mH
q -axis inductor	L_{qs}	21.8 mH
Angular velocity of the rotor	ω_r	200 r/min
flux of the rotor	ψ_r	0.607 Wb
Number of pole pairs	P	11
The air density	ρ	1.225 kg/m^3
The radius of the blade	R_b	1.2m
The optimum rotor tip speed ratio	λ_{opt}	6.36
The optimum efficiency	C_{Pmax}	0.4382

Table 10: Grid controller parameters

Control Parameters	Symbol	Value
Inner Loop Control Gain	k_i	1000
Outer Loop Control Gain	k_{iv}	150
Damping Ratio	ζ	0.707
Natural Pulsation 1	ω_{n1}	800 rad/s
Natural Pulsation 2	ω_{n2}	1000 rad/s
Real eigenvalue 1 and 2	$\lambda_{1,2}$	$\zeta\omega_{n1} \pm j\omega_{n1}\sqrt{1-\zeta^2}$
Real eigenvalue 3 and 4	$\lambda_{3,4}$	$\zeta\omega_{n2} \pm j\omega_{n2}\sqrt{1-\zeta^2}$

Table 11: PMSG grid controller parameters

Control Parameters	Symbol	Value
Inner Loop Control Gain	k_{md}	1000
Outer Loop Control Gain	k_{vu}	150
Damping Ratio	ζ	0.707
Natural Pulsation 1	ω_{n1}	800 rad/s
Natural Pulsation 2	ω_{n2}	1000 rad/s
Real eigenvalue 1 and 2	$\lambda_{1,2}$	$\zeta\omega_{n1} \pm j\omega_{n1}\sqrt{1-\zeta^2}$
Real eigenvalue 3 and 4	$\lambda_{3,4}$	$\zeta\omega_{n2} \pm j\omega_{n2}\sqrt{1-\zeta^2}$

4.6.1 Performance Evaluation under Balanced Grid

The first simulation experiment was conducted during balanced grid voltages, the grid voltages v_{abc} , the three-phase currents i_{abc} , the grid dq -axis currents $I_{d,q}$ and their references I_{dref} and I_{qref} the actual active and reactive powers P and Q are presented in Figure 27, while The dc-link voltage v_{dc} , the machine Torque T the machine current in synchronous frame i_{sd}

and i_{sq} and the reference of machine current i_{sdref} and i_{sqref} and the machine currents i_{sabc} are shown in Figure 28. The results obtained indicate that the controller in the grid side that was designed successfully maintained the dc-link voltage at its designated setpoint of 370 V. The reason for this outcome is because the suggested controller effectively managed the PWM rectifier, ensuring that the grid dq -axis currents precisely align with the specified command value derived from the outer dc voltage loop on the grid side. It is noteworthy that in balanced networks, the active and reactive powers do not exhibit oscillations, as anticipated. Nevertheless, it is worth noting that the machine currents consistently complied with the reference values given by the Maximum Power Point Tracking MPPT algorithm.

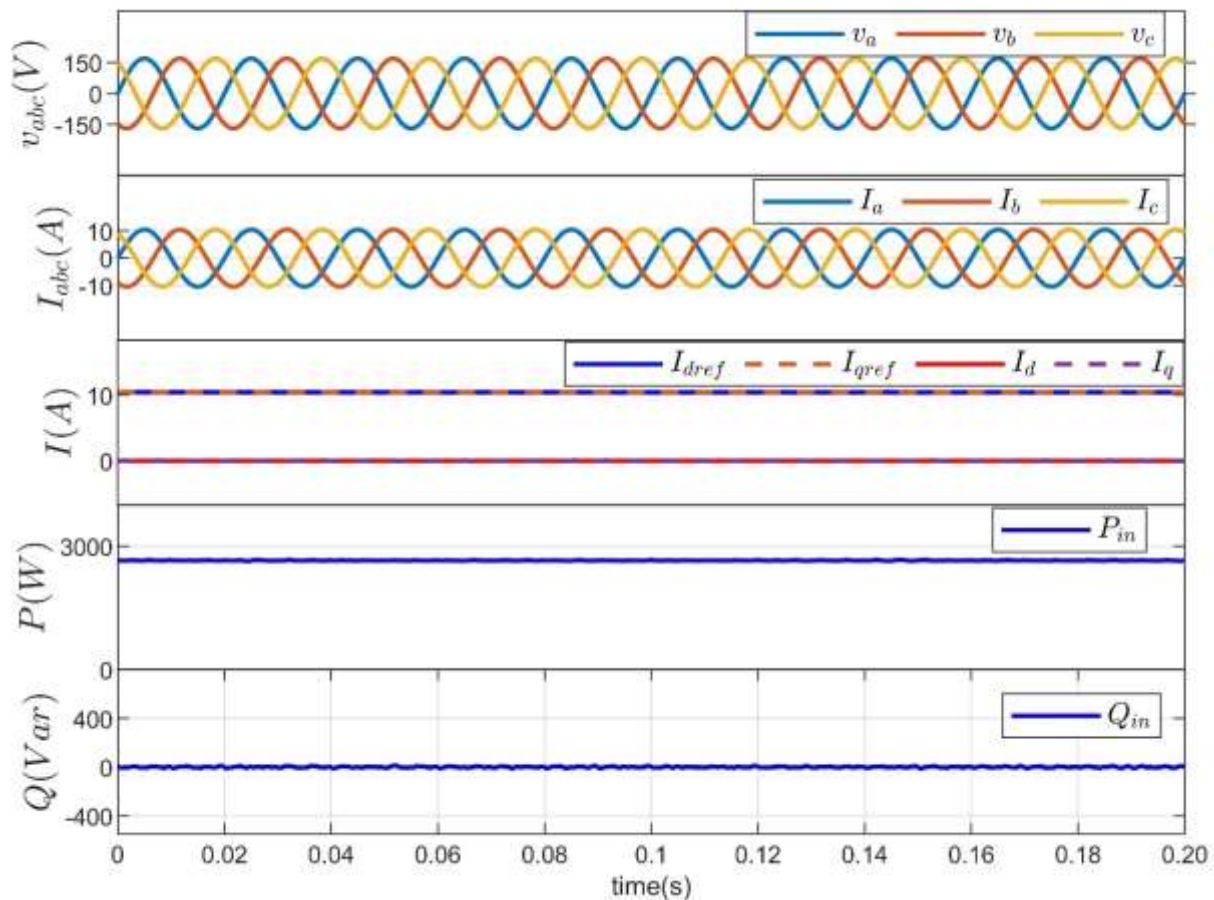


Figure 27: Grid simulation results under balanced grid voltages.

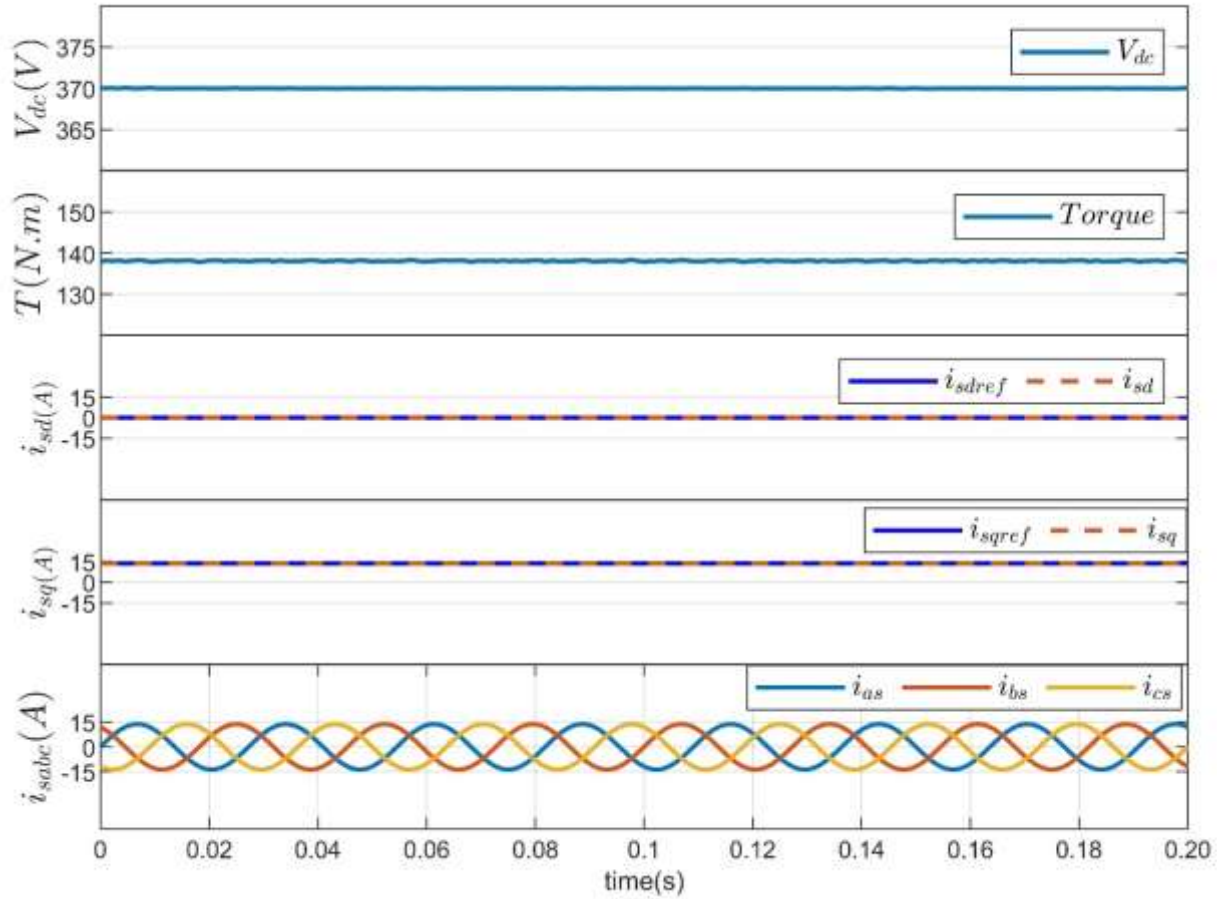


Figure 28:PMSG simulation results under balanced grid voltages.

4.6.2 Performance Evaluation under Unbalanced Grid Voltages without Notch Filter

This test is conducted with a 50% voltage dip at phase A and phase B, results show the proposed controller for GSC was able to ensure accurate control of d -axis component and q -axis component of the grid current even if their references exhibit sinusoidal behavior. Note that the oscillatory behavior of the current reference is due to the requirement of injecting constant active power to the grid under unbalanced voltages. The measured responses validated the composite controller's capability to reject both constant and sinusoidal disturbances at twice the fundamental frequency as shown in Figure 29. However, Figure 30 indicates that, when the grid voltage is imbalanced, the controller for the DC-link voltage was able to asymptotically regulate the DC-link voltage to match the desired value. where it is evident that the voltage imbalance resulted in the dc-link voltage including oscillation of

frequency 2ω , Which in turns results in noise in the machine torque. Finally, the machine side controller was able to regulate the machine dq -axis currents to their reference values calculate in the outer loop of dc link controller.

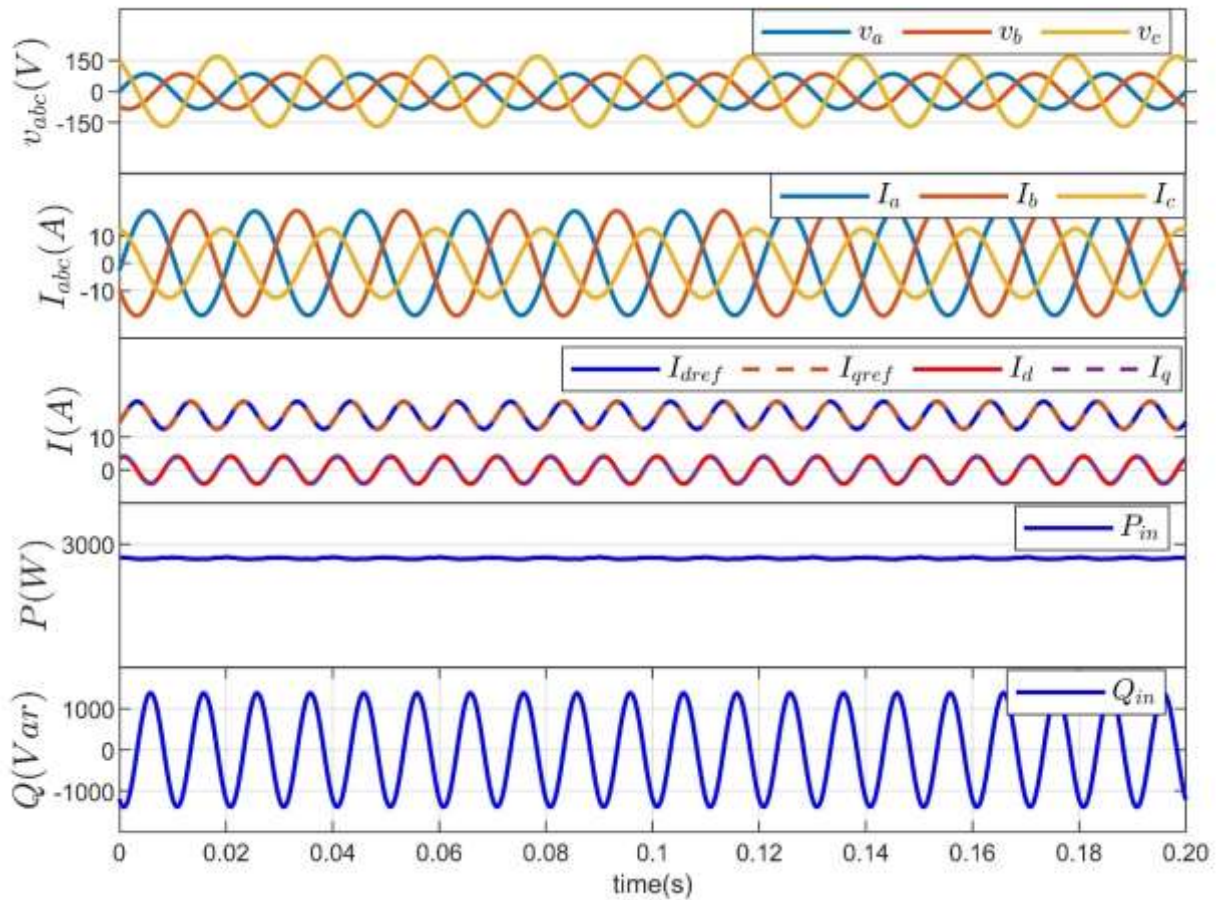


Figure 29: Grid simulation results under unbalanced grid voltages without notch filter.

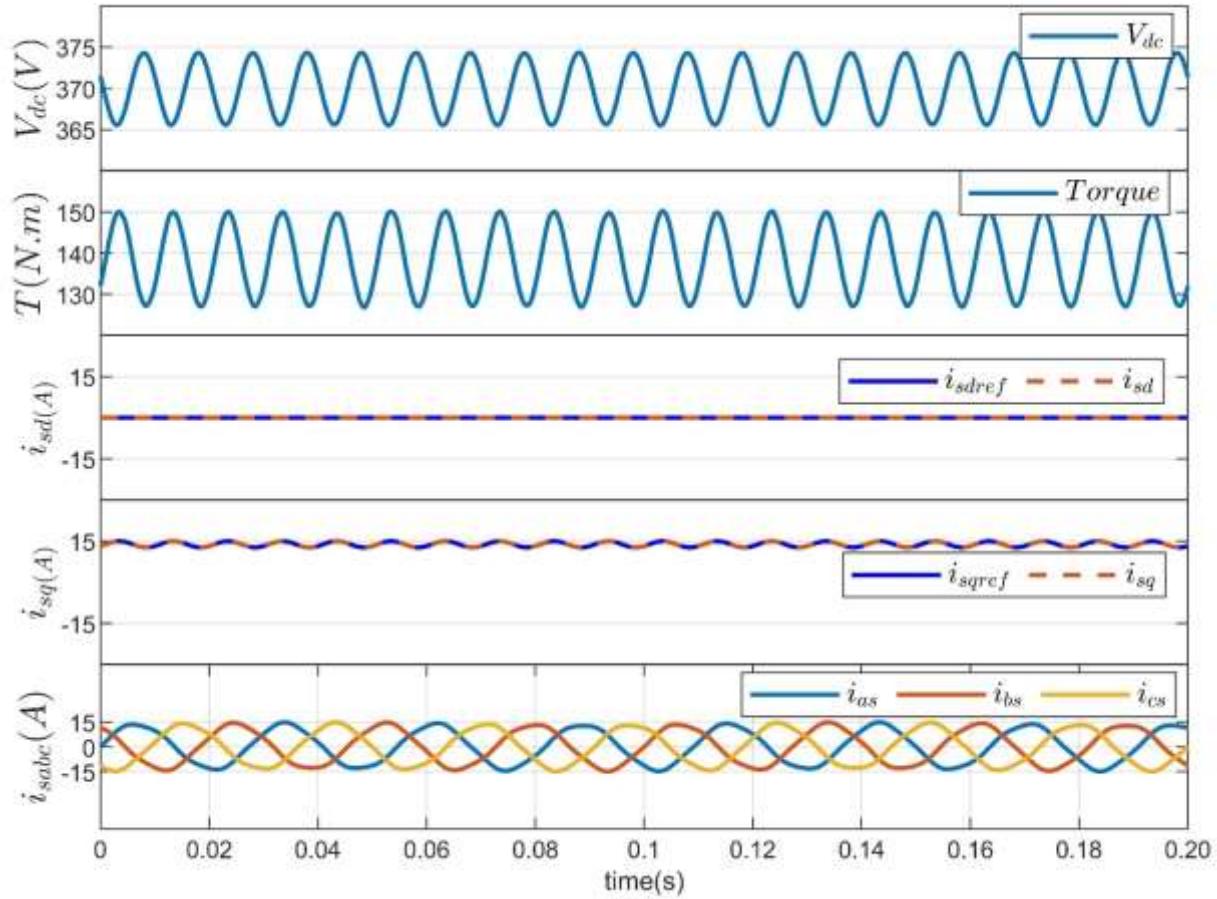


Figure 30: PMSG simulation results under unbalanced grid voltages without notch filter.

4.6.3 Performance Evaluation under Unbalanced Grid Voltages along with Notch Filter

This test is identical to the previous test, with the only difference being the addition of a notch filter to the dc-link voltage. Results show that the implementation of the filter reduces the noise in the dc-link voltage which in turns reduces the noise in the torque caused by the unbalanced in the grid voltage as shown in Figure 32.

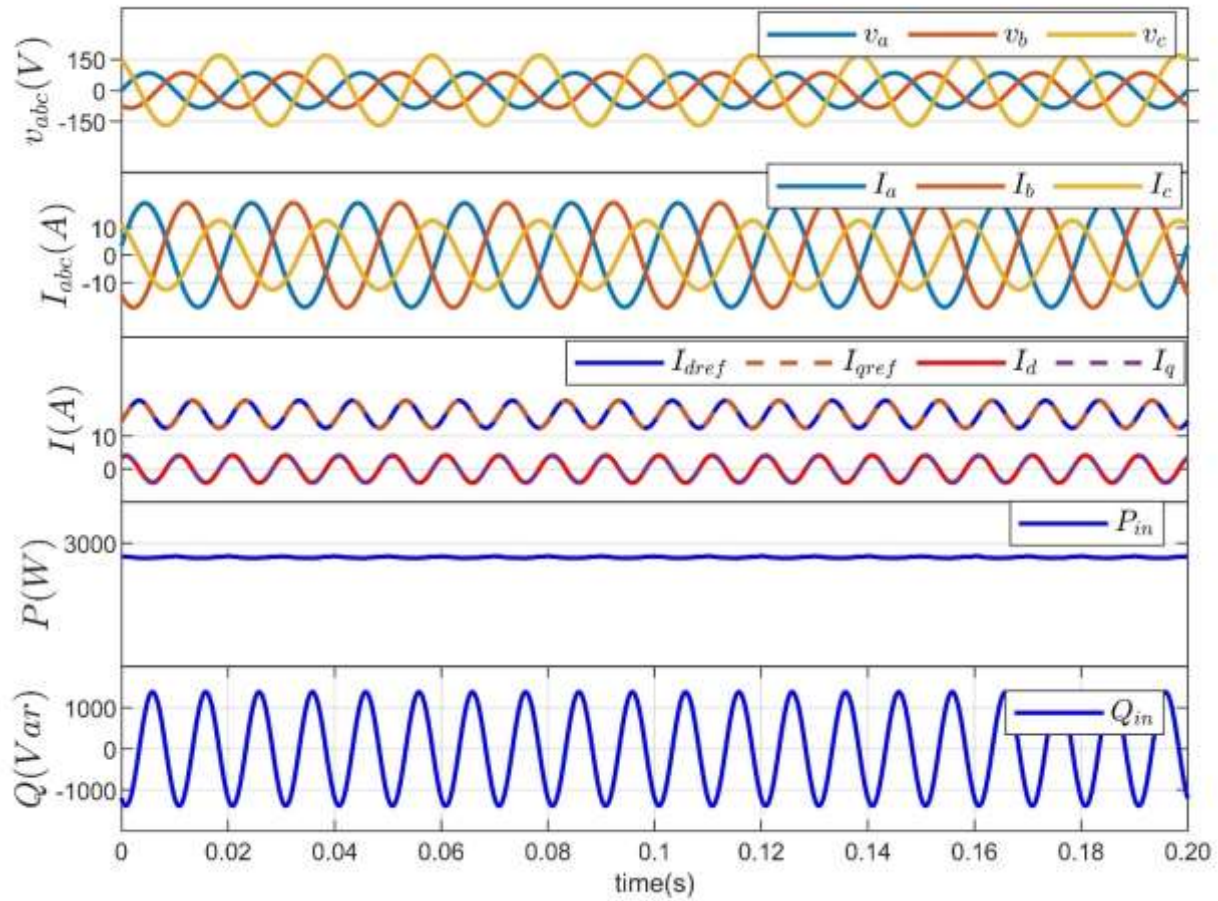


Figure 31: Grid simulation results during unbalanced grid voltages with notch filter.

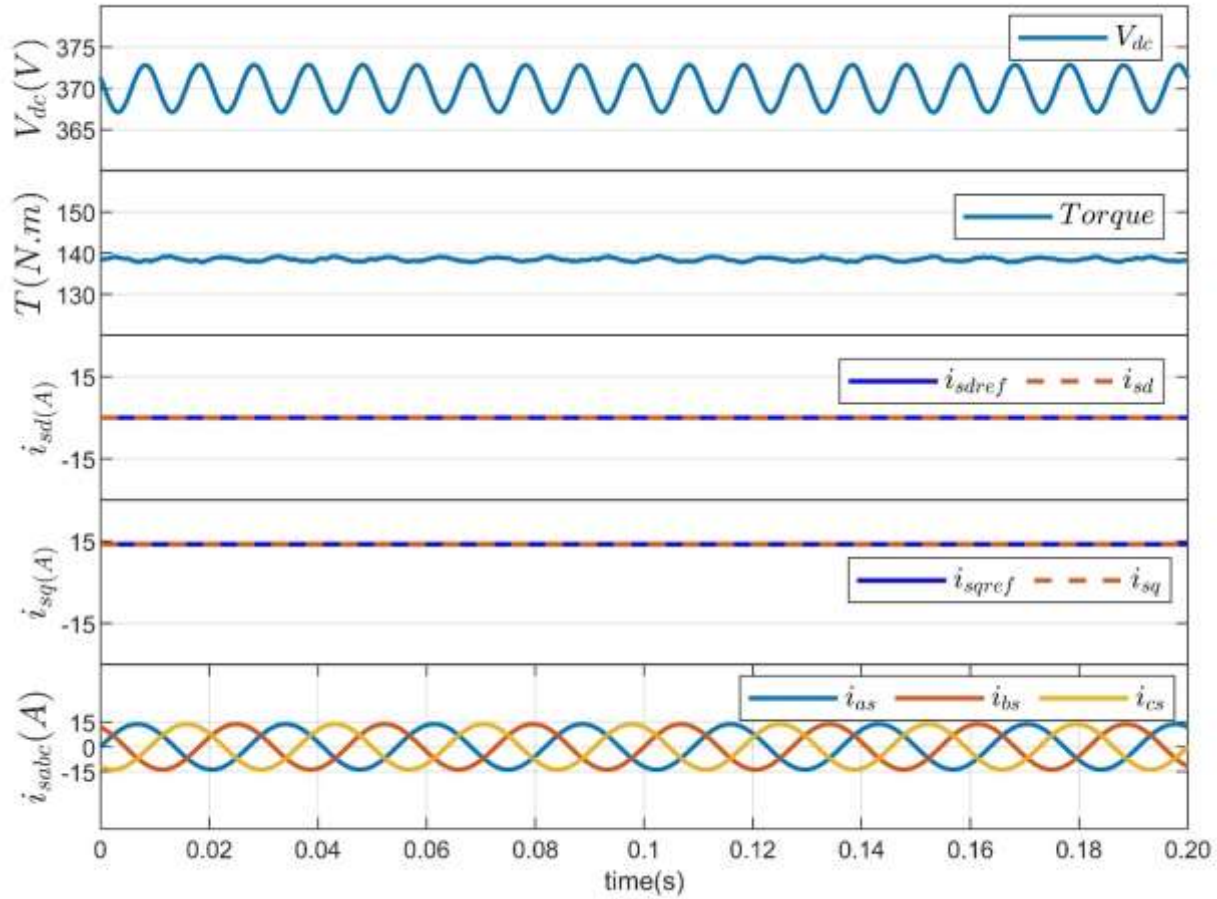


Figure 32: PMSG simulation results during unbalanced grid voltages with notch filter.

4.6.4 Performance Evaluation of the Disturbance Observer Effect and under Unbalanced Grid Voltages

4.6.4.1 Performance Evaluation of the Disturbance Observer in Grid Side

The objective of this study is to analyze the performance of the disturbance in the grid-side controller and examine the capability of the feedback controller in isolation. The test requires the elimination of the disturbance at $t=0.1$ seconds in grid side controller, while the disturbance in machine side is still operational. Figure 33 demonstrates that without the disturbance, the feedback controller alone is unable to guarantee that the grid dq -axis currents align with their respective references, which results in an oscillating active power injected to the grid at 2ω . This implies that the feedback controller alone is insufficient in mitigating the

effects of unknown disturbances caused by inaccuracies in the model and voltage imbalances. In the absence of any disturbance. However, the oscillating active power leads to a reduction in the ripples of the dc-link voltage, as seen in Figure 34.

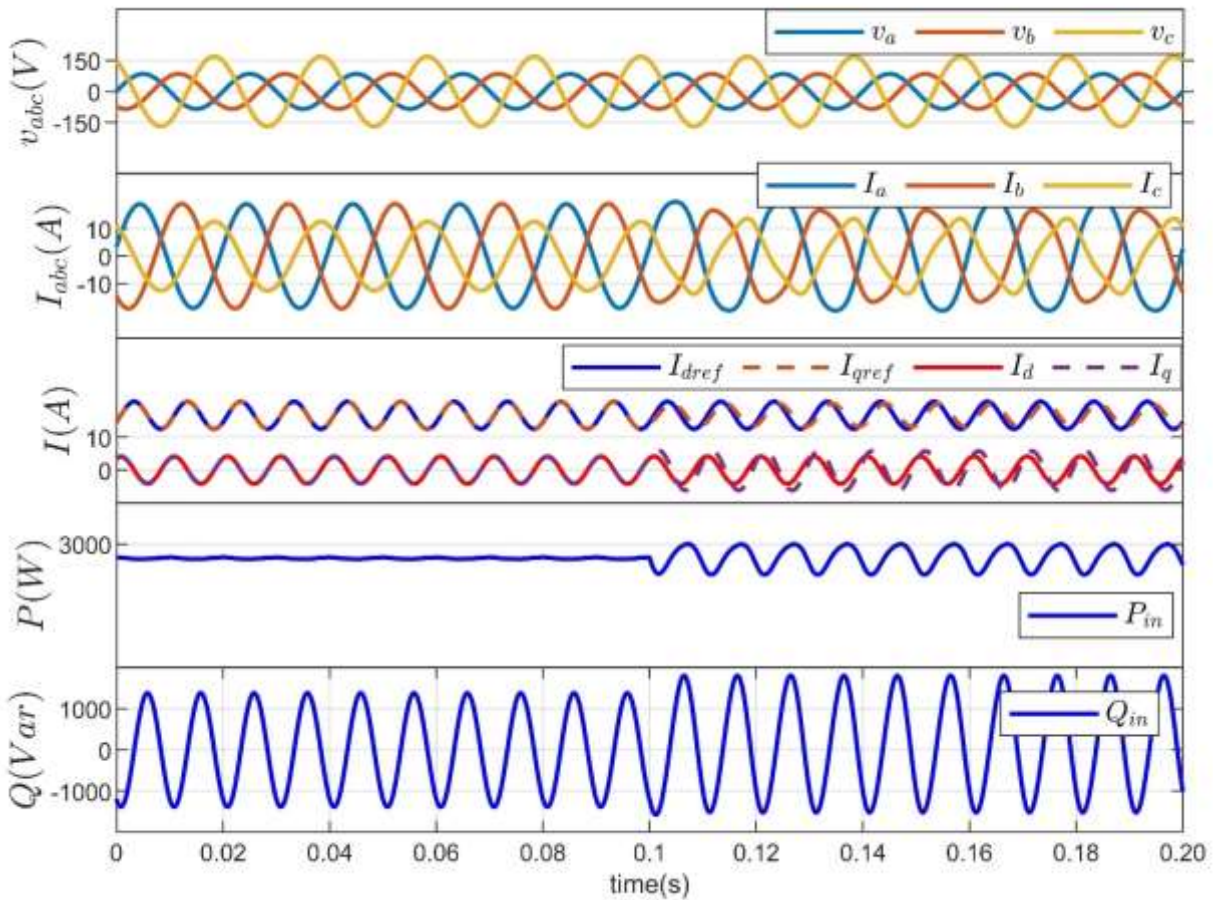


Figure 33: Grid simulation results when the disturbance observer was disabled at $t = 0.1$ s from the grid.

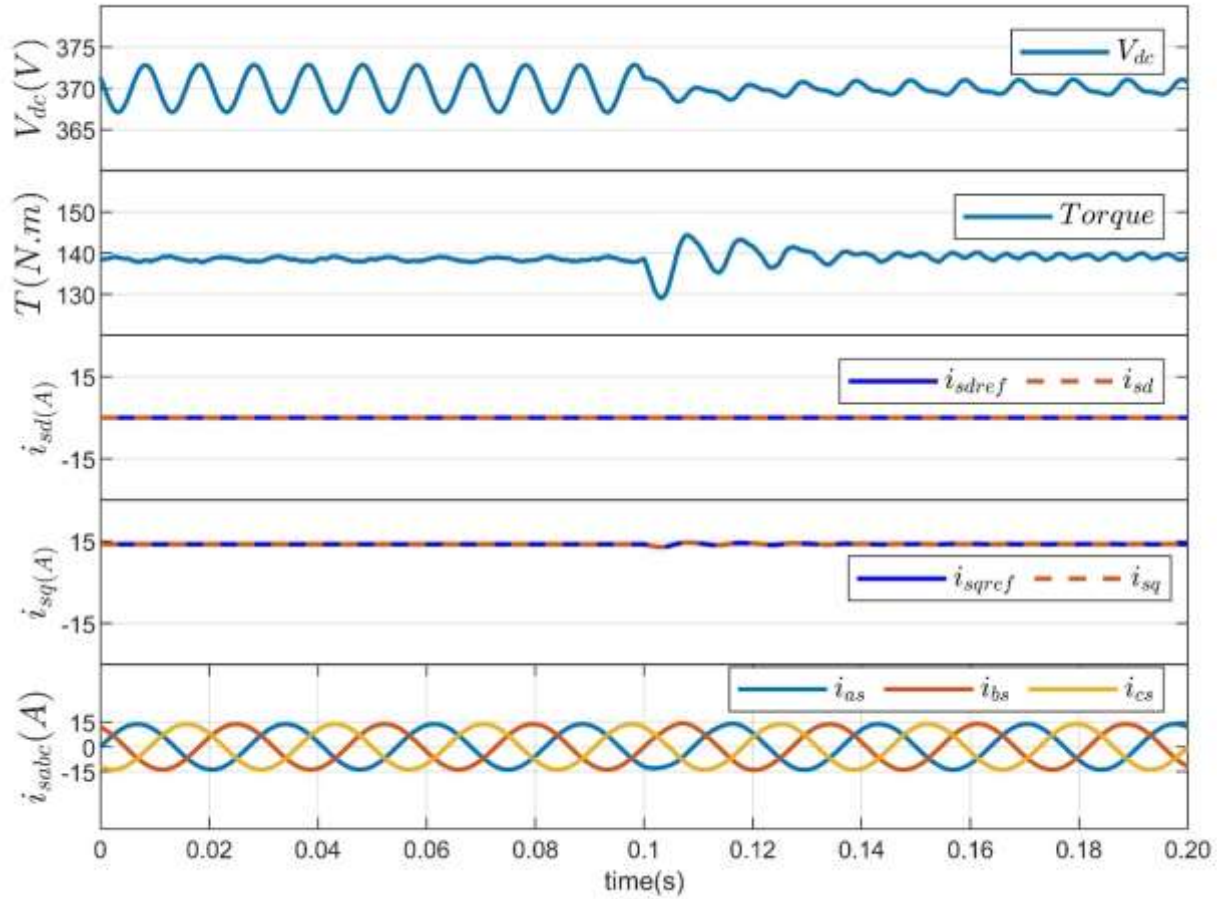


Figure 34: PMSG Simulation results when the disturbance observer was disabled at $t = 0.1$ s from the Grid.

4.6.4.2 Performance Evaluation of the Disturbance Observer in Machine Side

The aim of this study is to examine the performance of the disturbance in the controller on the machine side and assess the efficacy of the feedback controller in isolation. The simulation experiment involves removing the disruption at $t=0.1$ seconds from the machine side controller, while the disturbance in the grid side is still functioning. Figure 36 shows that the feedback controller alone without disturbance observer fails to accurately track the dq -axis machine currents to follow their references.

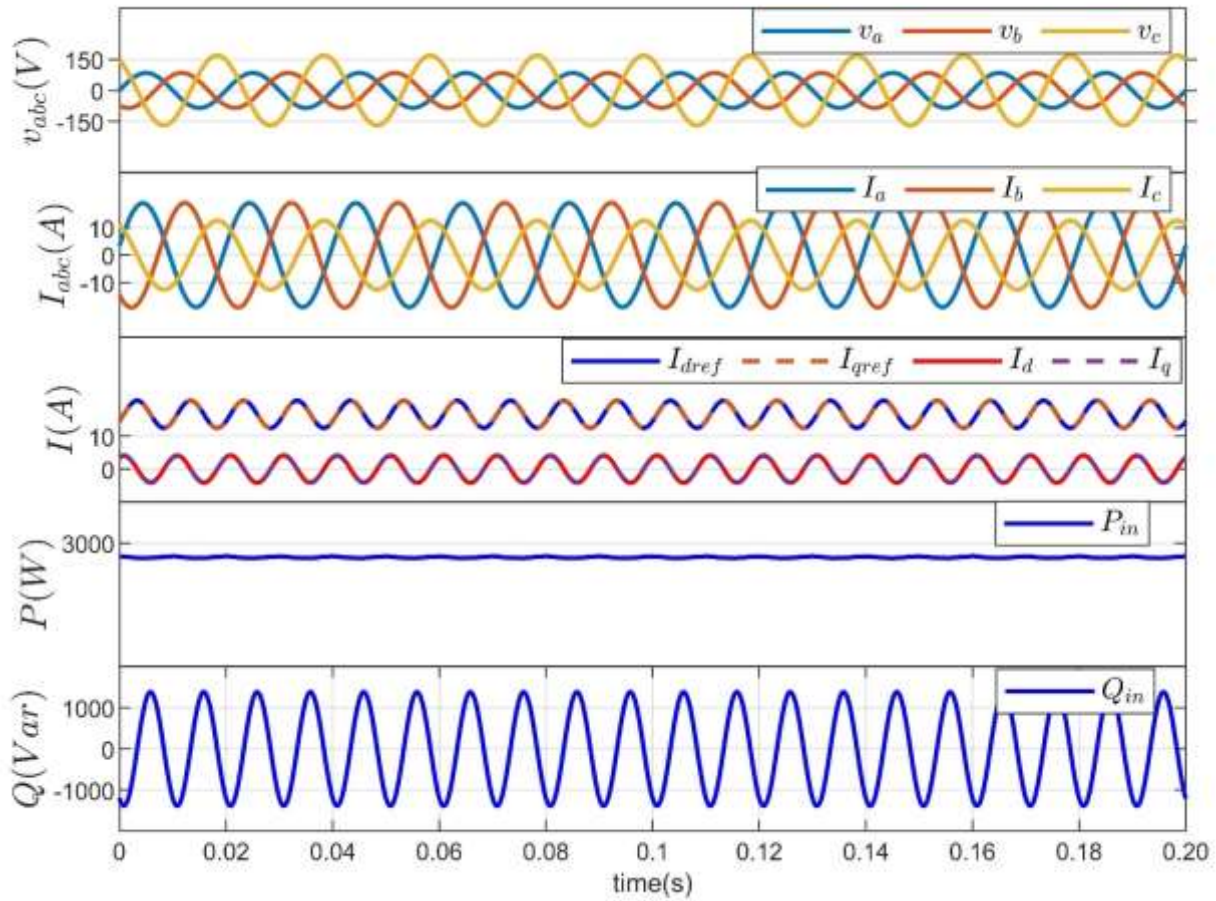


Figure 35: Grid Simulation results when the disturbance observer was disabled at $t = 0.1$ s from the machine.

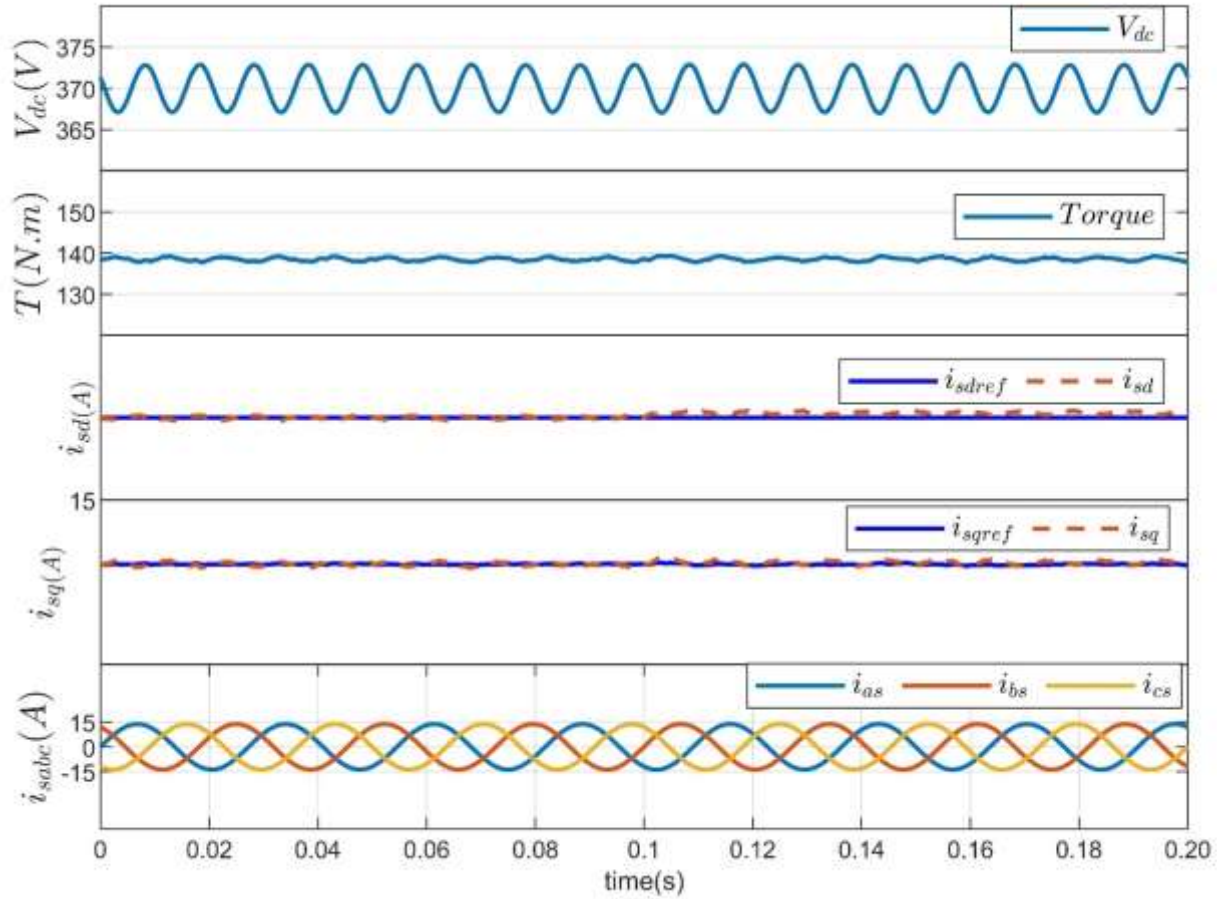


Figure 36: PMSG simulation results when the disturbance observer was disabled at $t = 0.1$ s from the machine.

4.6.5 Performance Evaluation under a Grid Condition Transition

The aim of this simulation experiment was to examine the dynamic response of the composite controller and evaluate how the control function transitions between the Machine Side Converter (MSC) and the Grid Side Converter (GSC) when the grid conditions change. Specifically, the focus was on the transition from a balanced grid to an unbalanced grid and then back to a balanced grid. At a time of 0.04 seconds, there is a drop in voltage of 50% in phase B, which is subsequently resolved at a time of 0.14 seconds. The simulation results are illustrated in Figure 37 and Figure 38. The acquired results demonstrated the efficient performance of the proposed controller in producing fast and seamless reconfiguration to an abrupt disturbance, as the initial value of the disturbance is always available. The presence of

voltage imbalance and subsequent fault clearance had almost no effect on the grid current, a little effect on the transient response of active power, as well as the dc-link voltage and associated torque. The simulation findings demonstrate that modifying the transition between grid balance and imbalance has no impact on the machine currents.

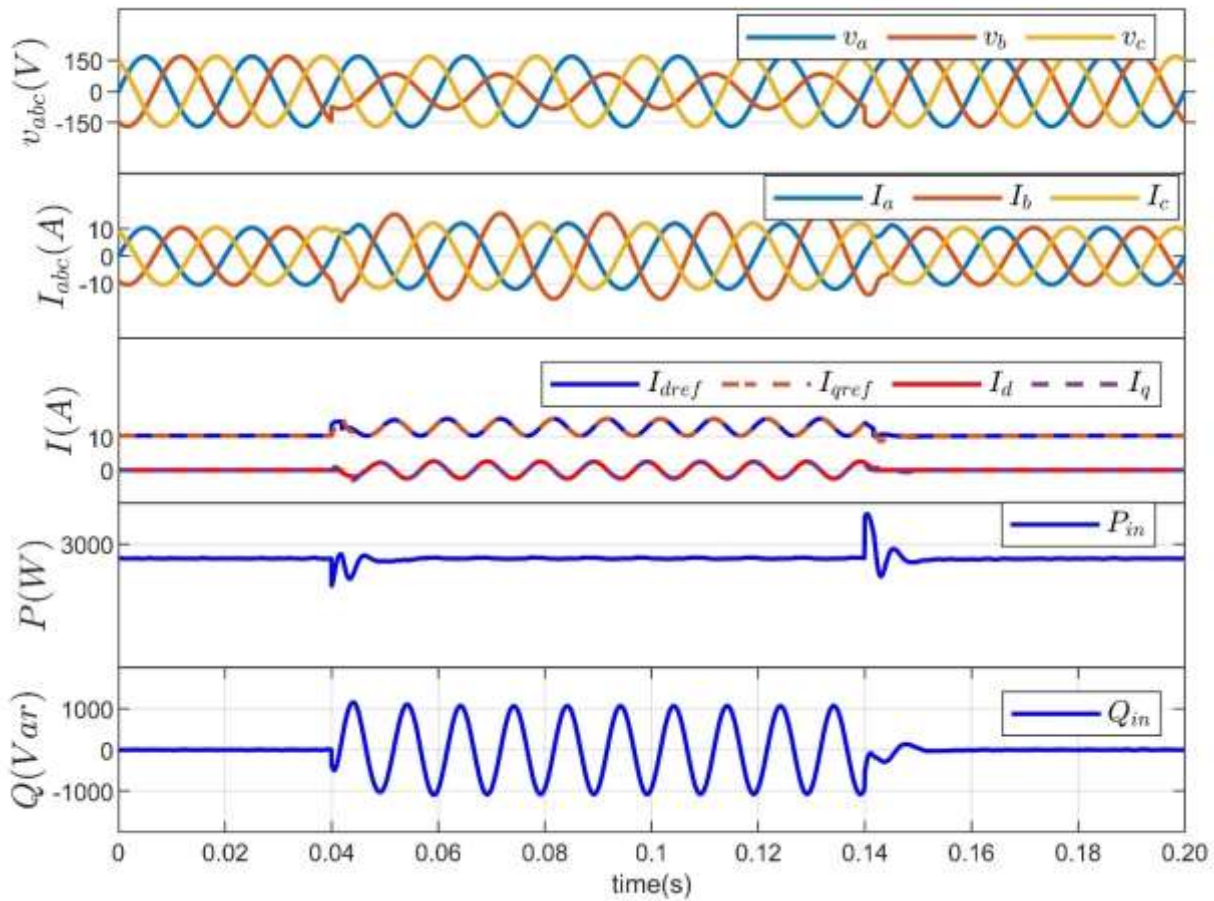


Figure 37: Grid simulation results when 50% dip in Phase B was suddenly created at $t = 0.04$ s to 0.14 s.

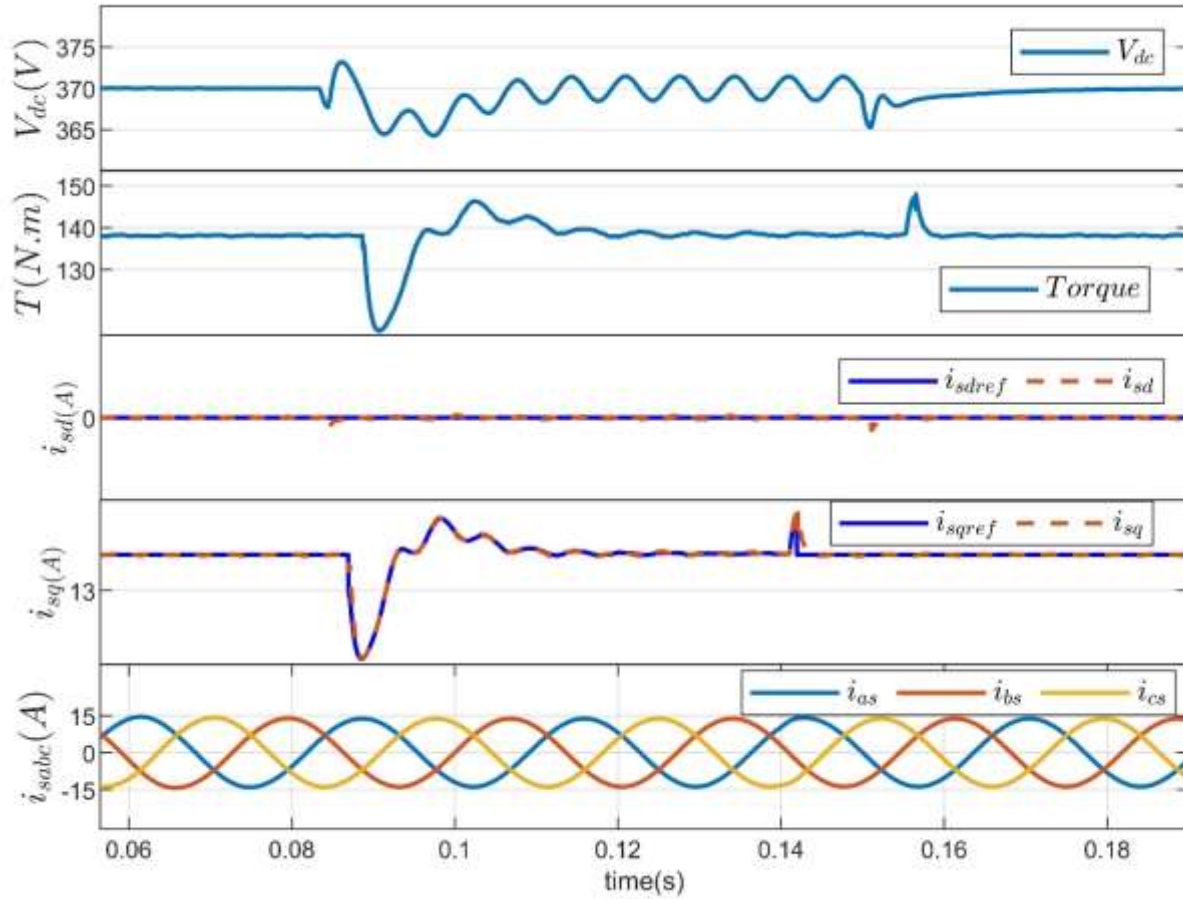


Figure 38: PMSG Simulation results when 50% dip in Phase B was suddenly created at $t = 0.04$ s to 0.14 s.

4.6.6 Performance Evaluation under Model Uncertainties and Unbalanced Grid Voltages

The objective of this simulation experiment was to evaluate the controller's resilience in the face of parameter variations. More precisely, the inductance and resistance values of the system were modified to 150% of their nominal values, the simulation was carried out under an unbalanced grid situation, and the results are shown in Figure 39 and Figure 40. The results show that changes in the variables L and R had no effect on the control performances, as the estimator accounted for the discrepancy between the real and nominal parameters. The efficacy of the composite controller was evidenced by the precise match between the real power and its intended reference value. This resulted in precise control of the active and reactive power, dc-link voltage, machine torque, and currents.

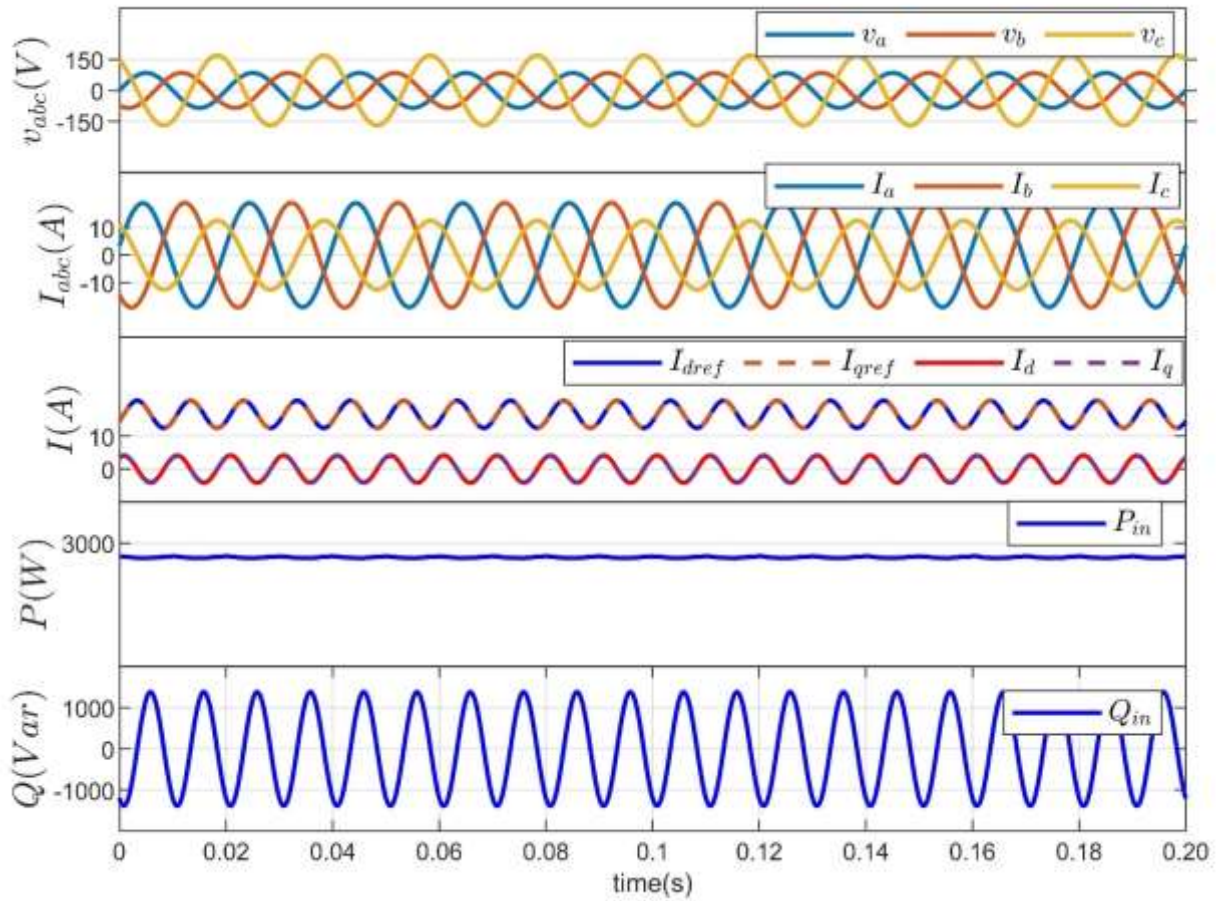


Figure 39: Grid simulated outcomes of the grid when the resistance R and inductance L utilized in the controller are increased by 150% of their nominal values.

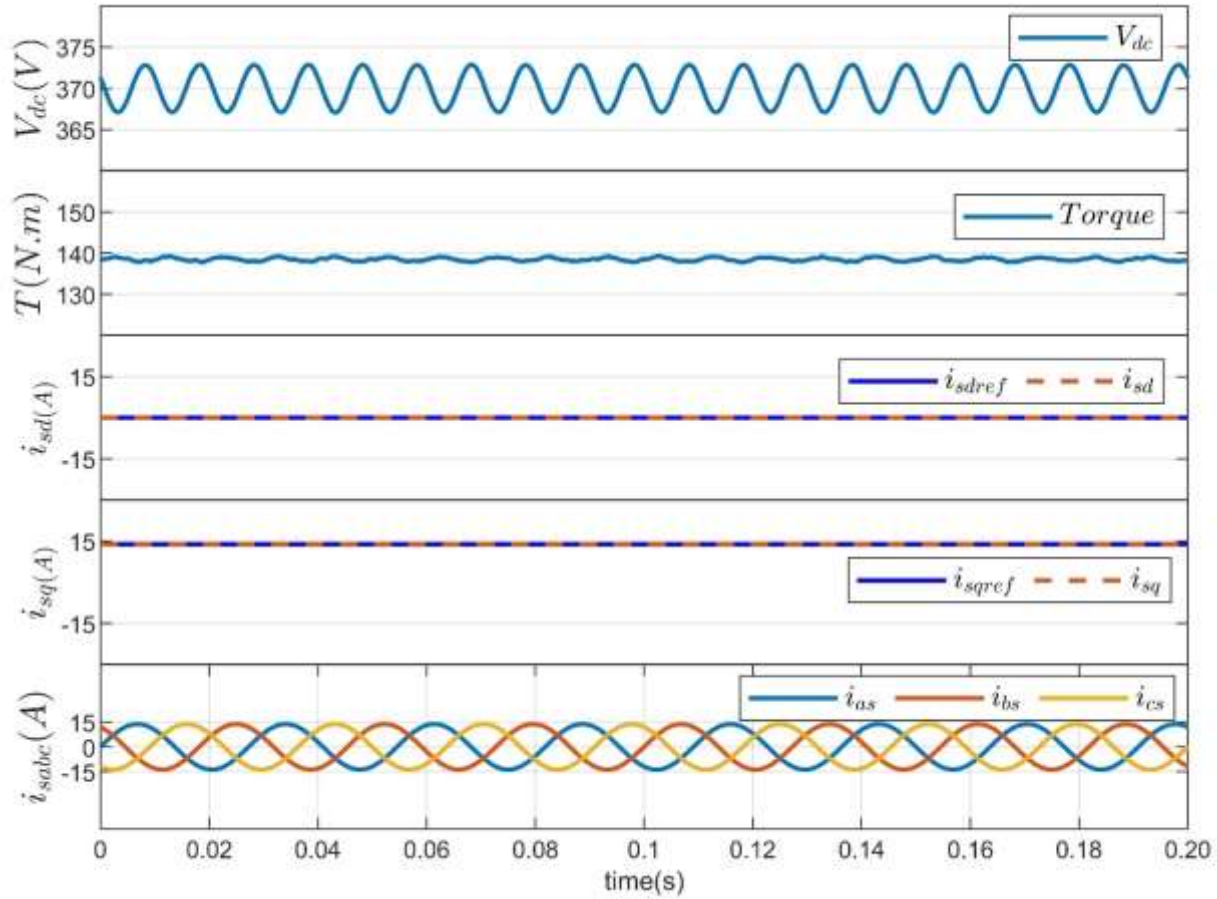


Figure 40: PMSG simulated outcomes of the grid when the resistance R and inductance L utilized in the controller are increased by 150% of their nominal values.

4.7 Summary

In this chapter, a composite controller has been designed to control both GSC and MSC for PMSG-based wind turbine considering both balanced and unbalanced grid voltages. When the grid voltage is balanced, the developed controller is formulated to control the dc-link voltage via GSC, while MSC is employed to control the power extracted from the wind through controlling the dq -axis components of the machine current. However, when the grid voltage is unbalanced, the role between MSC and GSC is interchanged so that MSC regulates the dc-link voltage, while GSC controls the amount of active and reactive powers delivered to the grid, which is achieved by controlling the dq -axis components of the grid current. The developed composite controller uses a feedback controller as a stabilizing compensator and a

disturbance observer as a servo-compensator. The disturbance observer was structured to enhance asymptotic regulation of the composite controller by estimating constant and sinusoidal disturbances that can arise under unbalanced grid voltages. The performances of the proposed controller have been tested in simulation considering both balanced and unbalanced grid voltages. The obtained results have shown a good control of the transient behavior of dc-link voltage in response to a sudden change of the grid conditions, which provides to the effectiveness of the disturbance observer to achieve seamless reconfiguration of the control scheme. Overall, the observed responses have shown good results under balanced grid voltage, but a double fundamental frequency oscillation was observed in the dc-link voltage and the machine torque when the grid voltage became unbalanced. To attenuate the effect of the dc-link voltage oscillation on the machine torque, the measurement of the dc-link voltage is passed through a notch filter before feeding it to the dc-link voltage controller. When implemented with a notch filter, the composite controller proved to be effective in achieving ripple-free torque.

Chapter 5: Conclusion

This thesis has addressed the control challenges associated with PMSG-based wind turbine under unbalanced grid voltages. The literature review conducted in chapter 1 highlighted that voltage unbalance can lead to double fundamental frequency oscillations in the instantaneous power injected to the grid which violates the grid code requirements. Additionally, voltage unbalance can cause undesirable dc-link voltage ripples, which can have an adverse impact on the torque response of the generator. These ripples can result in significant torque fluctuations, leading to vibrations that may diminish the durability and lifespan of the generator and the mechanical system used to couple the generator to the wind turbine. The problem of active power oscillations under unbalanced grid voltages is well established and addressed by several control techniques. It can be concluded from literature review that there is a general agreement that injecting free-ripple active power into grid requires the reactive power to oscillate around its dc component with a frequency 2ω . Besides, the sinusoidal currents flowing into the grid must be unbalanced to guarantee that the active power delivered to the grid is free from oscillations. The oscillatory behavior of the reactive power mandates employing controllers that are capable of achieving the tasks of asymptotic tracking of sinusoidal signals with non-zero dc components. Traditionally, integral action together with resonant controller can solve the problem of asymptotic tracking of such a signal reference provided that the oscillation frequency is known. The problem, however, is that the transient performances under such a control technique are mainly decided by the accuracy of the state model. More specifically, it is not possible to meet the desired transient response under model uncertainties, external unknown disturbances, and sudden changes in grid voltage conditions. This limitation of classical controllers has motivated the evaluation of an advanced control technique, known as Disturbance Observed-Based Control (DOBC). DOBC approach relies on combining a state-feedback control law with a disturbance observer. The feedback controller takes charge of stabilizing the closed-loop system, while the disturbance observer plays the role of servo-compensator. In other words, the disturbance observer assumes the role of suppressing the offset caused by model uncertainties and all

unknown disturbances that satisfy a specific dynamic equation. Designing such a composite controller requires using the state model that describes the dynamics of PMSG-based wind turbine, which is done in chapter 2.

Chapter 2 presents the typical topology of PMSG-based wind turbine which is composed of Grid-Side Converter (GSC), Machine-Side Converter (MSC), dc-link capacitor to interconnect GSC and MSC, PMSG coupled with a wind turbine, and an L filter to establish the connection between the grid and the GSC. This chapter also includes a comprehensive coverage of the derivation of all state models that are involved in the description of the dynamics of PMSG-based wind turbine. More precisely, this chapter presents a comprehensive description of the state models of PMSG and L filtered grid-tied inverter considering both rotating dq reference frame and stationery $\alpha\beta$ reference frame. This chapter also describes the dynamic equation of dc-link voltage under both balanced and unbalanced grid voltages.

Chapters 3 uses the state model of L filtered grid-tied inverter in the stationary $\alpha\beta$ frame to construct a controller for the regulation of the active and reactive powers delivered to the grid. The controller is designed based on DOBC approach with a view to regulate the power exchange between the grid and the dc-link capacitor, while at the same time meeting grid connection requirements under both balanced and unbalanced grid voltages. On the other hand, a current controller is developed for PMSG to adjust the power extracted from the wind turbine. The current controller is based on $\alpha\beta$ coordinates of PMSG and DOBC approach as a design procedure. The DOBC method is also adopted to synthesize a regulator for the dc-link voltage to cope with both balanced and unbalanced grid voltages. In fact, two controllers are developed for dc-link voltage; the first controller is implemented under balanced grid voltages, while the second one is used to cope with unbalanced grid voltages. Under balanced grid voltages, the GSC is utilized to regulate the dc-link voltage through the employment of a cascade control structure that consists of two loops; an outer loop and an inner loop. The outer loop is designed with the first dc-link voltage regulator, while the inner loop is implemented with the above-mentioned power control scheme to control the active and

reactive powers delivered to the grid. In such a case, the main function of the MSC is limited to implement the current controller for PMSG aiming to extract maximum available power from the wind. Under unbalanced grid voltages, the roles of GSC and MSC are interchanged; GSC takes charge of controlling only the active and reactive powers delivered to the grid, while MSC assures the role of regulating the dc-link voltage through the use of a cascade control structure. The latter consists of two loops; an outer loop for regulating dc-link voltage and an inner loop for controlling the stator currents of PMSG. The main function of the power controller, in this case, is that it allows implementing fault ride through requirement by adjusting the level of power delivery to the grid to match specific command values. Note that the control of PMSG, in this case, does not allow implementing maximum power point tracking algorithm as the command value for the current is provided by the outer voltage loop. In summary, chapter 3 presents two configurations of control scheme; one is used under balanced grid voltages, while the other one is employed under unbalanced voltages. The main concern for implementing such a control scheme to cope with both balanced and unbalanced grid voltages is due to the need for a smooth passage from one configuration to the other. This concern is easily resolved under DOBC approach by taking advantage of the disturbance observer to provide accurate information about the operating point just before each balanced/unbalance event. This helps in ensuring seamless transition between the two configurations in response to sudden changes in the grid voltage conditions. The last concern is due to the torque fluctuations that can appear as a result of dc-link voltage oscillations under unbalanced grid voltages. This concern is addressed in this paper by embedding a notch filter in the dc-link voltage regulator to suppress the 2ω oscillations from the current command of the current controller of PMSG. When it does so, the current controller can operate the PMSG to produce sinusoidal and balanced three-phase currents, thus developing ripple-free torque. In summary, the proposed reconfigurable control scheme presented in chapter 3 prevents the 2ω oscillations to propagate to PMSG and to the grid; these oscillations are confined between dc-link capacitor and L filter.

Chapter 4 is almost similar to chapter 3 in terms of control design, and the main difference is that the $\alpha\beta$ reference frame used in chapter 3 is replaced by dq reference frame.

In addition, the power controller of L filtered grid-tied inverter used in chapter 3 is replaced by a current controller in dq reference frame. As in chapter 3, all controllers in chapter 4 are designed based on DOBC approach to take advantage of the disturbance observer to ensure a smooth reconfiguration of the control scheme in response to sudden balance/unbalance event in the grid voltages.

Finally, the performances of the proposed reconfigurable control scheme have been evaluated using simulation tests for both balanced and unbalanced grid voltages. The simulation tests have been conducted using MATLAB Simulink software, and the corresponding results are presented in chapter 3 and 4. The obtained results show that the composite controller demonstrated excellent transient and steady-state performances in achieving the tasks of accurate tracking of sinusoidal references, ripple-free injected power, sinusoidal currents, ripple-free machine torque, and smooth reconfiguration of the control scheme in response to sudden changes in the grid conditions. Overall, the obtained results provide evidence of the effectiveness of the proposed control. Nevertheless, the required goals result in fluctuations in the dc-link voltage.

This thesis has presented the application of DOBC use of DOBC to deal with Among these, Composite DOBC structures offer several advantages. They can be easily designed and implemented, using secondary anti-windup features due to their separability and stable dynamic structure. At the same time, they effectively estimate and compensate the lumped disturbances including model uncertainties, parameter perturbations, unmodeled dynamics and external disturbances, thereby achieving robustness.

This thesis has presented the application of Disturbance Observer-Based Control (DOBC) approach for both GSC and MSC in PMSG based wind turbine. The aim is to mitigate the effect of 2ω ripple that arise during voltage unbalance. The proposed controller combines an output-feedback controller with a disturbance observer to provide an estimate of constant and sinusoidal disturbances of frequency 2ω , which approximate model uncertainties and unknown disturbances during voltage unbalance. This estimate is then used in the output-feedback controller to compensate for its effect on the control performance. The

DOBC technique is employed to operate the GSC ensuring accurate tracking of sinusoidal signals with zero and non-zero dc components, necessary for injecting ripple-free active power and sinusoidal currents into the grid. Similarly, DOBC technique is adopted to control MSC with a view to ensure asymptotic regulation of dc-link voltage. The control of MSC is achieved through the use of cascade control scheme, where an outer loop is used to regulate the dc-link voltage and an inner loop is employed to control the stator currents. Moreover, since there is no external path for the oscillation of frequency 2ω , it is not possible to completely remove the 2ω ripple caused by voltage unbalance. Thus, a notch filter is applied to confine the 2ω ripple between the dc-link capacitor and the L filter, preventing its propagation to the torque of the PMSG or through the grid.

References

- [1] A. Nouh and F. Mohamed, “Wind energy conversion systems: Classifications and trends in application,” in *2014 5th International Renewable Energy Congress (IREC)*, Mar. 2014, pp. 1–6. doi: 10.1109/IREC.2014.6826922.
- [2] J. Fadil, Soedibyo, and M. Ashari, “Performance comparison of vertical axis and horizontal axis wind turbines to get optimum power output,” in *2017 15th International Conference on Quality in Research (QiR) : International Symposium on Electrical and Computer Engineering*, Jul. 2017, pp. 429–433. doi: 10.1109/QIR.2017.8168524.
- [3] T. Fukami, M. Imamura, Y. Kaburaki, and T. Miyamoto, “A new self-regulated self-excited single-phase induction generator using a squirrel cage three-phase induction machine,” in *Proceedings 1995 International Conference on Energy Management and Power Delivery EMPD '95*, Nov. 1995, pp. 308–312 vol.1. doi: 10.1109/EMPD.1995.500744.
- [4] F. Martinez Rodrigo, J. M. Ruiz Gonzalez, J. A. Dominguez Vazquez, and L. C. Herrero de Lucas, “Sensorless control of a squirrel cage induction generator to track the peak power in a wind turbine,” in *IEEE 2002 28th Annual Conference of the Industrial Electronics Society. IECON 02*, Nov. 2002, pp. 169–174 vol.1. doi: 10.1109/IECON.2002.1187501.
- [5] R. Errouissi, A. Al-Durra, and M. Debouza, “A Novel Design of PI Current Controller for PMSG-Based Wind Turbine Considering Transient Performance Specifications and Control Saturation,” *IEEE Trans. Ind. Electron.*, vol. 65, no. 11, pp. 8624–8634, Nov. 2018, doi: 10.1109/TIE.2018.2814007.
- [6] S. Gao, H. Zhao, Y. Gui, D. Zhou, V. Terzija, and F. Blaabjerg, “A Novel Direct Power Control for DFIG With Parallel Compensator Under Unbalanced Grid Condition,” *IEEE Trans. Ind. Electron.*, vol. 68, no. 10, pp. 9607–9618, Oct. 2021, doi: 10.1109/TIE.2020.3022495.
- [7] R. D. Shukla, R. K. Tripathi, and S. Gupta, “Power electronics applications in wind energy conversion system: A review,” in *2010 International Conference on Power, Control and Embedded Systems*, Nov. 2010, pp. 1–6. doi: 10.1109/ICPCES.2010.5698663.
- [8] D. Porate, S. P. Gawande, K. B. Porate, R. N. Nagpure, M. A. Waghmare, and S. G. Kadwane, “Performance of PMSG Based Variable Speed WECS with Parallel Back-to-Back Converters Using Separate Zero d-axis Current Control,” in *2018 IEEE*

International Conference on Power Electronics, Drives and Energy Systems (PEDES), Chennai, India: IEEE, Dec. 2018, pp. 1–6. doi: 10.1109/PEDES.2018.8707805.

- [9] A. Tohidi, H. Hajieghrary, and M. A. Hsieh, “Adaptive Disturbance Rejection Control Scheme for DFIG-Based Wind Turbine: Theory and Experiments,” *IEEE Trans. Ind. Appl.*, vol. 52, no. 3, pp. 2006–2015, May 2016, doi: 10.1109/TIA.2016.2521354.
- [10] T. H. Nguyen and D.-C. Lee, “Advanced Fault Ride-Through Technique for PMSG Wind Turbine Systems Using Line-Side Converter as STATCOM,” *IEEE Trans. Ind. Electron.*, vol. 60, no. 7, pp. 2842–2850, Jul. 2013, doi: 10.1109/TIE.2012.2229673.
- [11] T. H. Nguyen and D.-C. Lee, “Ride-Through Technique for PMSG Wind Turbines using Energy Storage Systems,” *J. Power Electron.*, vol. 10, Nov. 2010, doi: 10.6113/JPE.2010.10.6.733.
- [12] A. Causebrook, D. J. Atkinson, and A. G. Jack, “Fault Ride-Through of Large Wind Farms Using Series Dynamic Braking Resistors (March 2007),” *IEEE Trans. Power Syst.*, vol. 22, no. 3, pp. 966–975, Aug. 2007, doi: 10.1109/TPWRS.2007.901658.
- [13] A. Uehara *et al.*, “A Coordinated Control Method to Smooth Wind Power Fluctuations of a PMSG-Based WECS,” *IEEE Trans. Energy Convers.*, vol. 26, no. 2, pp. 550–558, Jun. 2011, doi: 10.1109/TEC.2011.2107912.
- [14] L. Chang, W. Wu, and M. Mao, “LVRT control strategy of CSC-PMSG-WGS based on PIR controller,” in *2016 IEEE 7th International Symposium on Power Electronics for Distributed Generation Systems (PEDG)*, Jun. 2016, pp. 1–6. doi: 10.1109/PEDG.2016.7527027.
- [15] Y. Wang, J. Meng, X. Zhang, and L. Xu, “Control of PMSG-Based Wind Turbines for System Inertial Response and Power Oscillation Damping,” *IEEE Trans. Sustain. Energy*, vol. 6, no. 2, pp. 565–574, Apr. 2015, doi: 10.1109/TSTE.2015.2394363.
- [16] X. Guo, W. Liu, and Z. Lu, “Flexible Power Regulation and Current-Limited Control of the Grid-Connected Inverter Under Unbalanced Grid Voltage Faults,” *IEEE Trans. Ind. Electron.*, vol. 64, no. 9, pp. 7425–7432, Sep. 2017, doi: 10.1109/TIE.2017.2669018.
- [17] “An Output-Power-Control Strategy for a Three-Phase PWM Rectifier Under Unbalanced Supply Conditions | IEEE Journals & Magazine | IEEE Xplore.” Accessed: Jan. 23, 2024. [Online]. Available: <https://ieeexplore-ieee-org.uaeu.idm.oclc.org/document/4455581>

- [18] N. A. Orlando, R. A. Mastromauro, M. Liserre, and A. Dell'Aquila, "Grid voltage support by means of a small Wind Turbine System," in *2008 34th Annual Conference of IEEE Industrial Electronics*, Nov. 2008, pp. 2178–2183. doi: 10.1109/IECON.2008.4758294.
- [19] "Positive-Negative Sequence Current Controller for LVRT Improvement of Wind Farms Integrated MMC-HVDC Network | IEEE Journals & Magazine | IEEE Xplore." Accessed: Jan. 06, 2024. [Online]. Available: <https://ieeexplore-ieee-org.uaeu.idm.oclc.org/document/9233326>
- [20] "Coordinated DTC and VOC control for PMSG based grid connected wind energy conversion system | IEEE Conference Publication | IEEE Xplore." Accessed: Jan. 06, 2024. [Online]. Available: <https://ieeexplore-ieee-org.uaeu.idm.oclc.org/document/7977792>
- [21] R. Teodorescu, F. Blaabjerg, M. Liserre, and P. C. Loh, "Proportional-resonant controllers and filters for grid-connected voltage-source converters," *IEE Proc. - Electr. Power Appl.*, vol. 153, no. 5, p. 750, 2006, doi: 10.1049/ip-epa:20060008.
- [22] O. Aguilar-Mejia, R. Tapia-Olvera, and C. Santiago, *Adaptive Controller for PMSGs of Grid-Connected Wind Turbines*. 2012.
- [23] P. Dey, M. Datta, N. Fernando, and T. Senjyu, "A method to reduce DC-link overvoltage of PMSG based WECS during LVRT," in *2016 IEEE Region 10 Conference (TENCON)*, Nov. 2016, pp. 1894–1899. doi: 10.1109/TENCON.2016.7848351.
- [24] "(1) (PDF) Dynamic performance improvement of standalone battery integrated PMSG wind energy system using proportional resonant controller." Accessed: Jan. 08, 2024. [Online]. Available: https://www.researchgate.net/publication/319053319_Dynamic_performance_improvement_of_standalone_battery_integrated_PMSG_wind_energy_system_using_proportional_resonant_controller/figures?lo=1&utm_source=google&utm_medium=organic
- [25] G. Tsengenes, T. Nathenas, and G. Adamidis, "A three-level space vector modulated grid connected inverter with control scheme based on instantaneous power theory," *Simul. Model. Pract. Theory*, vol. 25, Jun. 2012, doi: 10.1016/j.simpat.2012.02.004.
- [26] T. Kato and K. Miyao, "Modified hysteresis control with minor loops for single-phase full-bridge inverters," in *Conference Record of the 1988 IEEE Industry*

Applications Society Annual Meeting, Oct. 1988, pp. 689–693 vol.1. doi: 10.1109/IAS.1988.25137.

- [27] G. Vázquez, P. Rodríguez, R. Ordoñez, T. Kerekes, and R. Teodorescu, “Adaptive hysteresis band current control for transformerless single-phase PV inverters,” in *2009 35th Annual Conference of IEEE Industrial Electronics*, Nov. 2009, pp. 173–177. doi: 10.1109/IECON.2009.5414770.
- [28] X. Zhang, L. Sun, K. Zhao, and L. Sun, “Nonlinear Speed Control for PMSM System Using Sliding-Mode Control and Disturbance Compensation Techniques,” *IEEE Trans. Power Electron.*, vol. 28, no. 3, pp. 1358–1365, Mar. 2013, doi: 10.1109/TPEL.2012.2206610.
- [29] N. A. Orlando, M. Liserre, R. A. Mastromauro, and A. Dell’Aquila, “A Survey of Control Issues in PMSG-Based Small Wind-Turbine Systems,” *IEEE Trans. Ind. Inform.*, vol. 9, no. 3, pp. 1211–1221, Aug. 2013, doi: 10.1109/TII.2013.2272888.
- [30] I. Matraji, A. Al-Durra, and R. Errouissi, “Design and experimental validation of enhanced adaptive second-order SMC for PMSG-based wind energy conversion system,” *Int. J. Electr. Power Energy Syst.*, vol. 103, pp. 21–30, Dec. 2018, doi: 10.1016/j.ijepes.2018.05.022.
- [31] S. Benelghali, M. E. H. Benbouzid, J. F. Charpentier, T. Ahmed-Ali, and I. Munteanu, “Experimental Validation of a Marine Current Turbine Simulator: Application to a Permanent Magnet Synchronous Generator-Based System Second-Order Sliding Mode Control,” *IEEE Trans. Ind. Electron.*, vol. 58, no. 1, pp. 118–126, Jan. 2011, doi: 10.1109/TIE.2010.2050293.
- [32] X. Shen *et al.*, “Adaptive Second-Order Sliding Mode Control for Grid-Connected NPC Converters With Enhanced Disturbance Rejection,” *IEEE Trans. Power Electron.*, vol. 37, no. 1, pp. 206–220, Jan. 2022, doi: 10.1109/TPEL.2021.3099844.
- [33] A. Swikir and V. Utkin, “Chattering analysis of conventional and super twisting sliding mode control algorithm,” in *2016 14th International Workshop on Variable Structure Systems (VSS)*, Jun. 2016, pp. 98–102. doi: 10.1109/VSS.2016.7506898.
- [34] Y. Shtessel, M. Taleb, and F. Plestan, “A novel adaptive-gain supertwisting sliding mode controller: Methodology and application,” *Automatica*, vol. 48, no. 5, pp. 759–769, May 2012, doi: 10.1016/j.automatica.2012.02.024.
- [35] Y. Feng, X. Yu, and Z. Man, “Non-singular terminal sliding mode control and its application for robot manipulators,” in *ISCAS 2001. The 2001 IEEE International*

Symposium on Circuits and Systems (Cat. No.01CH37196), May 2001, pp. 545–548 vol. 2. doi: 10.1109/ISCAS.2001.921368.

- [36] “An Adaptive Backstepping Nonsingular Fast Terminal Sliding Mode Control for Robust Fault Tolerant Control of Robot Manipulators | IEEE Journals & Magazine | IEEE Xplore.” Accessed: Jan. 08, 2024. [Online]. Available: <https://ieeexplore-ieee-org.uaeu.idm.oclc.org/document/8260945>
- [37] R. Errouissi and A. Al-Durra, “A Novel PI-Type Sliding Surface for PMSG-Based Wind Turbine With Improved Transient Performance,” *IEEE Trans. Energy Convers.*, vol. 33, no. 2, pp. 834–844, Jun. 2018, doi: 10.1109/TEC.2017.2776752.
- [38] E. M. Youness *et al.*, “Implementation and validation of backstepping control for PMSG wind turbine using dSPACE controller board,” *Energy Rep.*, vol. 5, pp. 807–821, Nov. 2019, doi: 10.1016/j.egy.2019.06.015.
- [39] Y. Kim, T. Park, and J. M. Lee, “Integration of model predictive control and backstepping approach and its stability analysis,” *IFAC-Pap.*, vol. 51, no. 18, pp. 405–410, Jan. 2018, doi: 10.1016/j.ifacol.2018.09.334.
- [40] T. K. Roy, M. A. Mahmud, S. N. Islam, and A. M. T. Oo, “Nonlinear Adaptive Backstepping Controller Design for Permanent Magnet Synchronous Generator (PMSG)-Based Wind Farms to Enhance Fault Ride Through Capabilities,” in *2019 IEEE Power & Energy Society General Meeting (PESGM)*, Aug. 2019, pp. 1–5. doi: 10.1109/PESGM40551.2019.8973758.
- [41] M. Makhad, M. Zazi, A. Loulijat, and A. O. Simon, “Robust Integral Backstepping control for Optimal Power Extraction of a PMSG-based Variable Speed Wind Turbines,” in *2020 1st International Conference on Innovative Research in Applied Science, Engineering and Technology (IRASET)*, Apr. 2020, pp. 1–6. doi: 10.1109/IRASET48871.2020.9092053.
- [42] “A new adaptive integral back stepping fractional order sliding mode control approach for PV and wind with battery system based DC microgrid - ScienceDirect.” Accessed: Jan. 09, 2024. [Online]. Available: <https://www.sciencedirect.com/science/article/abs/pii/S2213138822003137>
- [43] “Feedback Linearization Based Direct Torque Control for IPMSMs | IEEE Journals & Magazine | IEEE Xplore.” Accessed: Jan. 09, 2024. [Online]. Available: <https://ieeexplore-ieee-org.uaeu.idm.oclc.org/document/9149805>

- [44] A. Merabet, K. T. Ahmed, R. Beguenane, and H. Ibrahim, "Feedback linearization control with sliding mode disturbance compensator for PMSG based wind energy conversion system," in *2015 IEEE 28th Canadian Conference on Electrical and Computer Engineering (CCECE)*, May 2015, pp. 943–947. doi: 10.1109/CCECE.2015.7129402.
- [45] K.-H. Kim, Y.-C. Jeung, D.-C. Lee, and H.-G. Kim, "LVRT Scheme of PMSG Wind Power Systems Based on Feedback Linearization," *IEEE Trans. Power Electron.*, vol. 27, no. 5, pp. 2376–2384, May 2012, doi: 10.1109/TPEL.2011.2171999.
- [46] T. Ohnishi, "Three phase PWM converter/inverter by means of instantaneous active and reactive power control," in *Control and Instrumentation Proceedings IECON '91: 1991 International Conference on Industrial Electronics*, Oct. 1991, pp. 819–824 vol.1. doi: 10.1109/IECON.1991.239183.
- [47] "Improved switching table for direct power control of three-phase PWM rectifier | IEEE Conference Publication | IEEE Xplore." Accessed: Jan. 09, 2024. [Online]. Available: <https://ieeexplore-ieee-org.uaeu.idm.oclc.org/document/4548117>
- [48] M. Malinowski, M. Jasinski, and M. P. Kazmierkowski, "Simple direct power control of three-phase PWM rectifier using space-vector modulation (DPC-SVM)," *IEEE Trans. Ind. Electron.*, vol. 51, no. 2, pp. 447–454, Apr. 2004, doi: 10.1109/TIE.2004.825278.
- [49] V. Yaramasu and B. Wu, *Model Predictive Control of Wind Energy Conversion Systems*, 1st ed. Wiley, 2017. doi: 10.1002/9781119082989.
- [50] "Model Predictive Control and Direct Power Control for PWM Rectifiers With Active Power Ripple Minimization | IEEE Journals & Magazine | IEEE Xplore." Accessed: Jan. 09, 2024. [Online]. Available: <https://ieeexplore-ieee-org.uaeu.idm.oclc.org/document/7524701>
- [51] Y. Zhang and C. Qu, "Model Predictive Direct Power Control of PWM Rectifiers Under Unbalanced Network Conditions," *IEEE Trans. Ind. Electron.*, vol. 62, no. 7, pp. 4011–4022, Jul. 2015, doi: 10.1109/TIE.2014.2387796.
- [52] W. Jiang, W. Ma, J. Wang, L. Wang, and Y. Gao, "Deadbeat Control Based on Current Predictive Calibration for Grid-Connected Converter Under Unbalanced Grid Voltage," *IEEE Trans. Ind. Electron.*, vol. 64, no. 7, pp. 5479–5491, Jul. 2017, doi: 10.1109/TIE.2017.2674620.

- [53] J. Hu, L. Shang, Y. He, and Z. Q. Zhu, "Direct Active and Reactive Power Regulation of Grid-Connected DC/AC Converters Using Sliding Mode Control Approach," *IEEE Trans. Power Electron.*, vol. 26, no. 1, pp. 210–222, Jan. 2011, doi: 10.1109/TPEL.2010.2057518.
- [54] L. Shang, D. Sun, and J. Hu, "Sliding-mode-based direct power control of grid-connected voltage-sourced inverters under unbalanced network conditions," *IET Power Electron.*, vol. 4, no. 5, pp. 570–579, May 2011, doi: 10.1049/iet-pel.2010.0160.
- [55] D. Sun, X. Wang, and Y. Fang, "Backstepping direct power control without phase-locked loop of AC/DC converter under both balanced and unbalanced grid conditions," *IET Power Electron.*, vol. 9, no. 8, pp. 1614–1624, Jun. 2016, doi: 10.1049/iet-pel.2015.0653.
- [56] A. Bouafia, F. Krim, and J.-P. Gaubert, "Fuzzy-Logic-Based Switching State Selection for Direct Power Control of Three-Phase PWM Rectifier," *IEEE Trans. Ind. Electron.*, vol. 56, no. 6, pp. 1984–1992, Jun. 2009, doi: 10.1109/TIE.2009.2014746.
- [57] "Unified Power Control for PMSG-Based WECS Operating Under Different Grid Conditions | IEEE Journals & Magazine | IEEE Xplore." Accessed: Apr. 24, 2024. [Online]. Available: <https://ieeexplore-ieee-org.uaeu.idm.oclc.org/document/5742990>
- [58] H. T. Do, T. D. Dang, H. V. A. Truong, and K. K. Ahn, "Maximum Power Point Tracking and Output Power Control on Pressure Coupling Wind Energy Conversion System," *IEEE Trans. Ind. Electron.*, vol. 65, no. 2, pp. 1316–1324, Feb. 2018, doi: 10.1109/TIE.2017.2733424.
- [59] M. Heydari and K. Smedley, "Comparison of maximum power point tracking methods for medium to high power wind energy systems," in *2015 20th Conference on Electrical Power Distribution Networks Conference (EPDC)*, Apr. 2015, pp. 184–189. doi: 10.1109/EPDC.2015.7330493.
- [60] T. Nakamura, S. Morimoto, M. Sanada, and Y. Takeda, "Optimum control of IPMSG for wind generation system," in *Proceedings of the Power Conversion Conference-Osaka 2002 (Cat. No.02TH8579)*, Apr. 2002, pp. 1435–1440 vol.3. doi: 10.1109/PCC.2002.998184.
- [61] "Sensorless output maximization control for variable-speed wind generation system using IPMSG | IEEE Journals & Magazine | IEEE Xplore." Accessed: Jan. 10, 2024. [Online]. Available: <https://ieeexplore.ieee.org/document/1388662>

- [62] M. Pucci and M. Cirrincione, "Neural MPPT Control of Wind Generators With Induction Machines Without Speed Sensors," *Ind. Electron. IEEE Trans. On*, vol. 58, pp. 37–47, Feb. 2011, doi: 10.1109/TIE.2010.2043043.
- [63] I. K. Buehring and L. L. Freris, "Control policies for wind-energy conversion systems," *IEE Proc. C Gener. Transm. Distrib.*, vol. 128, no. 5, pp. 253–261, Sep. 1981, doi: 10.1049/ip-c.1981.0043.
- [64] "A novel algorithm for fast and efficient maximum power point tracking of wind energy conversion systems | IEEE Conference Publication | IEEE Xplore." Accessed: Jan. 10, 2024. [Online]. Available: <https://ieeexplore.ieee.org/document/4800030>
- [65] E. Abdou, A.-R. Youssef, S. Kamel, and M. Aly, "Sensor Less Proposed Multi Sector Perturb and Observe Maximum Power Tracking for 1.5 MW Based on DFIG," Jan. 2020, doi: 10.5281/zenodo.3607516.
- [66] "Improved Perturb and Observe MPPT Algorithm of Multi-Phase PMSG Based Wind Energy Conversion System | IEEE Conference Publication | IEEE Xplore." Accessed: Jan. 10, 2024. [Online]. Available: <https://ieeexplore.ieee.org/document/9008004>
- [67] "Maximum power extraction improvement using sensorless controller based on adaptive perturb and observe algorithm for PMSG wind turbine application - Putri - 2018 - IET Electric Power Applications - Wiley Online Library." Accessed: Jan. 10, 2024. [Online]. Available: <https://ietresearch.onlinelibrary.wiley.com/doi/full/10.1049/iet-epa.2017.0603>
- [68] H. H. H. Mousa, A.-R. Youssef, and E. E. M. Mohamed, "State of the art perturb and observe MPPT algorithms based wind energy conversion systems: A technology review," *Int. J. Electr. Power Energy Syst.*, vol. 126, p. 106598, Mar. 2021, doi: 10.1016/j.ijepes.2020.106598.
- [69] R. Tiwari and N. R. Babu, "Fuzzy Logic Based MPPT for Permanent Magnet Synchronous Generator in wind Energy Conversion System," *IFAC-Pap.*, vol. 49, no. 1, pp. 462–467, Jan. 2016, doi: 10.1016/j.ifacol.2016.03.097.
- [70] "An adaptive approximation method for maximum power point tracking (MPPT) in wind energy systems | IEEE Conference Publication | IEEE Xplore." Accessed: Jan. 14, 2024. [Online]. Available: <https://ieeexplore.ieee.org/document/6064125>

- [71] N. Saad, A. El-Sattar, and M. Metally, “Artificial neural controller for torque ripple control and maximum power extraction for wind system driven by switched reluctance generator,” *Ain Shams Eng. J.*, vol. 9, May 2017, doi: 10.1016/j.asej.2017.03.005.
- [72] W.-H. Chen, J. Yang, L. Guo, and S. Li, “Disturbance-Observer-Based Control and Related Methods—An Overview,” *IEEE Trans. Ind. Electron.*, vol. 63, no. 2, pp. 1083–1095, Feb. 2016, doi: 10.1109/TIE.2015.2478397.
- [73] “Torque - Speed Regulation of DC Motor Based on Load Torque Estimation Method. — Keio University.” Accessed: Jan. 15, 2024. [Online]. Available: <https://keio.elsevierpure.com/en/publications/torque-speed-regulation-of-dc-motor-based-on-load-torque-estimati>
- [74] “Generalized Multifrequency Current Controller for Grid-Connected Converters With LCL Filter | IEEE Journals & Magazine | IEEE Xplore.” Accessed: Mar. 11, 2024. [Online]. Available: <https://ieeexplore.ieee.org/document/8345159>
- [75] “Analysis of Electric Machinery and Drive Systems | IEEE eBooks | IEEE Xplore.” Accessed: Aug. 27, 2023. [Online]. Available: <https://ieeexplore.ieee.org/book/5265638>
- [76] “power_system_analysis_john_grainger_1st.pdf.” Accessed: Apr. 29, 2023. [Online]. Available: https://ritwikchowdhury.files.wordpress.com/2017/12/power_system_analysis_john_grainger_1st.pdf
- [77] X. Yao, C. Guo, Z. Xing, Y. Li, and S. Liu, “Variable Speed Wind Turbine Maximum Power Extraction Based on Fuzzy Logic Control,” in *2009 International Conference on Intelligent Human-Machine Systems and Cybernetics*, Aug. 2009, pp. 202–205. doi: 10.1109/IHMSC.2009.174.
- [78] “Grid Integration of Wind Energy: Onshore and Offshore Conversion Systems, 3rd Edition | Wiley,” Wiley.com. Accessed: Oct. 30, 2023. [Online]. Available: <https://www.wiley.com/en-kr/Grid+Integration+of+Wind+Energy%3A+Onshore+and+Offshore+Conversion+Systems%2C+3rd+Edition-p-9781119962946>
- [79] E. O. Sánchez, “SYNCHRONOUS GENERATORS The Electric Generators Handbook”, Accessed: Aug. 27, 2023. [Online]. Available: https://www.academia.edu/22537770/SYNCHRONOUS_GENERATORS_The_Electric_Generators_Handbook

- [80] M. Vidyasagar, *Nonlinear Systems Analysis*. in Classics in Applied Mathematics. Society for Industrial and Applied Mathematics, 2002. doi: 10.1137/1.9780898719185.
- [81] W.-H. Chen, “Disturbance observer based control for nonlinear systems,” *IEEEASME Trans. Mechatron.*, vol. 9, no. 4, pp. 706–710, Dec. 2004, doi: 10.1109/TMECH.2004.839034.
- [82] “(PDF) Nonlinear Systems Khalil (3rd Edition),” dokumen.tips. Accessed: Sep. 02, 2023. [Online]. Available: <https://dokumen.tips/documents/nonlinear-systems-khalil-3rd-edition.html>
- [83] Md. E. Haque, M. Negnevitsky, and K. M. Muttaqi, “A Novel Control Strategy for a Variable-Speed Wind Turbine With a Permanent-Magnet Synchronous Generator,” *IEEE Trans. Ind. Appl.*, vol. 46, no. 1, pp. 331–339, Jan. 2010, doi: 10.1109/TIA.2009.2036550.
- [84] P. Rodríguez, A. Luna, R. S. Muñoz-Aguilar, I. Etxeberria-Otadui, R. Teodorescu, and F. Blaabjerg, “A Stationary Reference Frame Grid Synchronization System for Three-Phase Grid-Connected Power Converters Under Adverse Grid Conditions,” *IEEE Trans. Power Electron.*, vol. 27, no. 1, pp. 99–112, Jan. 2012, doi: 10.1109/TPEL.2011.2159242.
- [85] R. Peña-Alzola, D. Campos-Gaona, P. F. Ksiazek, and M. Ordonez, “DC-Link Control Filtering Options for Torque Ripple Reduction in Low-Power Wind Turbines,” *IEEE Trans. Power Electron.*, vol. 32, no. 6, pp. 4812–4826, Jun. 2017, doi: 10.1109/TPEL.2016.2597844.
- [86] V. Kaura and V. Blasko, “Operation of a phase locked loop system under distorted utility conditions,” *IEEE Trans. Ind. Appl.*, vol. 33, no. 1, pp. 58–63, Jan. 1997, doi: 10.1109/28.567077.
- [87] P. Rodriguez, J. Pou, J. Bergas, J. I. Candela, R. P. Burgos, and D. Boroyevich, “Decoupled Double Synchronous Reference Frame PLL for Power Converters Control,” *IEEE Trans. Power Electron.*, vol. 22, no. 2, pp. 584–592, Mar. 2007, doi: 10.1109/TPEL.2006.890000.
- [88] “New Optimized PWM VSC Control Structures and Strategies Under Unbalanced Voltage Transients | IEEE Journals & Magazine | IEEE Xplore.” Accessed: Dec. 15, 2023. [Online]. Available: <https://ieeexplore-ieee-org.uaeu.idm.oclc.org/document/4300923>

List of Publications

M. Alanani and R. Errouissi, “Mitigation of 2w-Ripple in PMSG-based Wind Turbine Under Unbalanced Grid Voltages Using DOBC along with Notch Filter,” in *IEEE EUROCON 2023 - 20th International Conference on Smart Technologies*, Jul. 2023, pp. 484–489. doi: 10.1109/EUROCON56442.2023.10199051.

The logo of the United Arab Emirates University (UAEU) is displayed in white text on a red rectangular background.

جامعة الإمارات العربية المتحدة
United Arab Emirates University



UAEU MASTER THESIS NO. 2024: 25

The research context perspectives develop a disturbance observer-based control for PMSG-wind turbine under unbalanced grid conditions, the objective of the controller is to inject ripple-free active power to the grid during grid faults. Therefore, a lot of research related to this challenge were developed and implemented to design a robust controller to achieve the objective.

Moayad Maher Alanani received his Master of Science in Electrical Engineering from the Department of Electrical and Communication Engineering, College of Engineering at the United Arab Emirates University, UAE. He received his BSc in Electrical Engineering from the College of Electrical and Communication Engineering, The Hashemite University, Jordan.

www.uaeu.ac.ae

Online publication of thesis:
<https://scholarworks.uaeu.ac.ae/etds/>

UAEU عمادة المكتبات
Libraries Deanship

جامعة الإمارات العربية المتحدة
United Arab Emirates University

Digital Library Services Section - قسم الخدمات المكتبية الرقمية